

Alma Mater Studiorum - Università di Bologna

**NANOSCALE-ELECTRICAL AND
OPTICAL PROPERTIES
OF III- NITRIDES**

by

Albert Minj

Dissertation for the degree of
DOCTOR OF PHILOSOPHY IN PHYSICS

in the

FACOLTÀ DI SCIENZE MATEMATICHE FISICHE E NATURALI

Relatore: Prof. Anna Cavallini

Coordinatore di Dottorato: Prof. Fabio Ortolani

Dottorato di Ricerca in Fisica Ciclo XXV, Settore Concorsuale: 02/B1, SSD: FIS/03

Abstract

III-nitrides are wide-band gap materials that have applications in both electronics and optoelectronic devices. Because to their inherent strong polarization properties, thermal stability and higher breakdown voltage in Al(Ga,In)N/GaN heterostructures, they have emerged as strong candidates for high power high frequency transistors. Nonetheless, the use of (Al,In)GaN/GaN in solid state lighting has already proved its success by the commercialization of light-emitting diodes and lasers in blue to UV-range. However, devices based on these heterostructures suffer problems associated to structural defects. This thesis primarily focuses on the nanoscale electrical characterization and the identification of these defects, their physical origin and their effect on the electrical and optical properties of the material. Since, these defects are nano-sized, the thesis deals with the understanding of the results obtained by nano and micro-characterization techniques such as atomic force microscopy (AFM), current-AFM, scanning kelvin probe microscopy (SKPM), electron beam induced current (EBIC) and scanning tunneling microscopy (STM). This allowed us to probe individual defects (dislocations and cracks) and unveil their electrical properties. Taking further advantage of these techniques, conduction mechanism in two-dimensional electron gas heterostructures was well understood and modeled. Secondly, origin of photoluminescence was deeply investigated. Radiative transition related to confined electrons and photoexcited holes in 2DEG heterostructures was identified and many body effects in nitrides under strong optical excitations were comprehended.

Keywords: III-Nitrides, GaN, HEMT, 2DEG, dislocations, V-defects, conduction mechanism, CAFM, SKPM

Acknowledgements

It would not have been possible to write this doctoral thesis without the help and support of the people around me, to only some of whom it is possible to give particular mention here. This thesis would not have been possible without the help, support and patience of my principal supervisor, **Prof. Anna Cavallini**, not to mention her advice and unsurpassed knowledge in electrical characterization and defects in semiconductors, publication of articles in peer-reviewed journals and career-counseling. Her remarks and consistent encouragements through out the last 3 years were invaluable on both an academic and a personal level, for which I am extremely grateful. Also, I would also like to thank her for her support and assistance and administrating me to follow the timeline since the start of my doctoral program in 2009.

My sincere gratitude and many thanks go in particular to **Dr. Daniela Cavalcoli**. I am very much indebted to her for her time, availability in time of need, science discussions, supervision in operating SEM, AFM. And furthermore, I highly appreciate her for spending her precious time to listen my doubts and difficulties, to give beneficial proposal in carrying out novel and particular measurements, in understanding new concepts, to discuss most of my new results, and to manage every technical need required for my experiments.

I would also like to thank **Prof. Beatrice Fraboni** for her support, cooperation and encouragement in carrying out additional electrical measurements, which gave me a boost to carry out unconventional electrical characterization with AFM. Moreover, I would like to acknowledge that her suggestions were very useful in the systematic understanding of complex results.

I would like to thank **Antonio Castaldini** for his technical assistance with his vast experience and knowledge in making very complicated contacts.

I would like to acknowledge the **EU Project RAINBOW** that provided the full financial support including studentship, accessories required for the research, visit to another laboratories, participation in schools, or conference and traveling back to home.

It is a pleasure to pay tribute also to the sample collaborators. To **Ocal Tuna** and **Dr. C. Giesen** from AIXTRON and **Pierro Gammara** and **Dr. M-A. Poisson** from Alcatel, I would like to thank for providing numerous high quality AlInN/GaN, AlGaN/GaN, InGaN/GaN and InN samples, not to mention that they struggled very hard to prepare these samples.

I also extend my sincere gratitude to **Prof. Michael Kneissl** and **Dr. Patrick Vogt**, who gave me the opportunity to work in their laboratory at Technische Universität Berlin, Germany. Whole-heartedly, I would like to thank **Daria Skuridina** for accompanying me with intense and long experiments based on STM, XPS and AES, stretching very often more than continuous 12 hours. Other than this, she is highly appreciated to continue performing measurements and providing results even in my absence. I sincerely thank also **Dr. Duc Van Dinh**, who carried out XRD measurements on thin samples in his busy schedule and helped me grow my first MOCVD sample.

My sincere gratitude goes to **Prof. Rudiger Goldhahn** and **Dr. Martin Feneberg**, who gave me the chance to work on PL measurements in their laboratory in Magdeburg, Germany and their time to explain the fundamentals of photoluminescence. Many thanks go to **Dr. Fatima Romero** for pleasure working extensively together for 10-12 hours/day per week on photoluminescence and the discussion of the results.

I would like to sincerely thank **Dr. Arantxa-Vilalta Clemente**, from whose publication and sharing of her results helped me in understanding structural defects in nitrides and in particular, the same samples I was dealing with. Her continuous effort in providing more data on the samples, especially TEM and RBS, helped me in getting more insight in formation of structural defects and compositional inhomogeneities.

I am very thankful to **Andrea Civatti** from my laboratory, for his continuous enthusiasm, kind and helping nature in doing and teaching me metal evaporation on my samples. I highly appreciate his generosity for providing me with a lab-view program of my need to operate current-source.

My sincere gratitude to **Prof. F. Calle** and **Tommaso Brazzini** for showing high interest in this research and providing metallic contacts and their electrical characterization.

I would like to give my sincere gratitude to **Dr. Naresh Kumar** and **Dr. Carol-Tragor Cowan**, who gave me an opportunity to visit their laboratory. I am thankful for their successful collaboration, and for showing similar interest in exploring the nature of dislocations.

Amid, all of them, it is highly worth to mention **Saurabh Pandey** with whom I worked very closely, travelled mostly to the same conferences all over the world and co-authored many articles, created an exciting work environment, where frequent diverse discussions

on science and philosophy occurred and where it was easy to understand to physics. Moreover, his support was something I could count on.

I gratefully thank **Dr. Harisingh Shankar** for giving his time in proof-reading of this thesis. I have also benefited by advice and guidance from newly joined **Dr. Alberto Basile** who always kindly grants me his time even for answering some of my unintelligent questions about fundamental of physics and for carrying out arguments on “future of nitrides”, and of course, an entertaining trip to a new city.

Amongst my fellow colleagues in the Department, the effort made by **Saurabh, Alessandra Scidà, Lucia Amidani, Andrea Ciavatti, Stefania Carapezzi, Martina Perani** and newly joined **Alberto, Shankar** and **Geeta M. Rani** in promoting an international, welcoming, academic and social environment. Scidà and Lucia, in particular, helped me in getting adapted to a complete new culture and whole-heartedly welcomed me. Their kindness and their warm nature are unforgettable.

I would also like to mention my friends in Bologna, particularly, **Max, Irina, Chiara, Arianna** and **Jacopo**, who taught me ABCD of “Italian” and gave a pleasant and cheerful environment. It is hard to imagine myself in Bologna without them.

I would like to thank my **Mother, brothers** and **Aunts** for supporting me spiritually and showing care in this entire period I was away from them.

Above all, I would like to specially thank my friends, **Irina** and **Anna**, for their care and confidence on me. They always had great patience with me at all times and served me every time I was in need. It is there belief that I could make this, and to them is my thesis specially dedicated.

Contents

Abstract	i
Acknowledgements	ii
Table of Contents	v
Introduction	1
0.1 Overview and Scientific Research on III-Nitrides	1
0.2 Nitrides in Optoelectronics	2
0.3 Nitrides in power electronics	2
0.4 Objectives of this thesis	3
0.5 Structure of this thesis	3
1 Fundamental properties of III-Nitrides	8
1.1 Crystal structure	8
1.1.1 Lattice constants of binary compounds	9
1.1.2 Lattice constants of ternary compounds	9
1.2 Disorder in nature	11
1.2.1 AlGaN system	11
1.2.2 InGaN system	11
1.3 Band structure	12
1.3.1 Conventional signs	13
1.3.2 Introduction on theoretical calculation of band structure	13
1.3.3 k.p theory	14
1.3.4 An overview of the full Band structure	14
1.4 Polarization	18
1.4.1 Spontaneous polarization	19
1.4.2 Peizelectric polarization	20
1.4.3 Polarization in ternary alloys	22
1.4.4 Polarization at interfaces of heterostructures	25
2 Defects in III-Nitrides	33
2.1 Introduction	33
2.2 Threading dislocations	33
2.2.1 The debate on dislocations	35
2.2.2 Determination of dislocations	37

2.2.3	Dislocations and current transport	37
2.3	V-shape defects	41
2.4	Misfit Dislocations	44
2.5	Basal plan stacking faults (BPSF)	46
2.6	Cracks	49
3	Experimental techniques	55
3.1	Atomic force microscopy	55
3.1.1	AFM Setup	56
3.1.1.1	How does AFM work?	57
3.1.2	Contact mode	58
3.1.2.1	Dynamics of the tip in contact mode	58
3.1.3	Semi contact mode	60
3.1.3.1	Dynamics of the tip in semi-contact mode	60
3.1.3.2	Phase imaging (elastic and inelastic interactions)	65
3.1.3.3	Phase vs tip-sample separation	66
3.2	Scanning tunneling Microscopy (STM)	68
3.3	Electron beam induced current	69
3.3.1	Electron-hole pair generation	70
3.3.2	Carrier dynamics	70
3.3.3	EBIC Contrast	72
3.4	Photoluminescence (PL)	74
3.5	X-ray photoelectron spectroscopy (XPS)	75
3.5.1	Angular resolved XPS	76
4	GaN	80
4.1	Surface and electrical properties	80
4.2	Experimental section	80
4.2.1	Sensitivity of KPFM	81
4.3	Results and discussions	82
4.4	Optical characterization of GaN: Photoluminescence	87
4.4.1	Temperature dependent PL	87
4.4.2	Thermal quenching of free excitons	90
4.4.3	Thermal quenching of donor bound excitons	91
4.4.4	Conclusions	91
5	AlGaInN/(AlN)/GaN	94
5.1	Structural properties	94
5.2	Surface analysis	94
5.2.1	Topography	94
5.2.2	Surface structure	97
5.2.3	LEED	98
5.2.4	XPS, AES: Ga incorporation	98
5.2.5	Estimation of Ga	99
5.2.5.1	Determination of composition at the surface (Angle re- solved XPS)	100
5.2.5.2	Gallium incorporation	100

5.3	Electrical characterization	102
5.3.1	Fermi-level determination by XPS	102
5.3.2	Local current transport	103
5.3.2.1	Nano-electrical characterization of defect free surface	103
5.3.2.2	Model of the electrical transport	104
5.3.2.3	Comparison of n_{2D} with Hall measurement data	110
5.4	Electrical characterization of extended defects	112
5.4.1	Threading dislocations	112
5.4.2	Formation of nanocracks	116
5.5	Optical characterization: PL	121
6	InGaN	128
6.1	Structural properties	128
6.2	Electrical characterization of the surface	131
6.2.1	Effect of indium incorporation	131
6.3	Optical characterization with PL	137
6.3.1	Observation of high-excitation bands	141
7	Conclusions	146
7.1	GaN	146
7.2	AlInGaN/(AlN)/GaN	147
7.3	InGaN/GaN	148
	List of publications	150

Dedicated to my friends. . .

Introduction

0.1 Overview and Scientific Research on III-Nitrides

It is almost four decades since the first GaN was produced and we have now a very well established nitride semiconductor based industry to produce light sources such as light emitting diodes (LEDs), laser diodes (LDs) and electronic devices. In these 40 years, a significant progress has been done to develop nitride alloys and to realize operating devices out of them. Meanwhile, the commercial electronic industries have greatly expanded since the revolution of personal computers and miniaturization of silicon chips, and they have thrived very well on the amelioration in technology. For instance, back in 1980s and 1990s, reading/writing data in optical disks was done through infra-red (IR) laser diodes such as AlGaAs/GaAs IR Lasers (780 nm) and AlGaInP (650nm) (CDs and DVDs). Differently, today the demands to record high-density data have expanded to such an extent that the use of shorter wavelength LDs is inevitable. Already present in the market, InGaN epitaxial layers are used for violet laser diode (405 nm wavelength) to store a two-hour long Hi-Vision movie. Its not only the optical disks, but a number of applications, including full-color electroluminescent displays, laser printers, high density information storage on magnetic, optical communications highly desires short-wavelength-emitting devices. Apart from optoelectronic devices, owing to their wide band gap and tolerance to high temperature and radiation, they are used as high power and high frequency (> 1 GHz) amplifiers with applications ranging from satellite links to wireless communications, from highways to electronic warfare. In developing the research on nitrides to establishing it into a huge industry, a significant number of scientists have given their effort. It is, therefore, worth enlightening the history of the development of nitride-based semiconductors.

0.2 Nitrides in Optoelectronics

Compared to other III-V compounds, group III nitrides are highly resistant to degradation from intense illumination and high currents due to their strong chemical bonds. Further facilitation with its tunability of Al-In-Ga-N composition allows one to achieve band gap in the entire visible spectrum, eventually one could realize all three primary blue, green and red light sources. Due to lack of technology to prepare nitrides, this was not possible until 1969 when the first GaN was grown by Maruska and Tietjen [1], and after two years MIS-LEDs [2] and the stimulation of the UV emission [3] from single crystal needles of GaN were demonstrated. In the same year, growth of GaN by MOCVD opened up new prospects for a new industry of optoelectronic devices for mass production [4]. For two decades, there was a steady development of growth reactors/techniques, improvement of GaN quality and actualization of AlN for higher emission energies. In 1989, p-type doping of GaN with Mg by Amano et al. produced a conventional p-n junction based GaN LED [5]. Since then, a tremendous research activity in producing higher quality of GaN, AlN and their alloys was seen. And between 1992 and 1996, a number of landmarks were set with the achievement of InGaN SQW/MQWs structures [6],[7] and InGaN/AlGaIn QWs [8], which subsequently led to the realization of blue, green and yellow LEDs [9],[8],[7],[10] and UV/blue laser diodes [11],[12],[13],[14]. This eventually laid the foundations of the nitride-based optoelectronics.

0.3 Nitrides in power electronics

The observation of enhanced mobility effect in AlGaAs/GaAs heterojunctions in 1978 by Dingle et al. [15], paved a way to a new kind of field-effect transistors and in a year, high electron mobility transistors (HEMT) were demonstrated by Mimura et al. [16] and Delagebeaudeuf et al. [17] within the same year. The two dimensional (2D) nature of the carrier gas formed at the interface induced by the diffusion and alienation of free carriers from donors in high band gap region (AlGaAs) to an undoped-low band gap region (GaAs) was attributed to the enhancement of mobility. From then onwards, high power devices were materialized with other group III-arsenides including AlGaAs/InGaAs and AlInAs/InGaAs heterostructures. During the development era of epitaxy of nitrides, in 1991, Khan et al. observed similar enhanced mobility effect in AlGaIn/GaN heterostructures [18] and attributed it to the presence of two-dimensional electron gas (2DEG) at the interface, though its origin wasn't comprehended very well. Unlike in arsenides, mobility here was related to the presence of inherent strong polarization field in nitrides. In 1993, this work further led to the demonstration of first AlGaIn/GaN based

HEMTs [19]. As the nitride community was still struggling with a good quality growth and development of ohmic contacts, in 1994, 0.25 μm AlGaIn/GaN based HEMTs [20] demonstrated characteristics suitable for microwave applications. When compared to group-III arsenides, nitride-based HEMTs hold several advantages, which are mainly due to their high breakdown voltage and high saturation velocity, which makes them ideal for high power applications and high-speed device operation, respectively. In recent years, there were several other important advancements in the design of HEMTs to improve its mobility and free carrier concentration (2DEG) such as insertion of AlN interlayer [21],[22], and introduction of new ternary (lattice matched AlInN) [23] and quaternary alloys to avoid cracking problem.

0.4 Objectives of this thesis

This thesis deals with different aspects of group-III nitrides: (1) characteristics of extended defects, specially threading dislocations, V-shape defects in terms of potential, conductivity, recombination properties in GaN and ternary/quaternary alloys such as AlInN, AlGaIn, InGaIn and AlGaInN. These investigations have been performed by means of Kelvin probe force microscopy, conductivity atomic force microscopy and electron beam induced current. (2) radiative recombination properties of 2DEG and nano-scale conduction mechanism in AlGaInN/GaN and AlGaIn/GaN. (3) effect of indium fluctuation and structural deformation on radiative recombination properties and the study of many body effects that are associated with the optical gain.

0.5 Structure of this thesis

Chapter I is an overview of the fundamental (structural, optical and electrical) properties of group III binary (GaN, AlN, InN) and ternary (AlInN, InGaIn) nitrides and their heterostructures that are often used in devices. It also discusses advantages and disadvantages of strong inherent polarization fields in power and optoelectronics. Since study of structural defects is one of the most important objectives of this thesis, the entire Chapter II is dedicated to the ongoing debate about their nature. Some of the key results presented in this thesis are based on techniques that are not commonly used such as current-atomic force microscopy (C-AFM), scanning kelvin probe microscopy (SKPM), electron beam induced current (EBIC) or their interpretation is not fully understood such as phase-contrast imaging of AFM. Chapter III explains the principle behind their operation and discusses why the interpretation of the results is not straight forward. Photoluminescence (PL) is also described in this chapter with the description

of the results achieved by HeCd and ArF lasers.

The following chapters focus mainly on the key results. In Chapter IV, surface properties of 3 μm thick-GaN template MOCVD grown on sapphire with a low temperature (LT) GaN nucleation layer is discussed in detail. The identification of the dislocations and V-shape defects is discussed and the origin of potential and conductivity around them is well explained. It is also explained why the spots related to increment in induced current (appearing as bright spots) is often observed in EBIC measurements of GaN. Results on photoluminescence performed on the same are presented to understand optical transitions of donor bound excitons and free excitons from the conduction band to valence bands. These results are also intended to aid the understanding of PL measurements performed on heterostructures grown on GaN.

In the next Chapter V, electrical properties of V-defects in InGaN are studied by C-AFM and KPFM measurements. V-defects mentioned in this chapter are associated to threading dislocations. A significant difference is observed when they are compared to V-defects in GaN. Surface potential in InGaN samples showed strong dependence on the indium concentration of InGaN, which hints towards the charge state of the V-defects. As the V-defects are associated with the acceptor states, the electron concentration in the InGaN system would determine the degree to which these acceptor states are filled. The C-AFM also showed that conductivity of V-defects is strongly dependent on the indium content in InGaN. This is reasonably explained by indium segregation and the hypothesis of reduced local band gap due to high-indium incorporation near the V-defects. Optical characterization with photoluminescence InGaN samples demonstrated a strong correlation between the alloy disordering and indium incorporation, dominance of localized excitons and S-shaped temperature dependence of the exciton emission indicating local band gap fluctuations in the sample. Photoluminescence showed a very good correlation with AFM, XRD and SPV results. Very interestingly, band gap renormalization and appearance of stimulated emission on excitation with higher density was observed, which is related to the electron hole plasma recombination. This phenomena was observed for indium from 13% to 17%. Presence of many body effects suggests a high quality InGaN layer and this would be very useful to boost LEDs/LDs performance as it causes an increase in the optical gain.

Chapter VI is focused on HEMT structures with and without AlN interlayer: Al(In,Ga)N/GaN and Al(In,Ga)N/AlN/GaN. For different AlN thickness, surface morphology has been studied in terms of roughness, height-height correlation length, dislocation density and other defects as they all determine the mobility of 2DEG. Since gallium incorporation during the growth of AlInN is one of the main issues for the growers, a detailed

XPS characterization is performed to evaluate the amount of Ga that was incorporated into AlInN layer. These results are compared with RBS measurements. C-AFM was performed to study the inhomogeneity and conduction paths present on the surface. With the aid of nanoscale I-V measurements, our results show that dislocations in AlIn-GaN are highly conductive in nature. This is also deduced by phase-contrast imaging to be related to segregation of metallic atoms such as In or Ga near the V-defects and dislocation core, which forms a current or leakage path between the surface and 2DEG region. Since any disordering of this sort can cause a local variation in band gap or may induce new states in the forbidden gap, scanning tunneling microscopy (STM) and scanning tunneling spectroscopy (STS) measurements were performed. STS measurement on V-defects shows a reduction in the band gap along with some metallic behavior in local points. Interestingly, autocorrelation length calculated from the topography obtained using STM aided very well in fitting our experimental mobility data on these samples with the roughness-limited hall mobility. The chapter further shows the modeling of image-induced barrier lowering at the 2DEG region and is in agreement with the nano-scale I-V characteristics done on defect-free area. In the section of optical characterization, photoluminescence measurements show that the luminescence is dominated by the narrow emission line widths of D_0X , FX_A and FX_B in GaN and the transitions related to photoexcited carriers in the 2DEG region is deeply explained.

Bibliography

- [1] Maruska and Tietjen. *Appl. Phys. Lett.*, 15:327, 1969.
- [2] J. I. Pankove, E. A. Miller, , and J. E. Berkeyheiser. *RCA Rev.*, 32:383–392, 1971.
- [3] R. Dingle, K. L. Shaklee, R. F. Leheny, and R. B. Zetterstrom. *Appl. Phys. Lett.*, 19:5, 1971.
- [4] H. M. Manasevit, F. M. Erdmann, and W. I. Simpson. *J. Electrochem. Soc.*, 118:1864–1868, 1971.
- [5] H. Amano, M. Kito, K. Hiramatsu, and I. Akasaki. *Jpn. J. Appl. Phys.*, 28:L2112–L2114, 1989.
- [6] S. Nakamura, T. Mukai, M. Senoh, Shin ichi Nagahama, and N. Iwasa. *Jpn. J. Appl. Phys.*, 74:3911, 1993.
- [7] S. Nakamura, M. Senoh, N. Iwasa, Shin ichi Nagahama, T. Yamada, and T. Mukai. *Jpn. J. Appl. Phys.*, 34:1332, 1995.
- [8] S. Nakamura, T. Mukai, and M. Senoh. *Appl. Phys. Lett.*, 64:1687, 1994.
- [9] S. Nakamura, T. Mukai, and M. Senoh. *J. Appl. Phys.*, 76:18189, 1994.
- [10] S. Nakamura, M. Senoh, N. Iwasa, Shin ichi Nagahama, T. Yamada, and T. Mukai. *Jpn. J. Appl. Phys.*, 34:L797, 1995.
- [11] S. Nakamura, M. Senoh, Shin ichi Nagahama, N. Iwasa, T. Yamada, T. Matsushita, H. Kiyoku, and Y. Sugimoto. *Jpn. J. Appl. Phys.*, 35:L74, 1996.
- [12] S. Nakamura. *MRS Proceedings*, 449:1135, 1996.
- [13] K. Itaya, M. Onomura, J. Nishio, L. Sugiura, S. Saito, M. Suzuki, J. Rennie, Shin ya Nunoue, M. Yamamoto, H. Fujimoto, Y. Kokubun, Y. Ohba, Gen ichi Hatakoshi, and M. Ishikawa. *Jpn. J. Appl. Phys.*, 35:L1315, 1996.
- [14] I. Akasaki, S. Sota, H. Sakai, T. Tanaka, M. Koike, and H. Amano. *Electron. Lett.*, 32:1105, 1996.

-
- [15] R. Dingle, H. L. Stormer, A. C. Gossard, and W. Wiegmann. *Appl. Phys. Lett.*, 33:665, 1978.
- [16] T. Mimura, S. Hiyamizu, T. Fujii, and K. Nanbu. *Jpn. J. Appl. Phys.*, 19:L225–L227, 1980.
- [17] D. Delagebeaudeuf, P. Delescluse, P. Etienne, M. Laviron, J. Chaplart, and Nuyen T. Linh. *Electron. Lett.*, 16:667, 1980.
- [18] M. A Khan, J. M. Van Hove, J. N. Kuznia, and D. T. Olson. *Appl. Phys. Lett.*, 58:2408, 1991.
- [19] M. A Khan, A. Bhattarai, J. N. Kuznia, and D. T. Olson. *Appl. Phys. Lett.*, 63:1214, 1993.
- [20] M. A Khan, J. N. Kuznia, D. T. Olson, W. J. Schaff, J. W. Burm, and M. S. Shur. *Appl. Phys. Lett.*, 65:1121, 1994.
- [21] I. P. Smorchkova, S. Keller, S. Heikman, C. R. Elsass, B. Heying, P. Fini, J. S. Speck, and U. K. Mishra. *Appl. Phys. Lett.*, 77:3998, 2000.
- [22] I. P. Smorchkova, L. Chen, T. Mates, L. Shen, S. Heikman, B. Moran, S. Keller, S. P. DenBaars, J. S. Speck, and U. K. Mishra. *J. Appl. Phys.*, 90:5196, 2001.
- [23] J. Kuzmik. *IEEE Elec. Dev. Letts.*, 510:22, 2001.

Chapter 1

Fundamental properties of III-Nitrides

1.1 Crystal structure

GaN, AlN and InN are the commonly known binary compounds of nitride family. Using carefully optimized growth conditions, their ternary and quaternary alloys could be obtained, which are of great significance in the field of electronics and optoelectronics. Two widely used growth techniques for nitride family are metal organic chemical vapor deposition (MOCVD) and molecular beam epitaxy (MBE). Usually, nitrides have a wurtzite (α -phase) structure as it is thermodynamically very stable and conventionally grown on $Al_2O_3(0001)$, SiC(0001), Si(111) and GaAs (111). However, by selecting an appropriate cubic substrate, one may also grow them in their metastable state, zincblende structure (β -phase). For instance, when GaN is grown on cubic substrates of Si(001) or GaAs(001), MgO, zinc blende structure is more favored. [1],[2],[3],[4]. But, there are also some reports that show cubic inclusions or cubic growth on the same substrates intended for wurtzite structures, were induced by doping or altering growth temperature and other certain growth conditions or in some cases could be induced due to substrate misorientation [5],[6],[7],[8],[9],[10],[11],[12]. Geometrically, because of its atomic arrangement, cubic (111) facets are equivalent to hexagonal (0001) facets. Therefore, cubic (111) planes can be grown on (0001) surfaces of hexagonal substrates. This suggests that growth parameters would play a very important role. Since we have studied samples with wurtzite structure, from now on we will focus mainly on wurtzite structure.

Figure 1.1 shows a hexagonal unit cell of wurtzite structure [13]. It is defined by three parameters: edge length \mathbf{a} of the basal plane (0001), height of the prism \mathbf{c} and internal parameter \mathbf{u} as the anion-cation bond length along [0001] direction. In a Cartesian frame of reference [13], considering $(\hat{e}_x, \hat{e}_y, \hat{e}_z)$ as the orthonormal basis vectors, primitive translation vectors a_1, a_2 and a_3 can be expressed as

$$a_1 = a_r \hat{e}_x \quad (1.1)$$

$$a_2 = -\frac{1}{2}a_r \hat{e}_x + \sqrt{\frac{3}{2}}a_r \hat{e}_y \quad (1.2)$$

$$a_3 = c_r \hat{e}_z \quad (1.3)$$

1.1.1 Lattice constants of binary compounds

The bulk lattice constants \mathbf{a} and \mathbf{c} of all the binary nitrides dealt with in this study: GaN, AlN and InN are shown in Table 1.1. One can notice that there exists a large difference exists in lattice constant \mathbf{a} of the binary alloys. This is often referred to as ‘lattice mismatch’.

TABLE 1.1: bulk lattice parameters of wurtzite hexagonal structure of GaN, AlN and InN

	GaN	AlN	InN
$a(\text{\AA})$	3.187	3.112	3.548
$c(\text{\AA})$	5.184	4.982	5.760

1.1.2 Lattice constants of ternary compounds

Vegard’s law

According to this law, the lattice constants a and c of an alloy $A_x B_{1-x} N$ can be related to the lattice constants of their binary constituents AN and BN by

$$a(A_x B_{1-x} N) = x \cdot a(AN) + (1 - x) \cdot a(BN) \quad (1.4)$$

$$c(A_x B_{1-x} N) = x \cdot c(AN) + (1 - x) \cdot c(BN) \quad (1.5)$$

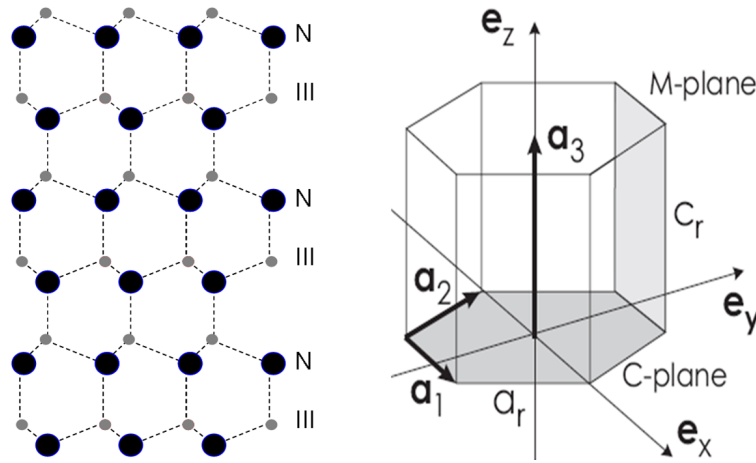


FIGURE 1.1: (a) arrangement of atoms in a wurtzite structure along c-axis (b) hexagonal unit cell of wurtzite structure

Here A and B indicate two generic cations among In, Al, and Ga such that their possible binary constituents would be GaN, AlN and InN. This law is usually found to work for structural properties in ternary alloys. The good agreement between the Vegard's law and the calculations performed by Bernardini et al. [14] using ab initio density functional techniques on the lattice parameters suggest the same (see figure 1.2), independent of chemical ordering (CH-like, CP-like) and disordering (random) of group-III atoms. The chemical ordering will be defined in the next section.

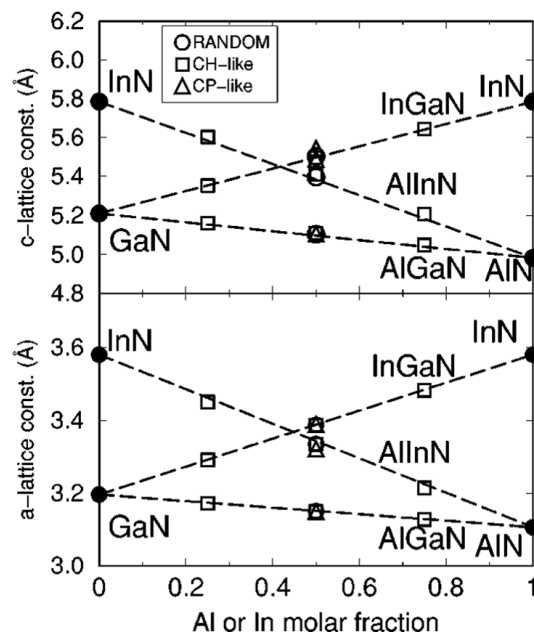


FIGURE 1.2: Basal (a) and axial (c) lattice constants of wurtzite-based nitride alloys. Directly calculated values for various alloy structures are denoted by open circles (random), squares (CH and LZ), and triangles (CP). The dashed lines are Vegard's law. (from Bernardini et al. [14])

1.2 Disordering in nature

In a wurtzite structure of group III-nitrides, the anion site is always occupied by a N atom but the question arises what will decide which group-III element would preferentially occupy a cation site and if it is controllable. For calculations, fully disordered (random) and the following partially ordered alloy structures are considered, as they have been observed before:

CuPt-like structure (CP): 1x1 super-lattice structures oriented along [0001] direction with alternating planes of group III elements, e.g. Al (In) with Ga plane. It is stable at the alloy surface.

Chalcopyrite-like structure (CH): Each anion is surrounded by two cations of one species and two of the other. It is a thermodynamically stable bulk structure and the most homogenous for a given composition.

Luzonite (LZ): Each nitrogen atom is surrounded by three out of four cations are of same element.

The occurrence of these structures is dependent on the thermodynamics and kinetics of growth. Thus, it is of major importance to know the equilibrium structures required for the calculations and modeling of devices as polarization properties would heavily depend on them, and thus the electrical properties.

1.2.1 AlGaN system

Korakakis et al. [15] reported ordering in this system along the c axis, where the Ga and Al atoms separately occupy the two simple hexagonal sub-lattices of the wurtzite system, giving rise to the lower symmetry P_{3m1} space group. This was demonstrated using XRD technique on 1 μm thick film of AlGaN where (0001) reflections to an ordered ternary system were observed. (0001) reflection in general is forbidden in random ternary alloy. However, the co-existence of three different kinds of chemical ordering (1:1, 3:1 and also 10:2 related to AlN/GaN, $Al_{0.25}Ga_{0.75}N/GaN$ and $Al_{0.16}Ga_{0.84}N/GaN$, respectively) in high quality AlGaN systems was reported by Ruterana et al. [16] using electron diffraction and x-ray techniques.

1.2.2 InGaN system

Theoretical studies by Ho and Stringfellow [17] have shown that the $In_xGa_{1-x}N$ ternary system is not thermodynamically stable. According to them, for $In_xGa_{1-x}N$ grown at

800°C, the solubility limit is $x \approx 0.06$ and the spinodal composition is $x \approx 0.22$. Consequently, decomposition at the spinodal could occur in the form of clustering, phase separation, and ordering, which is governed by the growth kinetics. N.A.El-Masry et al. [18] reported the occurrence of phase separation for InGaN films with $\text{InN} > 0.28$. The evidence of phase separation is shown in figure 1.3. Figure 1.3(a) is a single phase $\text{In}_{0.1}\text{Ga}_{0.9}\text{N}$ and 1.3(b) is a multiphase $\text{In}_{0.49}\text{Ga}_{0.51}\text{N}$. The details of the technique are described in M. K. Behbehani [19]. However, Ruterana et al. [20] observed that the In and Ga atoms occupy, respectively, the two simple hexagonal sublattice sites related by the glide mirrors and helicoidal axes of the P_{63mc} symmetry group of the wurtzite GaN, suggesting the presence of ordering and a possibility of fabrication of InGaN with at least 50% InN.

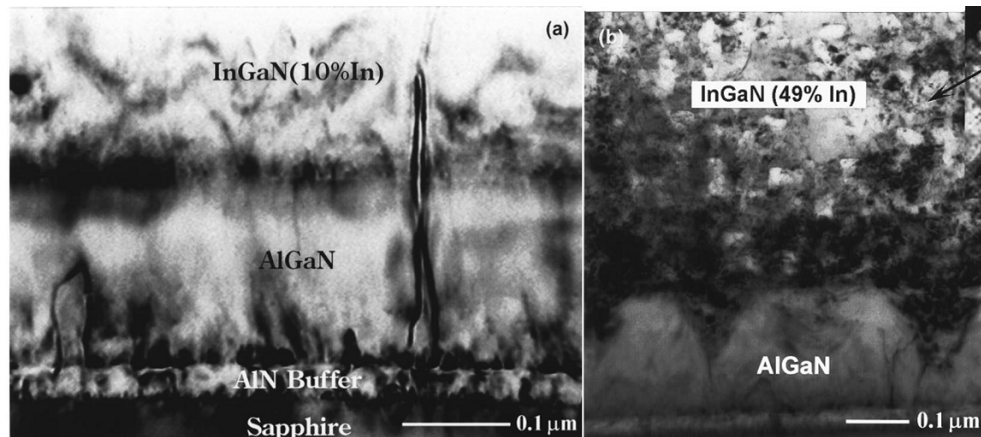


FIGURE 1.3: (a) single phase InGaN with 10% InN (b) multiphase InGaN with 49% InN. (from El-Masry et al. [18])

1.3 Band structure

One of the most important aspects of the group III-nitrides is their direct-band gap nature and the size of the energy gap, hence, named *wide band gap materials*. In their stoichiometric systems, 50% of the constituents consist of nitrogen (N) and the other half is made of metal constituents. This stoichiometry is same in both wurtzite and zincblende forms of nitrides. However, there is a another kind known as *dilute nitrides* where small amounts of N are added to the lattice for remarkably large negative bowing of the band gap making their system to compete for longer wavelength applications.

The band structure of any given semiconductor is pivotal in determining its potential utility in the modeling and the development of devices. Consequently, an accurate

knowledge of the band structure is critical if the semiconductor in question is to be incorporated. This has resulted in a demand for experimental and theoretical studies. Though they have established reliable values for quantities such as lattice parameters and fundamental band gaps, still many other parameters remain uncertain. Most of the theoretical research concentrates on providing parameters of band structure, especially those related to the effective masses of electrons and holes as well as the behavior and splitting of the valence band at the edge.

1.3.1 Conventional signs

When the propagation direction k of the excitation light is parallel to the c axis and the light is thus, polarized perpendicular to the c axis (also called alpha polarization) hence, it is denoted as $E \perp c$, where E denotes the electric field component of the light. Generally, this is the case for most of the optical measurements such as absorption, transmission, and reflectance. Whereas, when k is perpendicular to the c axis, component E of the light is parallel to c , hence, it is denoted as $E \parallel c$. When dealing with the band structures, the symbols \perp and \parallel assigned to indices of effective mass parameters denote the Γ -M (or \perp to c -axis) and Γ -A (or \parallel to c -axis) directions, respectively.

1.3.2 Introduction on theoretical calculation of band structure

Device modeling, optimization and many calculations of optical gain in bulk nitride materials and in quantum well structures rely on the valence- and conduction-band structures and transport parameters. The electronic band structures of nitrides could be obtained from atomistic ab initio methods such as first principle total energy calculations within local density functional approximations (LDA) [21] and full-potential linearized augmented plane-wave method (FLAPW) [22] or empirical and/or pseudopotential methods such as empirical pseudopotential method (EPM) [23] and empirical tight-binding method (ETBM) [24]. There are also phenomenological methods such as the $k \cdot p$ theory [21] that are often used. From these methods, band-structure parameters (especially valence band parameters) such as the splitting energies (e.g. crystal-field splitting energy, the spin-orbit split-off energies), the band-edge effective-mass parameters, Luttinger-like parameters, the deformation potential are extracted by a fitting procedure with the band-edge dispersion curve.

1.3.3 k.p theory

For electronic and optical properties, the band structure near the direct band edges can be used to understand experimental observations such as the photoluminescence spectrum and mobility measurements. Using the k.p method one can obtain analytical expressions for the band dispersion and the effective masses. It allows the extrapolation of the band structure over the entire Brillouin zone from the energy gaps and optical matrix elements at the zone center. Of these band structure calculations, the $k \cdot p$ method using six or eight bands is one that is specially useful for device modeling because the computational demands are light compared to other methods, such as those based on empirical pseudopotentials. The k.p approach is known to provide a good description of the heavy-hole, light-hole, and crystal field split-off bands at the zone center, which are important in any consideration of optical properties. Therefore, there is a need to obtain accurate k.p parameters for these wurtzite compounds and their alloys, in order to model current and future devices.

1.3.4 An overview of the full Band structure

Figure 1.4 shows the electronic band structure of WZ GaN calculated using empirical pseudopotential approach where the energy dispersions are shown along high symmetry lines of the first BZ [25]. The energy bands consist of four parts: three occupied bands and an unoccupied band. They originate from various orbital states and their hybridization. In GaN, these include states such as N2s, N2p, Ga4s, Ga4p and Ga3d. For instance, in the second lowest energy bands located between 0.55 Ryd and 0.38 Ryd, the lower energy side originates from the Ga3d well-localized states, and the upper side from the hybridized states between the Ga3d and the N2s states [26]. This can be applied in a similar fashion to AlN. However, due to difference in electronic structure of the cations in GaN and AlN, there is significant difference in their respective band structure. For example, in AlN, there is no hybridization between the cation d and the N 2s states due to absence of d electrons in Al atom in the ground state. Consequently, the lowest energy band is combined with the upper side of the second lowest one, and these two bands become one narrow band. The conduction bands are separated from the valence bands by ~ 0.14 Ryd at the $\Gamma - point$ (also referred to as conduction band minimum CBM). The vicinity of the CBM originates from the s states of N and Ga (N 2s and Ga 4s states). Comparing the band structure of AlN with that of GaN, the main features in these two energy regions are similar, except the order of energy levels around the VBM.

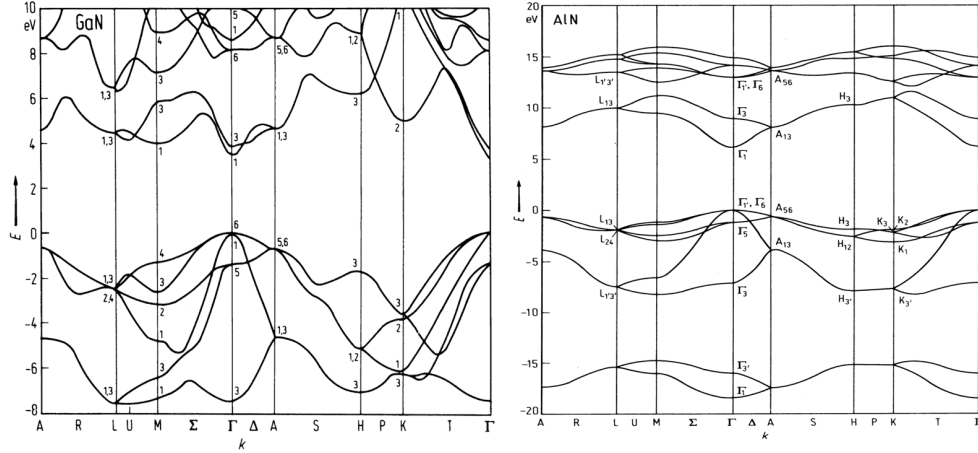


FIGURE 1.4: Band structure of wurtzite GaN (left) and AlN (right) [25]

Essential parameters that define the band structure (near the Γ – *point*) and determine the optical transitions of the material and optical devices, can be extracted experimentally and compared with the ones derived theoretically. The valence band of the wurtzite structure is strongly coupled between heavy holes (hh-), light holes (lh-), and crystal-field split-holes(ch-) in the bulk. In the band structure of GaN, the order of the valence bands in increasing order of their transition energies, are $\Gamma_{-9vbm}(A)$, $\Gamma_{-7v}(B)$, $\Gamma_{-7v}(C)$ as shown in figure 1.5. But the order of the valence bands in AlN is different from that of GaN, given as $\Gamma_{-7vbm}(A)$, $\Gamma_{-9v}(B)$, $\Gamma_{-7v}(C)$, see figure 1.5. Because of the large energy separation between the valence band maximum and the second and third valence states, fundamental optical transitions near the Γ – *point* and transport properties of the free holes are predominantly determined by the top valence band, i.e. Γ_{-9vbm} band in GaN and Γ_{-7vbm} in AlN.

TABLE 1.2: Table of eigenenergies, spin-orbit splitting energies of GaN and AlN

	GaN	AlN
$\Gamma_1^c - \Gamma_6^v$	3.47	6.11
$\Gamma_6^c - \Gamma_1^v$	0.023	-0.16
$\Gamma_6^c - \Gamma_3^v$	6.94	6.41
Δ_{SO}	0.011	0.018
Δ_{CF}	0.038	-0.219

Such an ordering of valence bands is consequently affected by the crystal field splitting. A significant difference in crystal-field splitting of GaN and AlN is seen, in terms of their polarity and magnitude: a negative crystal-field splitting (-219 meV) in AlN and a positive value (38 meV) in GaN. This is due to the fact that AlN, being more

ionic, has a smaller c/a ratio (1.601) and a larger u (0.3819), when compared to 1.626 and 0.3768, respectively of that of GaN. Here, u is a dimensionless cell-internal coordinate that in WZ structure that distinct the two nearest-neighbor anion-cation bond length. For an ideal WZ structure with $c/a = \sqrt{8/3}$ and $u = 0.375$, the two bond lengths are equal. Neglecting this effect in calculations can lead to large errors. This larger structural distortion in AlN also explains why WZ AlN has a smaller band gap than ZB AlN, where as for all the other binary semiconductors the opposite trend exists.

Another of its significant affect is on the optical transitions that are determined by the dipole transition matrix elements [27]. The matrix elements given by

$$I = |\langle \Psi | p | \Psi \rangle|^2 \quad (1.6)$$

for the transitions between the conduction state and the three valence states at Γ -point of AlN for differently polarized lights ($E \perp c$ and $E \parallel c$) are listed in the table 1.3. One may obtain the matrix elements for arbitrary light polarization from the relation,

$$I(\theta) = \cos^2(\theta) \cdot I(E \parallel c) + \sin^2(\theta) \cdot I(E \perp c) \quad (1.7)$$

where θ is the angle between E and the c axes.

As shown in the table 1.3, recombination between the conduction band electrons and the holes in the top most valence state (Γ_{7vbm}) is almost prohibited for $E \perp c$, whereas the recombination between the conduction band electrons and holes in the (Γ_{9v} and (Γ_{7v} or C) valence bands are forbidden for $E \parallel c$. This is in sharp contrast to GaN in which the theoretical and experimental results have shown that the recombination between the conduction band electrons and the holes in the top most valence band (Γ_{9vbm}) is almost prohibited for $E \parallel c$ (see table 1.4). This has very sharp implications on the band gap determined experimentally. The transition between the Γ_{7c} and the top valence band Γ_{7vbm} , which determines the minimum energy gap of AlN, is not active for $E \perp c$. Therefore, this type of optical measurement cannot obtain the true fundamental band gap of AlN. Instead, it measures the energy gap between the conduction band and the B (or C) valence band because these transitions are active for alpha polarization. This explains why larger band gaps, about 6.3 eV, were reported in earlier measurements, whereas the value of 6.11 ± 0.01 eV is obtained here by PL. This is in contrast to the case for GaN epilayers, in which the emission to the top most valence band is allowed

for alpha-polarization. Thus, different optical measurements would generally yield the same band gap value in GaN.

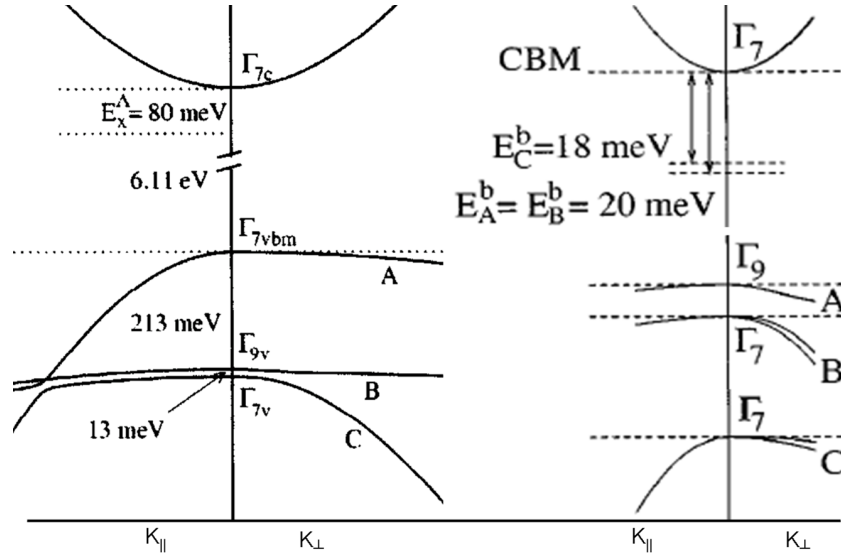


FIGURE 1.5: Calculated band structure of AlN (left) from ref. [28] and GaN (right) from ref. [29] at Γ -point shows the top of the valence band is split by crystal field and spin orbit coupling into the $\Gamma_{7vbm}(A)$, $\Gamma_{9v}(B)$, and $\Gamma_{7v}(C)$ states. The sign \perp (\parallel) denotes the direction perpendicular (parallel) to the [0001] direction of the AlN epilayer. The A band exciton binding energy is denoted as E_x^A .

TABLE 1.3: Square of the dipole transition matrix elements I of AlN for light polarized parallel ($E \parallel c$) and perpendicular ($E \perp c$) to the [0001] (from ref. [28])

Transition	$I(E \parallel c)$	$I(E \perp c)$
$\Gamma_7^c \leftrightarrow \Gamma_7^{vbm}$	0.4580	0.0004
$\Gamma_7^c \leftrightarrow \Gamma_9^v$	0.0	0.2315
$\Gamma_7^c \leftrightarrow \Gamma_7^v$	0.0007	0.2310

TABLE 1.4: Square of the dipole transition matrix elements I of GaN for light polarized parallel ($E \parallel c$) and perpendicular ($E \perp c$) to the [0001] (from ref. [29])

Transition	$I(E \parallel c)$	$I(E \perp c)$
$\Gamma_7^c \leftrightarrow \Gamma_7^{vbm}$	0	1
$\Gamma_7^c \leftrightarrow \Gamma_9^v$	0.053	0.974
$\Gamma_7^c \leftrightarrow \Gamma_7^v$	1.947	0.026

1.4 Polarization

The distribution of free carriers and the magnitude of electric currents in a semiconductor are determined by electric fields. In a semiconductor structure, such as a Si-based junction, the field is of external origin. The electric field inside the structure is determined by, e.g., the applied voltage, which is screened by electrons and nuclei of the solid. In ferroelectrics, pyroelectrics, and piezoelectrics, an internal field may exist even in the absence of the external field, due to the presence of non-vanishing electric polarization. Some basic relationships on polarization are briefly recalled below from ref. [30].

In a bulk homogeneous insulator, the electric field E , polarization density P , and the electric field displacement D are related by:

$$D = \varepsilon E + 4\pi P \quad (1.8)$$

where ε is the static dielectric constant of the insulator.

According to Poisson's equation, D is determined by the external electric charge density $qn(r)$:

$$\text{div}D = 4\pi qn(r) \quad (1.9)$$

where q is the elementary charge.

With the continuity condition at the surface or interface, 1.9 would yield

$$\Delta \cdot D = (D_2 - D_1) \cdot i = 4\pi\sigma \quad (1.10)$$

where σ represents the surface or interface charge density of external origin, i is the unit vector normal to the surface and D_2 is outside and D_1 inside the solid.

This shows that when $P = 0$ and surface charge density σ is of external origin, change in the displacement is directly related to σ .

When the polarization is present, its discontinuity (at surface or interface between two dielectrics) is related to the polarization surface charge density σ_p by [30]

$$\Delta \cdot P = \sigma_{pol} \quad (1.11)$$

Equations 1.8 to 1.11, suggests that in the absence of external charges at interfaces, discontinuities of the field and the polarization are related by

$$\Delta \cdot E = -\pi \delta P \cdot i \quad (1.12)$$

Similarly, the discontinuity of the electrostatic potential ϕ is determined by the dipole layer at the surface (or interface) and is given by

$$\Delta \phi = 4\pi \delta \quad (1.13)$$

where δ is the surface dipole density.

Clearly, as already indicated, the continuity equations apply both to free surfaces and to interfaces in heterostructures and superlattices.

1.4.1 Spontaneous polarization

Each unit cell can be considered to contain a charge dipole formed from the spatial separation of the barycentre of the negative charge from the electron cloud and the positive charge due to the nuclei. In a perfectly organized structure of layers of unit cells, the dipoles in every unit cells can neutralize each other in the bulk of the semiconductor, but would form a sheet charges $\pm\sigma_\pi$ on the surface or interface. For example, in case of GaN a free Ga-face surface develops a negative sheet charge, and a free N-face surface develops a positive sheet charge [30]. In spite of no charge in the bulk of the semiconductor, surface charges can cause high electric field in the bulk of the semiconductor. From Gauss's law, this field can be estimated as

$$F_\pi = \frac{\sigma_\pi}{e} \quad (1.14)$$

where σ_π is the sheet charge density and ϵ is the permittivity. The presence of mobile charges may cause charge redistribution so as the net field is no more dependent on the bound charges, only. This has a very significant role in the formation of two-dimensional electron gas (2DEG) in HEMT structures or red or blue-shift observed in emission from multi-quantum wells (MQWs), which will be discussed later. These mobile charges or free carriers could be associated to doping, impurities or even photo-excited carriers. An approximate value of this charge is around 10^{13} cm^{-2} . Considering the atomic sheet density in nitride semiconductors to be 10^{15} cm^{-2} , roughly one in 100 atoms contribute to spontaneous polarization charge. [30]

1.4.2 Piezoelectric polarization

A second type of polarization is often present in nitrides, closely related to the piezoelectric effect. Direct piezoelectric effect is defined as the creation of polarization when a mechanical stress is applied to a dielectric material. Biaxial strain is inherently present in heterostructures of nitrides due to large differences in lattice constants of AlN, GaN, InN and their alloys.

Piezoelectric polarization P_{PEi} is defined as the linear combination of all the strain tensors using well defined piezoelectric tensors or coefficients e_{ijk} as shown below

$$p_i = e_{ijk} \cdot \epsilon_{ijk} \quad (1.15)$$

where e_{ijk} is a third rank tensor.

In general, strain tensors consist of 9 components and piezoelectric tensor e_{ijk} consists of 3×9 components. Due to its symmetry, strain tensor and piezoelectric tensor can be contracted to 3×9 components. In wurtzite structures that have high symmetry, equation 1.15 further simplifies to three independent components e_{13} , e_{33} and e_{15} .

$$\begin{pmatrix} p_x \\ p_y \\ p_z \end{pmatrix} = \begin{pmatrix} 0 & 0 & 0 & 0 & e_{15} & 0 \\ 0 & 0 & 0 & e_{15} & 0 & 0 \\ e_{31} & e_{31} & e_{33} & 0 & 0 & 0 \end{pmatrix} \begin{pmatrix} \epsilon_x \\ \epsilon_y \\ \epsilon_z \\ \epsilon_{yz} \\ \epsilon_{xz} \\ \epsilon_{xy} \end{pmatrix}$$

The relevant relationship for the piezoelectric polarization along [0001] direction can now be expressed as

$$P_Z = P_{PE} = e_{33} \cdot \varepsilon_z + e_{31} \cdot (\varepsilon_x + \varepsilon_y) \quad (1.16)$$

where $\varepsilon_z = \frac{(c-c_0)}{c_0}$ is the strain along the c axis, $\varepsilon_x = \varepsilon_y = \frac{(a-a_0)}{a_0}$ is the in-plane strain that is assumed to be isotropic, e_{33} , e_{31} are the piezoelectric coefficients, a and c are the lattice constants under strain, and a_0 and c_0 are the lattice constants of the relaxed material.

The relation between the lattice constants in the hexagonal wurtzite system is given by

$$\frac{(c - c_0)}{c_0} = 2 \frac{C_{13}}{C_{33}} \frac{(a - a_0)}{a_0} \quad (1.17)$$

where C_{13} and C_{33} are elastic constants.

Using Eqs. (1) and (2), piezoelectric polarization along [0001] can be expressed as

$$P_{PE} = e_{33} \frac{C_{13}}{C_{33}} + 2e_{31} \frac{(a - a_0)}{a_0} \quad (1.18)$$

In the absence of external fields, the total polarization P is the sum of the spontaneous P_{PZ} and strain induced piezoelectric polarization P_{PE} .

$$P = P_{SP} + P_{PE} \quad (1.19)$$

All the important polarization parameters of the three binary compounds AlN, GaN and InN required in various calculations are summarized in table 1.5. Presence of strong polarization in nitrides can have both advantages and disadvantages for electronic and optoelectronic devices based on heterostructures. This would be discussed in the next section.

TABLE 1.5: Lattice constants and polarization parameters of AlN, GaN and InN [31]

	AlN	GaN	InN
$P_{SP}(C.m^{-2})$	0.081	0.029	0.032
$e_{33}(C.m^{-2})$	1.46	0.73	0.97
$e_{31}(C.m^{-2})$	0.6	0.49	0.57
$C_{13}GPa$	108	103	92
$C_{33}GPa$	373	405	224
$a_0(\text{\AA})$	3.112	3.189	3.540
$c_0(\text{\AA})$	4.982	5.185	5.705
u	0.380	0.376	0.377

1.4.3 Polarization in ternary alloys

Using Vegard's law, spontaneous polarization in a ternary alloy can be given as

$$P_{SP}(A_xB_{1-x}N) = xP_{SP}(AlN) + (1-x)P_{SP}(BN) \quad (1.20)$$

As per calculations and measurements by Ambacher et al. for $Al_xGa_{1-x}N$, this could be approximated to

$$P_{SP}(x) = (-0.052x - 0.029) \frac{C}{m^2} \quad (1.21)$$

However, this is not true for In-containing ternary alloys. As pointed out by Bernardini and Fiorentini et al. [32] the cause of bowing of SP is attributed to two effects:

- (1) The non linear dependence of the polarization on hydrostatic stress caused by the lattice mismatch between the alloy's binary components (tensile for Al and compressive for In)
- (2) Microscopic piezoelectric effect caused by the atomic size mismatch of the group III elements causing shrinkage or elongation of the average atomic bond size, also referred to as "bond alternation".

And these two factors, lattice and atomic size mismatch are significant in those ternary alloys which are constituted of either AlN and InN or GaN and InN. So, this nonlinear behavior is very pronounced in AlInN and InGaN and could be neglected in AlGaIn.

As shown in their work (fig.1.6), the deviation of polarization from Vegard's law for different alloy composition is significantly higher for In-containing partially ordered alloys and can be taken into account by the bowing factor b in the equation below

$$P_{SP}(A_xB_{1-x}N) = xP_{SP}(AlN) + (1-x)P_{SP}(BN) + bx(1-x) \quad (1.22)$$

Their results can be summarized as

- (1) The bowing, in general, is quite high for CP- structures w.r.t CH- structures in AlInN and InGaN. For example, bowing is +0.193 for CP-InGaN and less than 0.023 for CH-InGaN.
- (2) In random alloys, polarization deviates from the Vegard's law by not more than a maximum of 10% for all alloy composition, with an exception for AlInN.
- (3) In comparison to both AlInN and InGaN, AlGaN is the least affected by any kind of ordering.

Owing to such a large dependence of polarization on chemical order, it describes the importance of the structural arrangement to exactly calculate polarization induced charge (will be discussed in the next section “polarization at interfaces”).

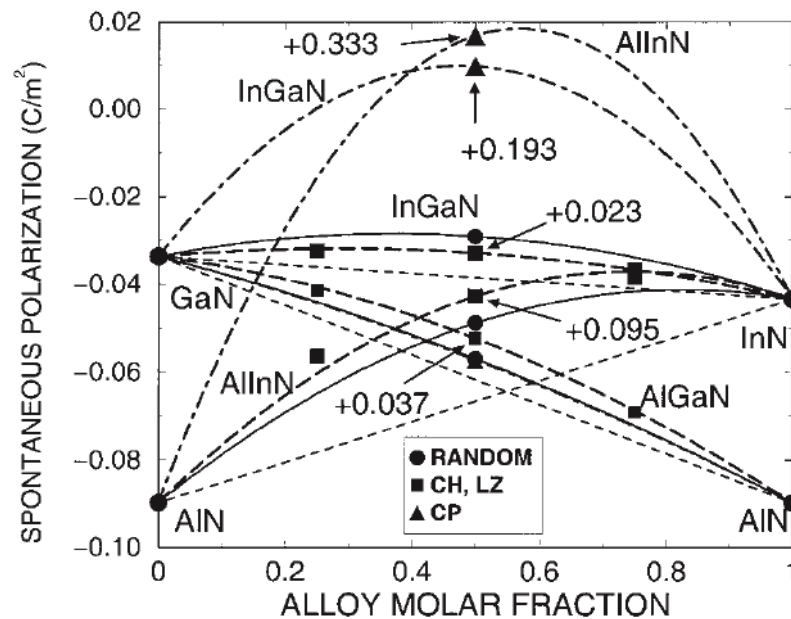


FIGURE 1.6: Spontaneous polarization against alloy molar fraction of InGaN, AlInN and AlGaN. Straight dashed curves, solid curve (filled circle), dashed curve (triangle) and dashed curve (square) refer to Vegard's law, random, CP- and CH-like structures. Values pointed at different curves represent their bowing parameters (Bernardini et al. [32])

Also, piezoelectric polarization in ternaries suffers from nonlinearity. For random alloys, though piezoelectric coefficients have a linear dependence on alloy composition, they are strongly dependent on the strain state. So, piezoelectric components can be still be

interpolated from Vegard's law, provided that the non-linearity of the binary constituents on the strain state is taken into account by the following equations:

$$P_{SpIN}^A = -1.808\varepsilon_1 + 5.624\varepsilon_1^2 \quad for \varepsilon < 0 \quad (1.23)$$

$$P_{SpIN}^A = -1.808\varepsilon_1 - 7.888\varepsilon_1^2 \quad for \varepsilon > 0 \quad (1.24)$$

$$P_{SpIN}^A = -0.918\varepsilon_1 + 9.541\varepsilon_1^2 \quad (1.25)$$

$$P_{SpIN}^A = -1.373\varepsilon_1 + 7.559\varepsilon_1^2 \quad (1.26)$$

$$(1.27)$$

where

$$\varepsilon(x) = \frac{a^{GaN} - a(x)}{a(x)} \quad (1.28)$$

For partially ordered structures, moderate negative bowing of the piezoelectric coefficients is induced, and the PE is reduced in comparison to the random alloy for the same composition. Figure 1.7 shows the piezoelectric polarization computed for random and partially ordered structures [Bernardini et al.] for different alloys. It is important to note that structural ordering has no affect on the polarization behavior in AlGaIn.

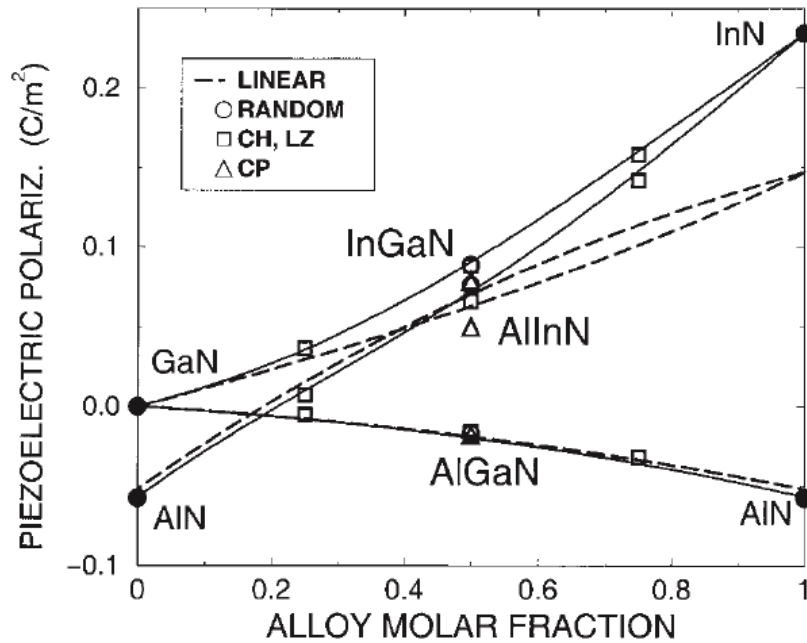


FIGURE 1.7: Piezoelectric polarization against alloy molar fraction of InGaIn, AlInN and AlGaIn. Dashed curves, solid curve (open circle), solid curve (triangle) and solid curve (square) refer to Vegard's law, random, CP- and CH-like structures. (from Bernardini et al. [32])

1.4.4 Polarization at interfaces of heterostructures

Polarization in bulk III-Nitrides results in the presence of electric field. The macroscopic potential and the charge distribution of the system consisting of single- and multi-heterojunctions, can be described by equations 1.8-1.12. The heterojunctions or the interface is usually found to be associated with the dipoles, which contributes to discontinuities in electrostatic potential and the band offsets. And the presence of polarization, would determine the charge densities accumulated at interfaces.

For pseudomorphic $Al_xGa_{1-x}N/GaN$ ($0 < x \leq 1$) and $Al_{1-x}In_xN/GaN$ ($0.71 < x \leq 1$) heterostructures grown along (0001), the polarization induced interface charge (bound sheet charge $+\sigma/e$) is positive. As a result, free electrons accumulate at the interface to compensate these charges. Due to high magnitude of polarization in III-nitrides, this process of compensation leads to formation of high density 2DEG. Compared to 2DEG in AlGaAs/GaAs, modulation doped barrier is not required. Though the origin of electron concentration in 2DEG region is still under debate in undoped heterostructures, surface states and residual carrier concentration of the bulk of GaN are considered to be the two prominent factors [33].

2DEG in HEMT structures As explained before, polarization induced positive sheet charge $\sigma(z)$ bounded at the Ga(Al)-face AlGa_N/GaN or N-face GaN/AlGa_N interface is compensated by the free electrons of the system. For Ga-face AlGa_N/GaN structures, the sheet electron concentration n_s accumulated near the interface can be approximately calculated from electrostatics as

$$n_s = \frac{\sigma}{e} - \frac{\varepsilon_0 \varepsilon_{AlGaN}}{d_{AlGaN} e^2} [e\phi_0 + E_F - \Delta E_C] \quad (1.29)$$

where ε is the relative dielectric constant of $Al_xGa_{1-x}N$, d_{AlGaN} is the thicknesses and $e\phi_b(z)$ is the Schottky barrier of the barrier layer AlGa_N (boundary condition), $E_F(z)$ is the Fermi level w.r.t the conduction band, and ΔE_C is the conduction band offset at the AlGa_N/GaN interface where a 2DEG forms.

As shown in the equation 1.29, sheet carrier concentration can be significantly modulated by changing at least two factors, $\sigma(z)$ and d_{AlGaN} . As $\sigma(z)$ is polarization induced bound charge, would depend on both spontaneous and piezoelectric polarization of AlGa_N layer, which would increase with increase in Al-content (see fig 1.8). However, this beneficial property of using high Al-content in AlGa_N is constrained by its critical thickness.

One may notice in equation 1.29 that as $\sigma(z)$ would increase, $d_{AlGaN,critical}$ would dramatically reduce and thus, a very high sheet carrier density cannot be achieved. AlGaN layers with high Al-content are often partially relaxed. The affect of relaxation is shown by Ambacher et al. in figure 1.8. In the figure, relaxation is defined as $r(x)$,

where

$$r(x) = \frac{a(x) - a(GaN)}{a_0(x) - a(GaN)} \quad (1.30)$$

In the case of doped AlGaN/GaN heterostructures, donor atoms contribute to the increment in sheet carrier concentration. This can also be described in the second term of the equation, which would reduce as the Fermi level lifts towards the conduction band. This is also well demonstrated in the study by Ambacher et al. for doped and undoped structures.

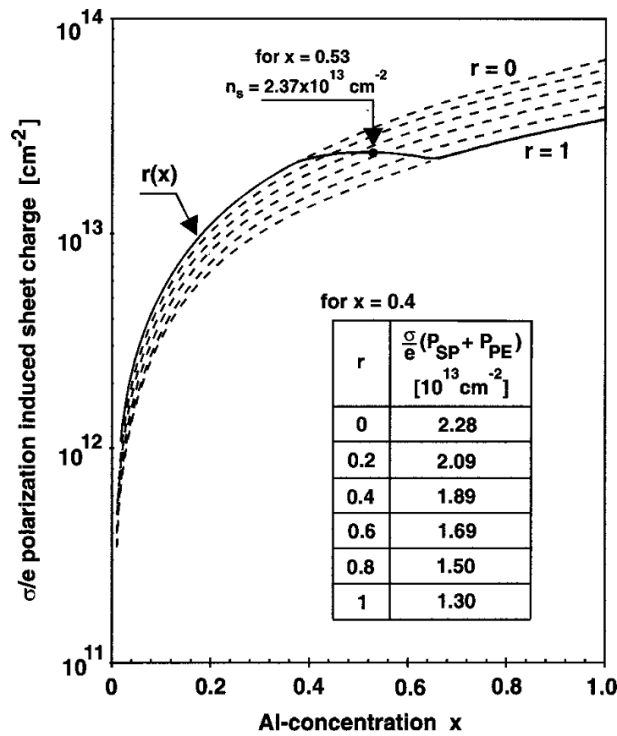


FIGURE 1.8: Calculated net polarization induced sheet charge, σ/e for pseudomorphically grown AlGaN/GaN heterostructures vs Al concentration. Here, r represents degree of relaxation, where $r=0$ states pseudomorphic growth and $r=1$ states fully relaxed AlGaN [from Ambacher et al. [34]]

It is quite clear here, independent of the extent of relaxation and doping of the barrier layer, one can still achieve high carrier density in the channel and high electron mobility

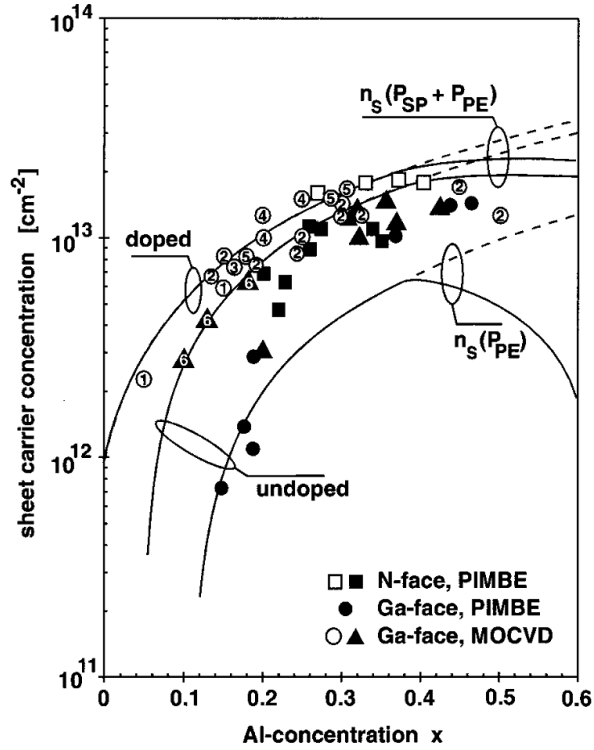


FIGURE 1.9: Calculated sheet carrier concentrations n_s for pseudomorphic (dashed lines) and partially relaxed $Al_xGa_{1-x}N/GaN$ HEMT structures. The upper two curves are net polarization induced n_s for doped and undoped barriers, respectively. The sheet carrier concentration induced by only piezoelectric polarization of the barrier $n_s(P_{PE})$ is shown for comparison (lower curve). Symbols are experimental data. $d_{AlGaN} = 20 \text{ nm}$, $T=300 \text{ K}$. [from Ambacher et al. [34]]

devices owing to strong polarization fields.

Quantum Well Nitride QW structures are of considerable technological interest for compact solid-state lighting devices and high-density optical storage. In general, a quantum well is synthesized from two semiconductors of different band gap, where the one with higher band gap would act as the barrier and one with lower would be the well. When the well thickness is sufficiently low, size quantization occurs and carriers occupy discrete levels in the conduction band and valence band of the well. This is can be understood from the infinite well approximation, where the quantum energies of the carriers are given by

$$E_n = \frac{\hbar^2}{2m^*} \left(\frac{(n+1)\pi}{L} \right)^2 \quad \text{for} \quad n = 0, 1, 2, \dots \quad (1.31)$$

And absorption edge in this case would be slightly higher than the band gap of the well:

$$E_{abs} = E_g + E_{0,e} + E_{0,h} \quad (1.32)$$

where, $E_{0,e}, E_{0,h}$ are the lowest subband energies of the carriers within the well.

The structure of a typical III- nitride-based MQW is configured as -C-A-C-A-C-A-C- where A and C represents active and cladding layers, respectively. In general, both the layers are strained in order to comply with the substrate in-plane lattice parameter. In these structures, the electric fields in the layers are caused by the fixed polarization charge. This built-in field superimposes with the compositional confinement potential of the MQW and is responsible for redshifts in the transition energies (Quantum-confined Stark effect) and suppression of interband transitions when the quantum well thickness is increased. Figure 1.10 shows the band diagram of $In_{0.2}Ga_{0.8}N/GaN$ MQW grown along [0001]. It is very clear that the electron and hole wavefunction do not overlap, but are spatially separated by few Å in the presence of polarization induced in-built electric field.

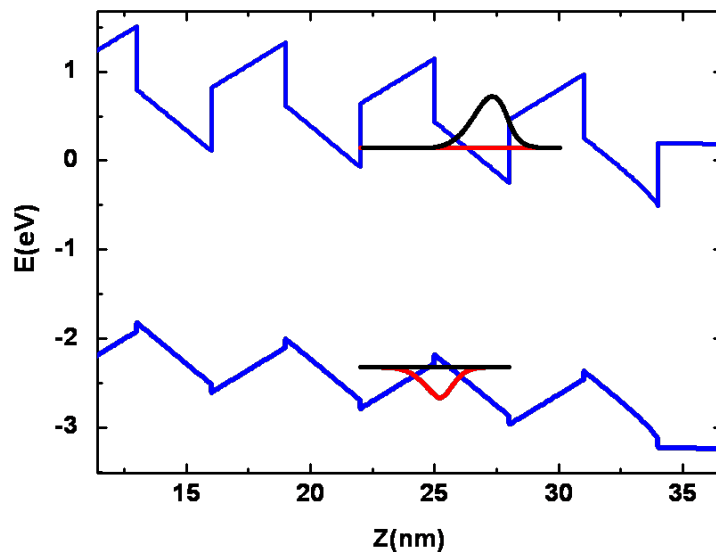


FIGURE 1.10: Simulated band diagram of $In_{0.2}Ga_{0.8}N/GaN$ MQW. Also shown is the electron and hole wavefunction function corresponding to the lowest subband.

Due to strong built-in polarization fields of an order of few order of MV/cm in wurtzite GaN-based QWs grown along the [0001] direction, the performance of the device is significantly degraded, particularly, optical gain and the luminescence is reduced by an order of magnitude when compared with other III-V semiconductors. This has motivated

for the growth and study of the quantum well structures on the non-polar or semi-polar planes.

Though the properties of III-nitrides are very promising for a wide number of applications, they suffer from structural deformations during the growth processes; few of them are still inevitable, such as threading dislocations, stacking faults and vacancies. They are often found to tamper with the emission properties and assist in degradation of the material and the device. This would be discussed in detail in the next chapter.

Bibliography

- [1] I. Gorczyca. *Solid state communications*, 79:1033, 1991.
- [2] T. Lei, M. Fanciulli, R. J. Molnar, T. D. Moustakas, R. J. Graham, and J. Scanlon. *Appl. Phys. Lett.*, 59:944, 1991.
- [3] M. J. Paisley, Z. Sitar, J. B. Posthill, and R. F. Davis. *J. Vac. Sci. Technol. A*, 7:701, 1989.
- [4] R. C. Powell, G. A. Tomasch, Y.-W. Kim, J. A. Thornton, and J. E. Greene. *MRS Proceedings*, 162:525, 1989.
- [5] H. Okumura, K. Balakrishnan, H. Hamaguchi, T. Koizumi, S. Chichibu, H. Nakanishi, T. Nagatomo, and S. Yoshida. *Journal of Crystal Growth*, 189:364, 1998.
- [6] T. Kurobe, Y. Sekiguchi, J. Suda, M. Yoshimoto, and H. Matsunami. *Appl. Phys. Lett.*, 73:2305–2307, 1998.
- [7] S. Y. T. Suemasu H. Tsuchiya, K. Sunaba and F. Hasegawa. *Jpn. J. Appl. Phys.*, 36:L1–L3, 1997.
- [8] K. Balakrishnan, G. Feuillet, K. ohta, H. Hamaguchi, H. Okumura, and S. Yoshida. *Jpn. J. Appl. Phys.*, 36:6221, 1997.
- [9] Y. Cui, V. K. Lazorov, M. M. Goetz, H. Liu, D. P. Robertson, M. Gajdardziska-Josifovska, and L. Li. *Appl. Phys. Lett.*, 82:4666, 2003.
- [10] J. W. Yang, J. N. Kuznia, Q. C. Chena, M. Asif Khan, T. George, M. De Graef, and S. Mahajan. *Appl. Phys. Lett.*, 67:3759, 1995.
- [11] Y. Zhao, C. W. Tu, I.-T. Bae, and T.-Y. Seong. *Appl. Phys. Lett.*, 74:3182, 1999.
- [12] A. Nagayama, R. Katayama, N. Nakadan, K. Miwa, H. Yaguchi, J. Wu, K. Onabe, and Y. Shiraki. *physica status solidi (a)*, 176:513, 1999.
- [13] C. Kittel. *Introduction to Solid State Physics*. Wiley, 7th edition edition, 1996.
- [14] F. Bernardini and V. Fiorentini. *Phys. Rev. B*, 64:085207, 2001.

- [15] D. Korakakis, K. F. Ludwig, and T. D. Moustakas. *Appl. Phys. Lett.*, 71:72, 1997.
- [16] P. Ruterana, G. De Saint Jores, M. Lagt, F. Omnes, and E. Bellet-Amalric. *Appl. Phys. Lett.*, 78:344, 2000.
- [17] I hsiu Ho and G. B. Stringfellow. *Appl. Phys. Lett.*, 69:2701, 1996.
- [18] N. A. El-Masry, E. L. Piner, S. X. Liu, and S. M. Bedair. *Appl. Phys. Lett.*, 72:40, 1998.
- [19] M. K. Behbehani, E. L. Piner, S. X. Liu, N. A. El-Masry, and S. M. Bedair. *Appl. Phys. Lett.*, 75:2202, 1999.
- [20] P. Ruterana, G. Nouet, W. Van der Stricht, I. Moerman, and L. Considine. *Appl. Phys. Lett.*, 72:1742, 1998.
- [21] S. K. Pugh, D. J. Dugdale, S. Brand, and R. A. Abram. *Semicond. Sci. Technol.*, 14:23–31, 1999.
- [22] E. Wimmer, H. Krakauer, M. Weinert, and A. J. Freeman. *Phys. Rev. B*, 24:864, 1981.
- [23] D. J. Dugdale, S. Brand, and R. A. Abram. *Physical Review B*, 61, 2000.
- [24] B. Jogai. *Solid State Communications*, 105:465–468, 1998.
- [25] B. Rezaei, A. Asgari, and M. Kalafi. *Physica B*, 371:107, 2006.
- [26] S. Nakamura and S. F. Chichibu. *Nitride Semiconductor Blue Lasers and Light Emitting Diodes*. CRC Press, 1st edition edition, 2000.
- [27] Claus Klingshirn. *Semiconductor Optics*. Springer, 3rd edition edition, 2006.
- [28] J. Li, K. B. Nam, M. L. Nakarmi, J. Y. Lin, H. X. Jiang, Pierre Carrier, , and Su-Huai Wei. *Appl. Phys. Lett.*, 83:5163, 2003.
- [29] G. D. Chen, M. Smith, J. Y. Lin, H. X. Jiang, Su-Huai Wei, M. Asif Khan, and C. J. Sun. *Appl. Phys. Lett.*, 68:2784, 1996.
- [30] C. Wood and D. Jena. *Polarization effects in Semiconductors: From Ab initio theory to device applications*. Springer.
- [31] O. Ambacher, R. Dimitrov, M. Stutzmann, B. E. Foutz, M. J. Murphy, J. A. Smart, J. R. Shealy, N. G. Weimann, K. Chu, M. Chumbes, B. Green, A. J. Sierakowski, W. J. Schaff, , and L. F. Eastman. *phys. stat. sol. (b)*, 216:381, 1999.
- [32] F. Bernardini and V. Fiorentini. *phys. stat. sol. (a)*, 190:65, 2002.

-
- [33] S. Pandey, D. Cavalcoli, B. Fraboni, A. Cavallini, T. Brazzini, and F. Calle. *Appl. Phys. Lett.*, 100:152116, 2012.
- [34] O. Ambacher, B. Foutz, J. Smart, J. R. Shealy, N. G. Weimann, M. Murphy K. Chu, A. J. Sierakowski, W. J. Schaff, L. F. Eastman, R. Dimitrov, A. Mitchell, and M. Stutzmann. *J. Appl. Phys.*, 87:334, 2000.

Chapter 2

Defects in III-Nitrides

2.1 Introduction

In III-V semiconductors such as arsenides and phosphides, the presence of dislocations is a very critical issue. They are known to act as non-radiative recombination centers, shortening the minority carrier lifetime. Since the efficiency of any optical device is dependent only on the radiative part of the recombination, presence of such non-radiative recombination centers were strongly correlated with the deterioration of the device. For example, in arsenide based LEDs, as the dislocation density spans from 10^3 cm^{-2} to 10^5 cm^{-2} , efficiency reduces by more than 50% and after reaching a density of 10^9 cm^{-2} there is almost no laser action. This is well evidenced in fig. 2.1 by Lester et al. [1] and shows how the efficiency of LEDs based on GaAs, GaP, GaAsP reduces dramatically by the dislocation density. Not only in LEDs but this is true in also other optoelectronic devices such as lasers. However, when they are compared to GaN-based LEDs, the minority carriers were extraordinarily insensitive to the presence of dislocations. As a result, in spite of consisting very high dislocation density, GaN-based LEDs were found to be highly efficient. Such a benign nature of dislocation could be attributed to the ionic nature of bonding in the III-V nitrides, which prevents dislocation and other structural defects such as stacking faults from acting as an efficient nonradiative recombination sites in these materials.

2.2 Threading dislocations

Threading dislocations occurring in hexagonal GaN along [0001] were found with a density reaching 10^{10} cm^{-2} [2],[3]. The main cause of such structural deformations is the significant mismatch between thermal expansion coefficients (α) and lattice constants

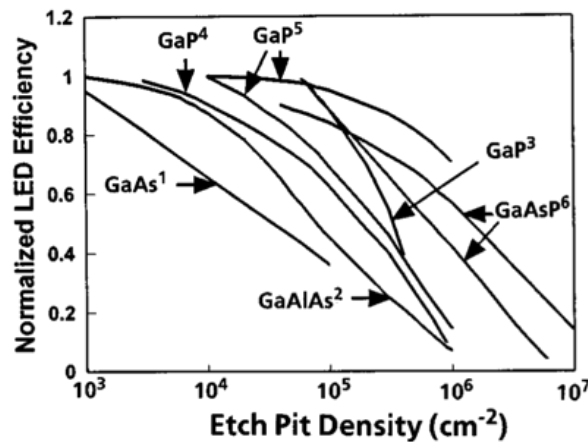


FIGURE 2.1: Dependence of LED efficiency (obtained from the paper cited below) on dislocation density for III-V devices

(a_0) between the nitride layer and substrates (such as Al_2O_3 , Si, SiC) or between two nitride layers. a_0 and α for different substrates and nitrides are given in table 2.1. Depending on their Burger's vector, they are classified as screw (c-type), edge (a-type) and mixed (a+c type) threading dislocations. In case of screw-type TD, Burger's vector is $1/3 \langle 0001 \rangle$ along the c-axis and for edge-type TD, it is perpendicular to the c-axis with Burger's vector as $1/3 \langle 11\bar{2}0 \rangle$. As the name suggests, mixed-type TD consist of both the components of edge and screw with Burger's vector as $1/3 \langle 11\bar{2}3 \rangle$. Their density is higher at the interface but reduces to 10^9 cm^{-2} as the thickness reaches $0.7 \mu\text{m}$ [4]. Other than their association with recombination centers, they also form current leakage paths in optical and electronic devices. So, a considerable effort is being given to reduce this density and ELOG (epitaxial laterally overgrown) GaN is one of the useful structures for this purpose. It is also possible to grow freestanding GaN substrates (usually grown by HVPE) to avoid threading dislocations in GaN but they suffer from its high manufacturing cost.

TABLE 2.1: Properties of nitrides along (0001) and various substrates. Here a , $\varepsilon_{\parallel, GaN}$ and α are in-plane equilibrium lattice constant, the biaxial strain of a GaN layer pseudomorphically grown on the respective nitride layers or substrate and thermal expansion coefficient (at 600K), respectively. Values are taken from Ref. [5], [6] and [7]

	<i>GaN</i>	<i>AlN</i>	<i>InN</i>	$Al_2O_3(0001)$	<i>6H - SiC</i>	<i>Si(111)</i>
$a(\text{\AA})$	3.190	3.110	3.544	4.759	3.073	3.840
$\varepsilon_{\parallel, GaN}(\%)$	0	-2.4	11.2	+49	-3.6	+20.5
$\alpha(10^{-6}K^{-1})$	5.0	5.3	5.7	6.7	4.3	2.6

2.2.1 The debate on dislocations

Hall mobility measurements performed by Ng et al. [8] on n-type GaN samples with varying free electron concentration in the range of $10^{16} - 10^{20} \text{ cm}^{-3}$ indicated that electron scattering with the negatively charged edge dislocations are responsible for limiting the mobility. See fig. 2.2. It is discussed in detail in the next section. Look et al. [9] developed a theoretical model for charged dislocation scattering and demonstrated a very good fitting with experimental $n(T)$ and $\mu(T)$ over a wide range of temperature for samples with different dislocation densities (10^8 and 10^{10} cm^{-2}). Direct observation of negatively charged dislocations was made by D. Cherns et al. [10] using electron holography technique, where the phase map showed the potential of the dislocation varying by 4 eV from the surrounding regions (see fig. 2.3). Further, DFT calculations by Elsner et al. [11] showed that not only edge threading dislocations but also screw threading dislocations are electrically inactive with no deep gap states in wurtzite GaN. However, full-core screw dislocations could have deep gap states due to large bond distortions. The core structures assumed in this theoretical calculations were observed by Xin et al. using atomic resolution Z-contrast imaging [12], where pure edge and mixed dislocations in GaN were found to exhibit an eight-fold ring core structure (see fig. 2.4). The core of only the pure edge dislocations was found lying along a column of alternating Ga and N-atoms (as $[10\bar{1}0]$ surface dimmers). It is further pointed out that screw dislocation was also observed as a full core structure (see fig. 2.5) apart from an open core structure. Contrasting to all these studies, using ballistic electron emission microscopy, Im et al. suggested that there is no fixed negative charge associated with the threading dislocations, however, but evidently showed positively charged surface at TDs [13].

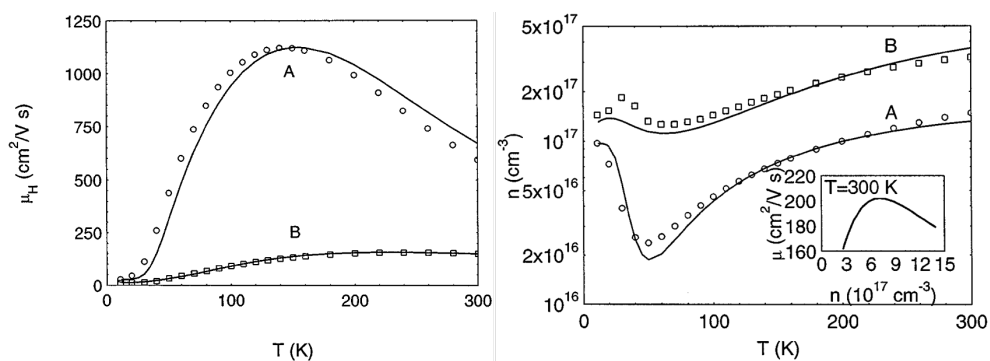


FIGURE 2.2: (a) Hall mobility vs temperature and (b) Hall concentration vs temperature for GaN samples A and B by Look et al. [9]. The solid lines are theoretical fits to experimental data represented in scattered dots. Sample A and B consist of dislocation density 10^8 and 10^{10} cm^{-2} respectively.

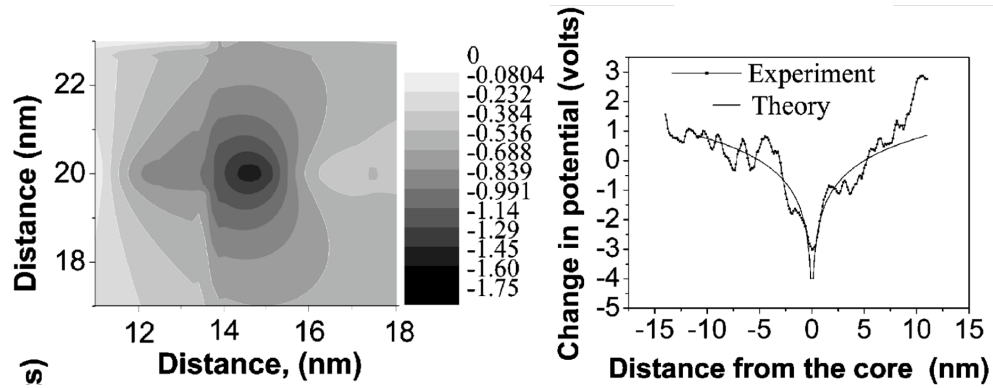


FIGURE 2.3: Electron holography phase map around the dislocation core (b) the line scan across the dislocation compared with the theoretical physical model of charged dislocation. The phase is plotted as an equivalent change in inner potential (solid line). [10]

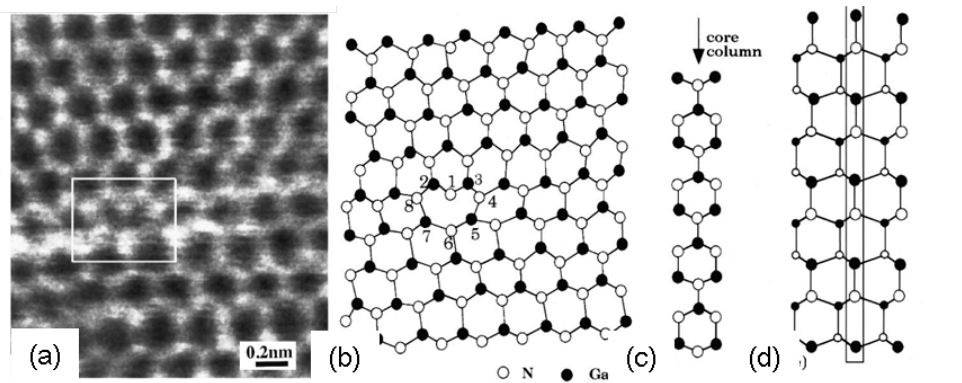


FIGURE 2.4: (a) High-resolution Z-contrast image of a threading dislocation with edge character looking down (0001). The bright dots are atomic columns of alternating Ga and N atoms. The dislocation core is shown in the boxed region. (b) Sketch of the core structure determined from the experimental data. One double Ga-N layer is projected onto the c plane. Core columns are indicated by numbers 1 to 8. (c) Side view of the core structure of a pure edge dislocation projected onto the {10 $\bar{1}$ 0} plane showing similarity to one dimer row in the {10 $\bar{1}$ 0} surface in (d). Smaller symbols denoting the atoms below the surface. [12]

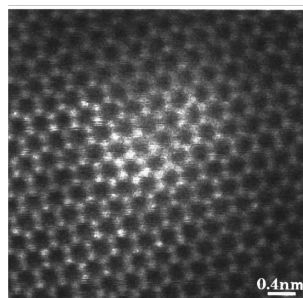


FIGURE 2.5: High resolution Z-contrast image of an end-on pure screw dislocation showing a full core. [12]

2.2.2 Determination of dislocations

As from the introduction of dislocations in the previous section, one must have already noticed that high resolution TEM, Z-contrast imaging microscopes are very powerful techniques to observe dislocations and core-structures but they are quite expensive and involve sample destruction. In the same family of investigation tools appears the scanning tunneling microscope. It is capable of imaging the surface atomic structure and has been successfully applied in GaN to observe dislocations [14] and to some extent can identify dislocation type. However, it is limited by small scan window available (few hundred nanometers), inaccessible below surface regions and requires very smooth and clean surface, which itself is a major issue in nitrides. In specific cases such as smooth MOCVD grown GaN (0001) surfaces consisting of step terraces (~ 0.2 nm) [15], by observing the interaction of dislocations with these terraces in the AFM topography image, identification of dislocations can be performed. As shown in fig. 2.6 [16], if the terrace terminates at the dislocation, it indicates the presence of screw-component, which has a Burger's vector along [0001] and if terrace doesn't interact with the dislocation, it would be a pure-edge type dislocation with Burger's vector along $[11\bar{2}0]$. However, with this method one cannot distinguish mixed and screw-type dislocations and is only applicable to GaN (0001) surface. This concept is hard to transfer to other nitride systems such as AlGa_N, InGa_N and AlIn_N, as they are already known for their 3D growth mechanism and rough surfaces. Terraces/steps are almost not seen in such ternary and quaternary alloys. A similar way for identification is chemical etching process where different dislocations show different resistance to etching. As shown in literature [17],[18], pure screw dislocations show the highest etching rate, followed by mixed-type dislocation and pure-edge type dislocations show the least affected. In fig. 2.7, post-etching GaN surface is shown. Apart from all the destructive methods explained above, using ECCI one may identify individually pure-edge, pure-screw and mixed-type dislocations [19].

2.2.3 Dislocations and current transport

A general accepted view of threading dislocations in GaN is that when charged, they act as Coulomb scattering centers. This scattering mechanism prevails when the doping level becomes equivalent to the volume concentration of traps introduced by dislocations. If the dislocations have acceptor centers along the dislocation line, they would capture electrons from the conduction band in an n-type semiconductor. The same is true for holes in p-type semiconductors. For example, for an edge dislocation density of 10^{10} cm^{-2} , one expects $2 \cdot 10^{17} \text{ cm}^{-3}$ of dangling bonds along the dislocation lines. The dislocation lines become negatively charged and a space charge is formed around

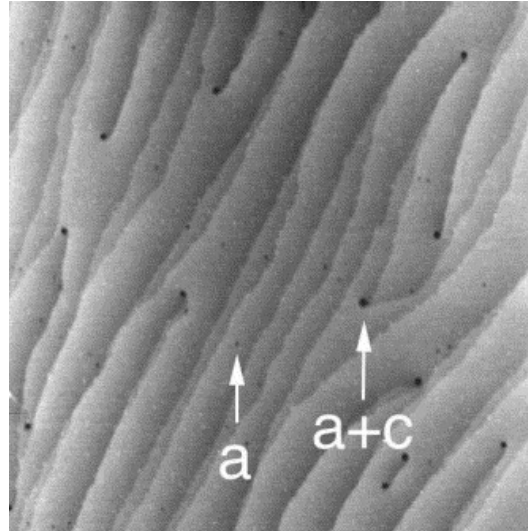


FIGURE 2.6: GaN (0001) surface showing terraces and dislocations. Terrace steps terminate at dislocations with screw component and have no interaction with pure-edge dislocations.[16]

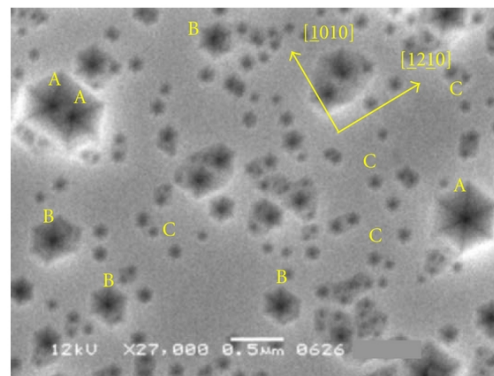


FIGURE 2.7: Etch pattern of HVPE GaN epilayer after 2-min E-etching at 540°C . The A pits are ascribed to the screw dislocations, the middle-size B pits to the mixed and the smallest C pits to the edge dislocations. [18]

it which scatters electrons traveling across the dislocations, thus reducing the mobility. For electron concentration below $10^{17} - 10^{18}\text{cm}^{-3}$ dislocation scattering dominates and, thus, mobility μ increases with concentration. For higher electron concentration, dislocation scattering is screened and ionized impurity scattering dominates, thus μ decreases.

The electron mobility due to such free carrier-charged dislocation scattering is given by the expression [20]

$$\mu = \frac{30\sqrt{2\pi\varepsilon^2 d^2 (KT)^{3/2}}}{N_{disl} e^3 f^2 \lambda_d \sqrt{m}} \quad (2.1)$$

where d is the distance between acceptor centers (i.e. dangling bonds) along the dislocation line,

f is the occupation rate of the acceptor centers,

N_{disl} is the density of dislocations,

and λ_d is the Debye screening length given as

$$\lambda = \left(\frac{\varepsilon kT}{e^2 n} \right)^{\frac{1}{2}} \quad (2.2)$$

where n is the net carrier concentration.

As shown in fig.2.8 (Ng et al.), the electron mobility is limited by scattering from dislocations, causing a monotonic increase in mobility with net carrier concentration (dashed line). Exceeded a certain free carrier concentration, the transport is dominated by the ionized impurity scattering. In fig. 2.8 this is shown as solid points falling on the solid line. One may also notice that there is trade-off between high electron concentration and mobility. The temperature dependence of the dislocation scattering limited mobility is reported in fig. 2.9, which shows a good fit between the experimental data (Ng et al.) and equation 2.1.

It is very interesting to note from fig. 2.8 that if the free electron concentration in GaN can be enhanced without using any dopant, by extrapolation one should achieve a very high mobility. This becomes the fundamental base of nitride based HEMT structures (AlGaN/GaN or AlInN/GaN) where high concentration of free carrier (2DEG) due to strong polarization fields is already present along with very high mobility in GaN.

The complete view of a threading dislocation doesn't end here. They are often found to be associated with V-shaped defects and have been consistently observed over years. There is a general consensus that this transformation is strongly dependent on the growth dynamics. They propagate to the surface surpassing a number of epilayers such as in MQW structures. Though there are physical models to explain how they are formed, it has not yet been understood how their growth can be controlled. However, there is still a debate if really they are detrimental to the devices or act as self-neutralizing as suggested by Hangleiter et al.

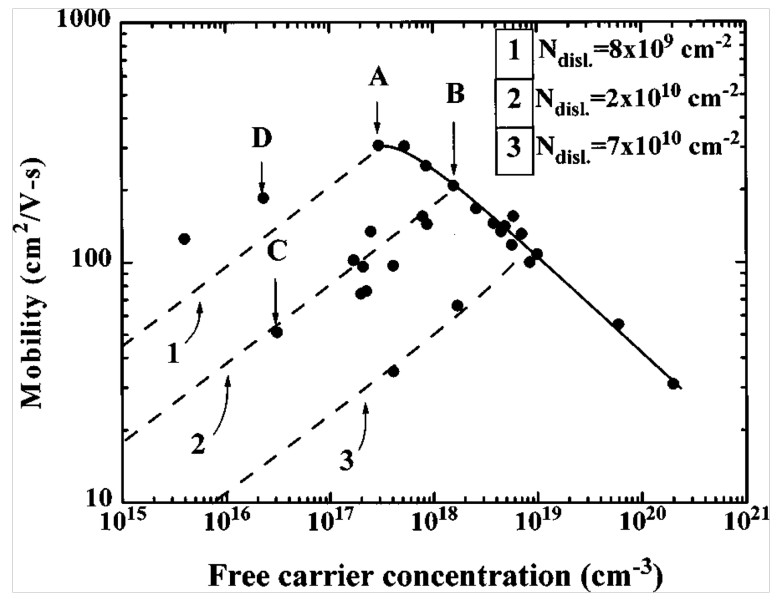


FIGURE 2.8: Electron mobility vs net carrier concentration of n-GaN films. The curves in the low carrier concentration regions are theoretical curves fitted to Eq. 2.1 with the indicated dislocation densities. [8]

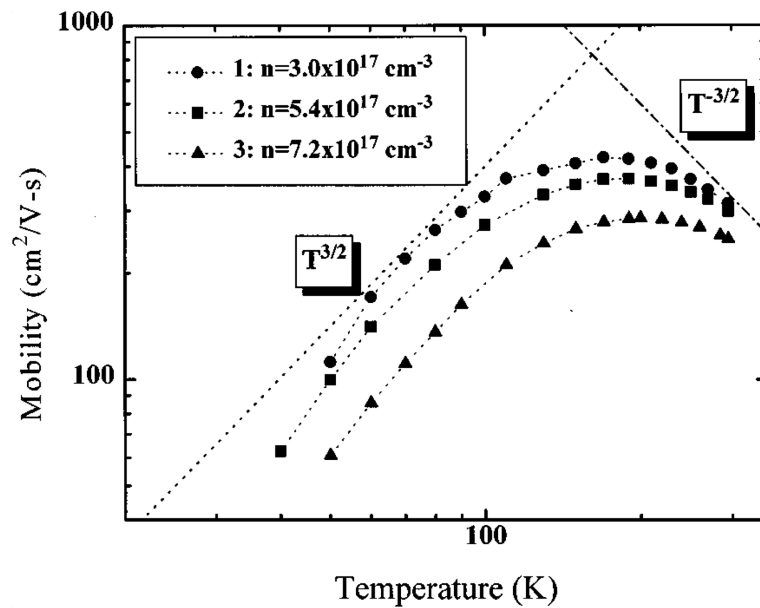


FIGURE 2.9: Temperature dependence of electron mobility of Si-doped GaN films where impurity scattering is the dominant scattering mechanism. [8]

2.3 V-shape defects

V-shaped structures are of great interest, and very often are present at nitride surfaces. SEM and TEM images of such V-defects have shown that these have a hexagonal inverted pyramidal structure. Further analysis has associated these V-shaped structures to threading dislocations as they are formed at the opening of the threading dislocations. Hence, the term **V-defects**, is coined-off from here. There are some other characteristic defects such as nanotubes and pinholes that are found in GaN and related epitaxial layers. They are extended always along the c-axis growth direction, also open up at the surface with a characteristic V shape and when observed in cross-sectional view, their V arms form a 60° angle. They occur in density of $10^5 - 10^7 \text{cm}^{-2}$ and their radii often is accounted in broad range, typically $2 - 40 \text{ nm}$ for nanotubes and few hundreds nanometers for pinholes in GaN. Contrary to nanotubes, pinholes do not have a substantial length with a constant diameter. However, both nanotubes and pinhole in-plane view appear as perfect or slightly elongated hexagonal shape. Depending on the polarity, the pinhole density varies, $10^6 - 10^7 \text{cm}^{-2}$ for Ga-polar and 2 orders of magnitude smaller for N-polar. It is important to mention that in N-polar they are also associated with inversion domains.

It is known that the growth on $\{10\bar{1}1\}$ planes is slow compared to $\{10\bar{1}1\}$ and $\{1010\}$ planes., which is true for both the polarities. This could explain the occurrence of large size pinholes or V-shape defects. In most cases, however, once a pinhole is formed it extends to the surface along V arms.

Hence, from topography, it would not be easy to distinguish pinhole from nanotube.

There are some examples of nanotubes and pinholes interacting with dislocations such as nanotubes with dislocation half-loops and very often pinholes with dislocations. However, there is a general consensus that there is no correlation between the dislocations and nucleation of nanotubes/pinholes except that dislocations get attracted towards nanotubes and pinholes to reduce their total line energy.

Understanding the micro-structural characteristics of V-defects and its origin is of fundamental importance for improving the device performance. As a matter of fact, V-defects in InGaN and InGaN/GaN multi quantum wells (MQWs) are found to be critical to optical properties and optical properties [21] [22] [23] and recent reports [24] [25] [26] on AlInN and InGaN proves V-defects to be the cause of high leakage current. One of the objectives of this thesis is to find why such high leakage is associated with V-defects. Density and size of V-defects may vary from one structure to another, hence it is necessary to understand growth dynamics, origin and equilibrium dimensions of V-defect structure.

The following section focuses on the current understanding of the formation of V-defects as proposed by Frank's theory [27].

Linear elasticity theory is implemented to estimate the formation energy of V-shape pit. For simplicity of the model, we consider here the crystal constituting of a single screw dislocation (with Burger's vector b along $[0001]$) that thread to the surface. Here topology of the screw dislocation is assumed as a hollow core cylindrical structure because it is often observed with an open core structure in GaN [28] as shown in figure 2.10. It is also referred to as nanpipes. If the internal surface energy of this dislocation is γ_0 , then its Frank's radius r is given by

$$r = \frac{\mu b^2}{8\pi^2 \gamma_0} \quad (2.3)$$

where μ is the shear modulus.

In the present case γ_0 is the surface energy of the internal surface $(10\bar{1}0)$. All the dimensions are presented in terms of r . V-defects are usually observed with hexagonal inverted pyramidal structure. For simplification of the calculation, this can be replaced with a cone of radius 'a' and height 'h' where they are related by the expression

$$h = \sqrt{\frac{8}{3}} a \quad (2.4)$$

The pit formation energy of the V-pits can be calculated from the following terms: (1) The change in surface energy resulting from replacement of a hexagonal (0001) surface with the six $(10\bar{1}1)$ facets of the inverted pyramid, given by $S\gamma - \gamma_0 r^2 x^2$ where

$$S = \left(\frac{3\sqrt{3}}{2} \right) \left(\frac{\gamma(10\bar{1}0)}{\alpha\gamma_0} - \frac{\gamma(0001)}{\gamma_0} \right) \quad (2.5)$$

and α is the scalar product of the unit vectors normal to $(10\bar{1}0)$ and (0001) planes (2) Reduction in strain energy where strain energy density over a cone is given as

$$E(\rho) = \frac{\mu b^2}{8\pi^2 \rho^2} \quad (2.6)$$

3) Elimination of the dislocation core energy λx . Thus, formation energy E_{form} of a V-pit is given by

$$E_{form} = S\gamma_0 r^2 x^2 - 2\pi\sqrt{\frac{8}{3}}\left(\frac{x}{x-1}\right)(x \ln x - x + 1)\gamma_0 r^2 - \lambda x \gamma_0 r^2 \quad (2.7)$$

The factor x defines the size of the V-pit and it depends on the energy associated with the dislocation. This value can be determined by minimizing E_{form} as given in equation above.

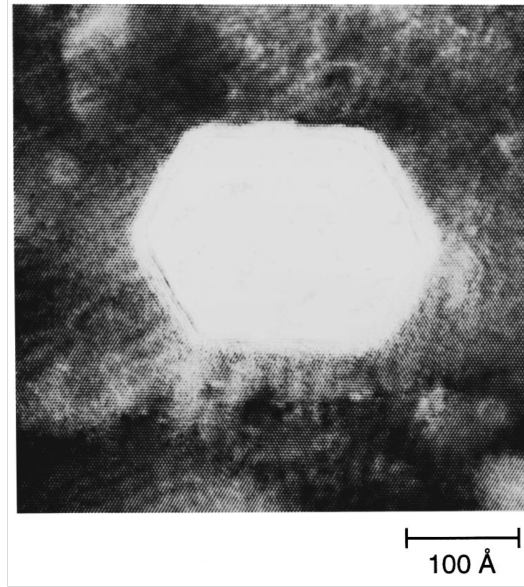


FIGURE 2.10: Atomic resolution TEM image of a screw dislocation open core obtained with the $[0001]$ zone axis. The internal surfaces of the open core are formed by six close-packed $\{1\bar{1}00\}$ prism planes (lattice spacing of 2.76\AA). COURTESY: Qian et al. [3]

During the growth, pinholes may occur at many possible locations, such as sites where growth islands coalesce, a dislocation intersects the growth surface or where the impurity clusters. And this is all due to formation of initial $\{10\bar{1}1\}$ surfaces that have a slow growth rate. It is observed that with introduction of impurities or dopants such as O, Si, Mg etc., an enhancement in the density and size of the pinholes and nanotubes is observed, even in the absence of any affect on the strain of the layer. In case of InGaN QWs or highly strained InGaN/AlGaIn QWs, their density is dramatically increased, which suggests that indium incorporation and local strain could also facilitate their formation. These observations suggest that it is not strain but impurity clustering, which may locally impede growth causing small indentations that could become the nucleus of a pinhole. These pinholes may eventually form nanotube if their facets $\{10\bar{1}1\}$ evolve

into $\{1010\}$ facets parallel to the growth direction. This occurs when impurities are absent, resulting in rapid growth rate on $\{1010\}$ planes. However, presence of impurities hinders the growth of $\{1010\}$ planes and opens up a way for $\{10\bar{1}1\}$ facets resulting in V-shaped defects.

Though, most of the open-core or nanopipe dimensions and dislocations structures can be reasonably explained by the Frank's equation (in terms of Frank-radius and the Burger's vector length), while others not. One could attribute growth kinetics for such quantitative discrepancies, however, there still a need for a deeper investigation. Since these open cores would be detrimental to the devices, it is very important to determine the processing conditions in which they become unstable and vanish.

Lifetime of an optical device is critically determined not only by the dislocations but also by other structural defects such as misfit dislocations, cracks, domain boundaries, stacking faults and point defects, which may act as traps and effective recombination centers.

2.4 Misfit Dislocations

Dislocations are formed on planes containing the minimum lattice translations. These planes are the preferred slip planes. A slip plane (same as glide plane) contains both the Burger's vector and the line direction of the generated dislocations. It is defined by two terms: the plane and the direction of the slip. In hexagonal structures, (0001) or basal plane is the only plane with highest lattice site density. This plane contains minimum lattice translations, and thus are the preferred slip planes. So, this slip system is conventionally written as $\{0001\} \langle 11\bar{2}0 \rangle$ type and the minimum lattice translations are given as $1/3[11\bar{2}0]$, $1/3[1\bar{2}10]$ and $1/3[\bar{2}110]$.

The generation of the misfit dislocation can be calculated from the net driving force required for the formation and glide of misfit dislocations for each slip system. Based on the classic Matthews-Blakeslee model, a misfit dislocation can be described by two kinds of forces acting on it. The first force F_a is the force acting on the slip plane along the slip direction. This force is a result of the shear stress present due to lattice mismatch. F_a is given by

$$F_a = 2Gb\epsilon \frac{1+v}{1-v} \cos\lambda \quad (2.8)$$

where G is the shear modulus of the film, b is the Burger's vector of the misfit dislocation, h is the film thickness, ν is the Poisson ratio, λ is the angle between the Burger's vector and the vector in the interfacial plane, which is perpendicular to the dislocation line. E is the strain in the film given by

$$\varepsilon = \frac{a_f - a_s}{a_s} \quad (2.9)$$

where a_f and a_s are the lattice parameters of the film and substrate respectively. The second force F_l is due to the line tension, resisting formation of the dislocation. This force can be expressed as

$$F_l = Gb^2 \left(\frac{1 - \nu \cos^2 \alpha}{4\pi(1 - \nu)} \right) \left(\ln \left(\frac{h}{b} \right) + 1 \right) \quad (2.10)$$

where α is the angle between the misfit dislocation line and its Burger's vector. Apart from these two forces, dislocation motion is impeded by the Peierls forces, which result in a frictional force on the dislocation. This force F_p can be written as

$$F_p = 2Gbh \sec \phi \left(\frac{1 - \nu \cos^2 \alpha}{1 - \nu} \right) \omega \exp \left(\frac{-2\pi d(1 - \nu \cos^2 \alpha)\omega}{(1 - \nu)b} \right) \quad (2.11)$$

where ϕ is the angle between the film surface and the normal to the slip plane, d is the interplanar spacing corresponding to the slip plane. ω is a material constant given by

$$\omega = \left(\frac{4\pi^2 n k T}{5GV} \right) \quad (2.12)$$

where n is the number of atoms per unit cell, V is the volume of the unit cell and T is the growth temperature. This expression for the Peierl's force is based on the assumption that the dislocation motion is by slow mechanical glide under stress and not by diffusive glide. The Peierls force is then independent of dislocation velocity. The net driving force for dislocation glide is $F_{net} = F_a - F_l - F_p$. Misfit dislocations are formed when the lattice mismatch force exceeds the opposing forces. At the critical thickness, the three forces are in equilibrium and $F_{net} = 0$. For a film thickness greater than the critical thickness, $F_{net} > 0$ and misfit dislocations are generated.

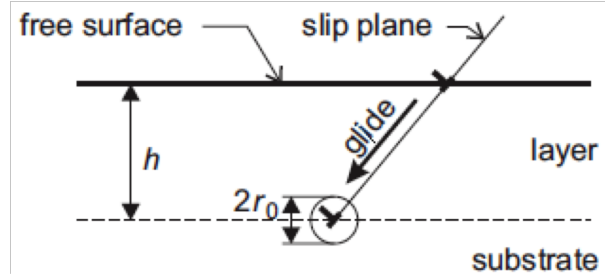


FIGURE 2.11: Schematic illustrating the glide of misfit dislocation (perpendicular to the plane) from a free surface. COURTESY: Holec et al. [29]

In the table below is shown the net force acting on the misfit dislocation in $\{0001\}$ for all possible slip systems in $In_{0.1}Ga_{0.9}N/GaN$ calculated by Srinivasan et al. [30]. There are only two active slip systems in InGaN: $11\bar{2}2 < 11\bar{2}3 >$ and $1\bar{1}01 < 11\bar{2}3 >$. Misfit dislocation glide on a non-basal slip plane is schematically shown in fig. 2.11.

TABLE 2.2: Slip systems and the corresponding forces acting on the misfit dislocations in InGaN. COURTESY: Srinivasan et al.

slip system	$\cos\lambda$	$F_a(nN)$	$F_l(nN)$	$F_p(nN)$	$F_{net}(nN)$
$\{0001\} < 11\bar{2}0 >$	0	0	24	-	
$\{1\bar{1}00\} < 11\bar{2}0 >$	0	0	11	53	-
$\{1\bar{1}00\} < 0001 >$	0	0	68	10	-
$\{11\bar{2}0\} < 0001 >$	0	0	68	349	-
$\{1\bar{1}01\} < 11\bar{2}0 >$	0	0	11	117	-
$\{1\bar{1}02\} < 11\bar{2}0 >$	0	0	11	465	-
$\{11\bar{2}2\} < 11\bar{2}3 >$	0.524	634	92	44	499
$\{1\bar{1}01\} < 11\bar{2}3 >$	0.454	549	88	127	334
$\{1\bar{1}02\} < 1\bar{1}01 >$	0.730	1099	137	1947	-

Since misfit dislocation is a form of plastic deformation, critical thickness of a material can also be related to the onset of MD formation, other than strain. As InGaN and InN grown over GaN is compressively strained, cracking is not possible and their critical thickness only points towards the MD formation. Though other alloys such as AlGaN and in some cases GaN bulk are tensile strained, their critical thickness would refer to the crack formation. Since misfit dislocations have already been observed along with cracks, they are found to be inter-related and this will be discussed in the next section.

2.5 Basal plan stacking faults (BPSF)

The wurtzite structure is characterized by the stacking sequence ...ABAB- ABAB... along the (0001) direction perpendicular to the basal plane where each letter stands for

an ordered pair of cation and anion layers separated by distance uc , which is defined in terms of lattice constant c along (0001) and internal parameter $u \approx 0.375$. In case of zincblende the stacking sequence would be $\acute{E}ABCABC$. A basal-plane stacking fault is simply defined as a disruption in this stacking sequence.

In the wurtzite structure, three types of faults are well known: I_1 , I_2 , and extrinsic. And a new kind of intrinsic stacking faults reported in Ref. [31].

I_1 : The formation of this kind of intrinsic stacking fault requires only one violation of the stacking rule and has the lowest formation energy with respect to other stacking faults. This fault can occur either on the pair A or B, such that stacking sequence would change to ABABACACAC or ABABCBCBCB respectively. This stacking sequence is depicted in fig. 2.12(a). Since this has the lowest formation energy, it is the most encountered SF in GaN and AlN and is associated with partial dislocations. They are formed due to growth related phenomena.

I_2 : intrinsic stacking faults (also called I_2). Its occurrence involves two violations of the stacking rule, and it has the next lowest formation energy. The stacking sequence would appear as ABABCACACA. The stacking sequence depicted in Fig. 2.12(b). They are associated with Shockley partial dislocations suggesting their formation via slip (strain relaxation).

E: These are extrinsic stacking faults. The faults have an additional C pair inserted in the midst of the normal stacking sequence changing to sequence to ABCAB. See fig. 2.12(c)

The fourth kind is another kind of intrinsic stacking fault (type III)[31]. Here, C occupies one of the A or B layers, changing the stacking sequence to AaBbAaCcAaBb. See fig. 2.12(d)

Stacking fault energy is defined as the difference in energy between faulted and unfaulted structures. This energy can be expressed in terms of per unit area in the basal plane or the area of a primitive unit cell in which case it is referred to as reduced stacking fault energy. Reduced stacking fault energies for I_1 , I_2 and E as estimated from DFT calculations by A.F.Wright are summarized in table 2.3. It shows that the stacking fault energy is lower in GaN and highest in AlN. In case of full relaxation of the layer separations (i.e. between A and B) and cation-anion separations within each layer, stacking fault energies reduce by a maximum of 5%.

across the stacking fault is limited by the tunneling through the depletion region and quantum well region and charge scattering. As a result, conductivity and mobility across the stacking fault is observed to be lower in comparison to that of the basal plane [35].

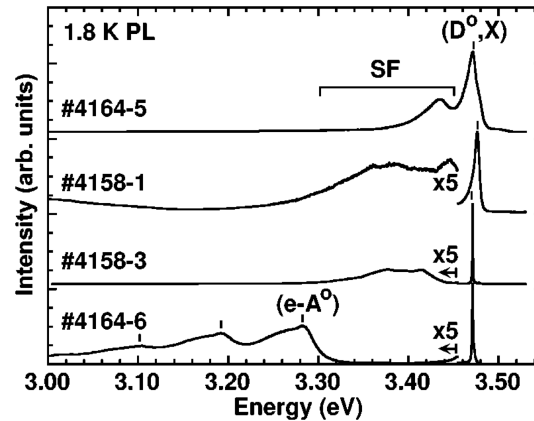


FIGURE 2.13: Schematic illustrating the glide of misfit dislocation (perpendicular to the plane) from a free surface. COURTESY: Bai et al.[33]

J. Bai et al. showed that PL peak at low temperature in the range of 3.30-3.45 eV are related to basal plane stacking faults (fig. 2.13) by showing an increase in the SF-related PL intensity with the BPSF density. They can be bounded with Shockley partial dislocations with Burger's vectors of $1/3 \langle 10\bar{1}0 \rangle$. These stacking faults act as quantum wells where electrons are localized in the thin 3C-GaN quantum wells in the faulted region and holes that are either in the same regions or in the 2H-GaN barriers.

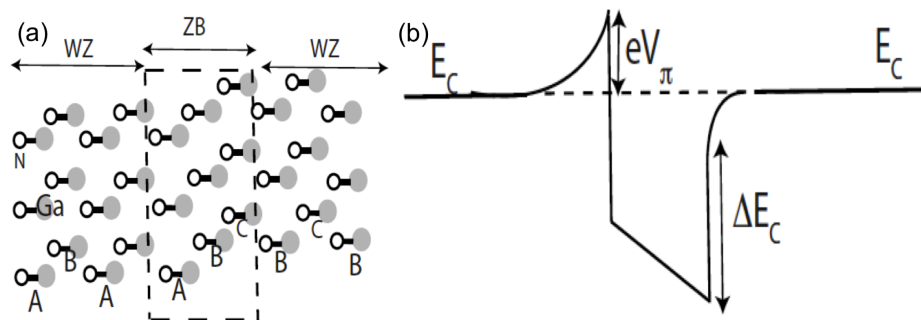


FIGURE 2.14: (a) structure of stacking fault (type I_1) and (b) the corresponding conduction band model.

2.6 Cracks

Additionally to threading dislocations, when the film thickness surpasses a threshold “critical thickness”, GaN films starts to crack mostly during the post-growth cooling process. This is primarily due to the tensile stress arising from the thermal expansion

coefficient mismatch, which is further facilitated from the tensile stress developed from island coalescence and lateral grain growth. It significantly reduces the performance of GaN-based devices due to their association with poor crystal quality and they also act as carrier-scattering centers. Since the crack density is highly dependent on the growth conditions, it is possible to improve the average size of the crack-free surface areas by manipulating the growth conditions and post-growth heat treatment.

In AlGaN/GaN heterostructures, the high stress generated in AlGaN can promote catastrophic failure in AlGaN/GaN based UV LEDs via crack-generation. Depending on the Al% (or the stress), cracks are found to lie on $\{11\bar{2}0\}$ planes for low Al content and $\{1\bar{1}00\}$ for higher Al. It is not necessary that cracks would always exhibit facet openings at the surface, but could also be observed with overgrowth (fig. 2.15a) or terraced atomic steps (fig. 2.15b). Relaxation mechanism is also associated with the formation of misfit dislocations. In general, equilibrium critical thickness to generate misfit dislocations is smaller than of the crack. In the absence of active slip system for planar (0001) nitride films, formation of interfacial misfit dislocations is less feasible. However, due to the high shear stress concentration surrounding the crack tips at the AlGaN/GaN interface, misfit dislocation nucleation and their subsequent glide on the interfacial plane (0001) could occur or in short, crack formation can activate the slip systems for misfit dislocations. This signifies that strain relaxation in coherently strained films could occur via both crack and misfit dislocation formation.

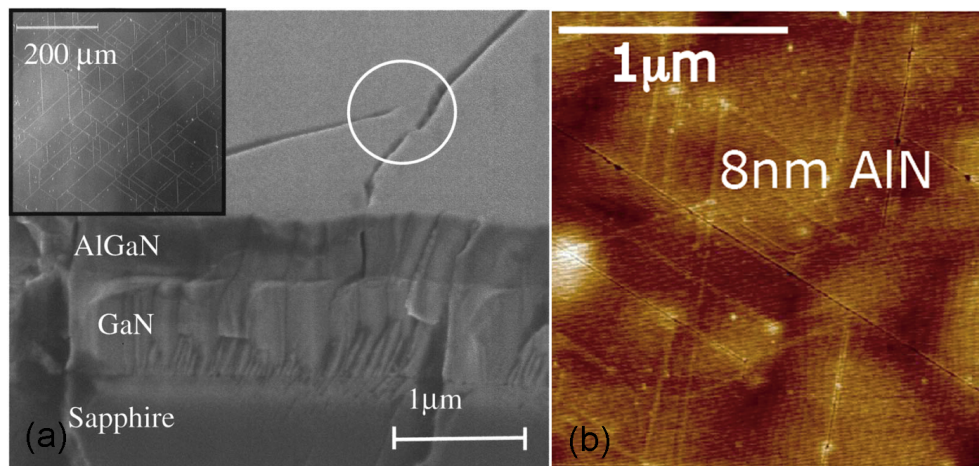


FIGURE 2.15: (a) SEM image of a $0.5\mu\text{mAl}_{0.37}\text{Ga}_{0.63}\text{N}/\text{GaN}$ heterostructure on sapphire. Overgrowth of cracks (circled). Dark field optical plan view image of the crack network in an $\text{Al}_{0.17}\text{Ga}_{0.83}\text{N}$ film (inset). [36] (b) AFM image of 8 nm thick AlN grown on GaN substrate [37]

There has been a lot body of research in optimizing the growth conditions of the buffer layer as well as the multi-structure design, which has significantly reduced the cracking

problems in GaN. This includes various methods such as multi-step AlGa_N graded structure [38], AlGa_N/GaN superlattice [39], insertion of a low-temperature AlN (LT-AlN) interlayer into the bulk high growth temperature GaN [40], *HT – AlN/LT – AlN/HT – AlN/Al_xGa_{1-x}N* buffer system [41].

Graded AlGa_N intermediate layers between the AlN NL and the GaN introduce compressive stress during growth in order to compensate for the tensile stress that is generated primarily during the cool down from the growth temperature. The growth of a successive *Al_xGa_{1-x}N* layer introduces compressive stress when $x < y$ due to the negative lattice mismatch between GaN and AlN.

LT-AlN interlayer can lead to a lower threading dislocation density, improvement of the crystalline quality and the reduction of tensile stress and cracking that is generated during the high-temperature GaN growth or cooling. AlN epitaxial layers are widely applied as nucleation layers (NLs) for GaN growth on silicon and serve not only as wetting layers for GaN but also as barrier layers to prevent Ga meltback etching.

In this chapter, we deeply discussed various kinds of defects including threading dislocations, in-plane interfacial misfit dislocations, cracks and stacking faults that occur often in III-nitrides, can act as traps and recombination centers. Though a lot of research has already been done in understanding their properties and their effect on optoelectronic devices, but still there is a lack of general consensus in many cases due to contradicting observations. This opens up the need for further investigation.

Bibliography

- [1] S. D. Lester, F. A. Ponce, M. G. Craford, and D. A. Steigerwald. *Appl. Phys. Lett.*, 66:1249, 1995.
- [2] R. C. Powell, N.-E. Lee, Y.-W. Kim, and J. E. Greene. *J. Appl. Phys.*, 73:189, 1993.
- [3] W. Qian, M. Skowronski, M. D. Graef, K. Doverspike, L. B. Rowland, and D. K. Gaskill. *Appl. Phys. Lett.*, 66:1252, 1995.
- [4] H. Morkoc. *Mat. Sci. Eng.R*, 33:135–207, 2001.
- [5] K. Osamura, S. Naka, and Y. Murakami. *J. Appl. Phys.*, 46:3432, 1975.
- [6] H. Schulz and K. H. Thiemann. *Solid State Commun.*, 23:815, 1977.
- [7] O. Ambacher. *J. Phys. D: Appl. Phys.*, 31:2653–2710, 1998.
- [8] H. M. Ng, D. Doppalapudi, T. D. Moustakas, N. G. Weimann, and L. F. Eastman. *Appl. Phys. Lett.*, 73:821, 1998.
- [9] D. C. Look and J. R. Sizelove. *Phys. Rev. Lett.*, 82:1237, 1998.
- [10] D. Cherns and C. G. Jiao. *Phys. Rev. Lett.*, 87:205504, 2001.
- [11] J. Elsner, R. Jones, P. K. Sitch, V. D. Porezag, M. Elstner, Th. Frauenheim, M. I. Heggie, S. Oberg, and P. R. Briddon. *Phys. Rev. Lett.*, 79:3672, 1997.
- [12] Y. Xin, S. J. Pennycook, N. D. Browning, S. Sivananthan, F. Omne's, B. Beaumont, J. P. Faurie, and P. Gibart. *Appl. Phys. Lett.*, 72:2680, 1998.
- [13] H.-J. Im, Y. Ding, J. P. Pelz, B. Heying, and J. S. Speck. *Phys. Rev. Lett.*, 87:106802, 2001.
- [14] A. R. Smith, V. Ramachandran, R. M. Feenstra, D. W. Greve, M.-S. Shin, M. Skowronski, J. Neugebauer, and J. E. Northrup. *J. Vac. Sci. Technol. A*, 16:1641, 1998.

- [15] P. J. Hansen, Y. E. Strausser, , A. N. Erickson, E. J. Tarsa, P. Kozodoy, E. G. Brazel, J. P. Ibbetson, U. Mishra, V. Narayanamurti, S. P. DenBaars, and J. S. Speck. *Appl. Phys. Lett.*, 72:2247, 1998.
- [16] H.P.D. Schenk, P. Vennegues, O. Tottereau, T. Riemann, and J. Christen. *Journal of Crystal Growth*, 258:232, 2003.
- [17] L. Huang, F. Liu, J. Zhu, R. Kamaladasa, E. A. Preble, T. Paskova, K. Evans, L. Porter, Y. N. Picard, and R. F. Davis. *Journal of Crystal Growth*, 347:88–94, 2012.
- [18] V. Ivantsov and A. Volkova. A comparative study of dislocations in hvpe gan layers by high-resolution x-ray diffraction and selective wet etching. *ISRN Condensed Matter Physics*, 2012:184023, 2012.
- [19] G. Naresh-Kumar, B. Hourahine, P. R. Edwards, A. P. Day, A. Winkelmann, A. J. Wilkinson, P. J. Parbrook, G. England, and C. Trager-Cowan. *Phys. Rev. Lett.*, 108:135503, 2012.
- [20] B. Podor. *Phys. Status Solidi*, 16:K167, 1966.
- [21] S. Nakamura. *Science*, 281:956–961, 1998.
- [22] J. Bruckbauer, P. R. Edwards, T. Wang, and R. W. Martin. *Appl. Phys. Lett.*, 98:141908, 2011.
- [23] X. H. Wu, C. R. Elsass, A. Abare, M. Mack, S. Keller, P. M. Petroff, S. P. DenBaars, , J. S. Speck, and S. J. Rosner. *Appl. Phys. Lett.*, 76:692, 1998.
- [24] A. Minj, D. Cavalcoli, and A. Cavallini. *Appl. Phys. Lett.*, 97:132114, 2010.
- [25] J. Song, F. J. Xu, X. D. Yan, F. Lin, C. C. Huang, L. P. You, T. J. Yu, X. Q. Wang, B. Shen, K. Wei, and X. Y. Liu. *Appl. Phys. Lett.*, 97:232106, 2010.
- [26] X. A. Cao, J. M. Teetsov, M. P. D’Evelyn, D. W. Merfeld, and C. H. Yan. *Appl. Phys. Lett.*, 85:7, 2004.
- [27] F. C. Frank. *Acta Crystallogr.*, 4:497, 1951.
- [28] W. Qian, G. S. Rohrer, M. Skowronski, K. Doverspike, L. B. Rowland, and D. K. Gaskill. *Appl. Phys. Lett.*, 67:2284, 1995.
- [29] D. Holec, P.M.F.J. Costa, M. J. Kappers, and C.J. Humphreys. *Journal of Crystal Growth*, 303:314–317, 2007.
- [30] S. Srinivasan, L. Geng, F. A. Ponce, Y. Narukawa, and S. Tanaka. *phys. stat. sol. (c)*, 0:2440–2443, 2003.

- [31] C. Stampfl and C. G. Van de Walle. *Phys. Rev. B*, 57:R15052, 1998.
- [32] A. F. Wright. *J. Appl. Phys.*, 82:5259, 1997.
- [33] J. Bai, M. Dudley, B. Raghathamachar, P. Gouma, B. J. Skromme, and L. Chen. *Appl. Phys. Lett.*, 84:3289, 2004.
- [34] R. Liu, A. Bell, F. A. Ponce, C. Q. Chen, J. W. Yang, and M. A. Khan. *Appl. Phys. Lett.*, 86:021908, 2005.
- [35] Aniruddha Konar, Tian Fang, Nan Sun, and Debdeep Jena. *Appl. Phys. Lett.*, 98:022109, 2011.
- [36] S. J. Hearne, J. Han, S. R. Lee, J. A. Floro, D. M. Follstaedt, E. Chason, and I. S. T. Tsong. *Appl. Phys. Lett.*, 76:1534, 2000.
- [37] Yu Cao and Debdeep Jena. *Appl. Phys. Lett.*, 90:182112, 2007.
- [38] M-H. Kim, Y-G. Do, H. C. Kang, D. Y. Noh, and S-J. Park. *Appl. Phys. Lett.*, 79:2713, 2001.
- [39] S.A. Nikishin, N.N. Faleev, G. Antipov, S. Francoeur, L. Grave de Peralta, G.A. Seryogin, H. Temkin, T.I.Prokofyeva, M. Holtz, and S.N.G.Chu. *Appl. Phys. Lett.*, 75:2073, 1999.
- [40] H. Amano, M. Iwaya, T. Kashima, M. Katsuragawa, I. Akasaki, J. Han, S. Hearne, J. A. Floro, E. Chason, and J. Figiel. *Jpn. J. Appl. Phys.*, 37:L1540–L1542, 1998.
- [41] E. Arslan, M. K. Ozturk, A. Teke, S. Ozcelik, and E. Ozbay. *J. Phys. D: Appl. Phys.*, 41:155317, 2008.

Chapter 3

Experimental techniques

3.1 Atomic force microscopy

In 1986, Gerd Binnig and Heinrich Rohrer shared the Nobel Prize in Physics for the invention of Scanning Tunneling Microscope (STM) [1] to image individual surface atoms with a high resolution for the first time. This success of the STM then led to the invention of other scanning probe microscopes, where a sharp tip is mechanically scanned over a sample surface. The atomic force microscope (AFM) is one of the most successful among these to be used worldwide [1]. The emergence of AFM was to overcome the limitation present in STM as it doesn't have the potential to image insulating materials. A measurable quantity of force between the molecules of a sharp tip and the surface, would allow imaging insulating surfaces that was not possible with STM due to very low measurable tunneling current. Owing to a high "inter-atomic" spring constant $\sim 10 \text{ N/m}$, this can be achieved. The inter-atomic spring could be calculated from the relation $k = \omega^2 m$, where vibration frequencies ω is typically $> 10^{13} \text{ Hz}$ for atoms bounded in a molecule or in a crystalline solid and the mass of the atoms $\sim 10^{-25} \text{ kg}$. By designing cantilevers to mount these sharp tips with a spring constant much lower than the equivalent spring between atoms, it would make it possible to sense angstrom-size displacements of such soft cantilevers and image atomic scale topography without pushing the atoms out of their atomic sites. With time and as the need to study material and electronic properties locally has increased, this methodology was further upgraded into other modes such non-contact and tapping mode. The phase images associated with these modes proved to be very efficient to differentiate chemical compositions, and stiffness in the field of organics, biology and microelectronics. The ability to control the motion of sharp tip in close proximity to the surface led to the emergence of new modes such as KPFM, SCM that proved to be very promising in the field of semiconductors

to study material defects, for diagnostic purposes in microelectronic circuits and to characterize nanostructures.

3.1.1 AFM Setup

The principal of operation of an AFM is shown schematically in fig. 3.1. Principally, AFM consists of six essential components:

1. **Piezoelectric actuator (X,Y)** to scan the surface (along x and y-direction) in a raster pattern
2. **Piezoelectric tube (Z)** to map vertical movements along z-direction
3. **Optical detection system**
4. **Laser diode** to provide measureable intensity as the input signal
5. **Photodiodes** to track the position of the reflected laser spot
6. **Sharp tip mounted on a cantilever with reflective backside** for laser spot
7. **Feedback system** to control the movement of the Piezo
8. **Display** to convert measured data into an image

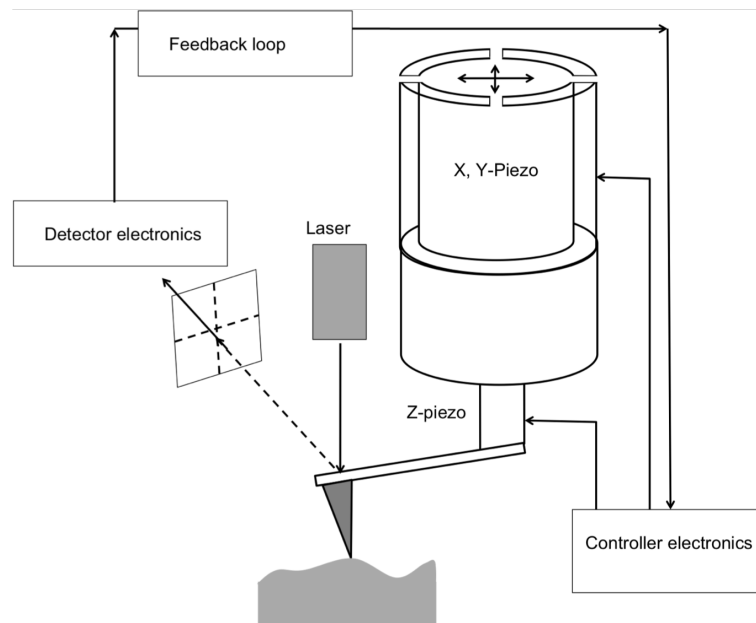


FIGURE 3.1: Schematic diagram of the experimental setup of AFM.

3.1.1.1 How does AFM work?

The AFM tip is first brought in close proximity to the sample surface such that there is a measurable force of interaction that may be attractive or repulsive between them starts to appear. This force of interaction is tip-sample distance dependent (as shown in fig. 3.2) and can be easily quantified. Depending on the requirement, one may operate AFM at a fixed interaction force, which is commonly known as the SET POINT. The definition of set point would vary as the mode of operation of AFM varies. There are three modes in AFM:

1. Contact AFM
2. Non-contact AFM
3. Intermittent, tapping or semi-contact AFM

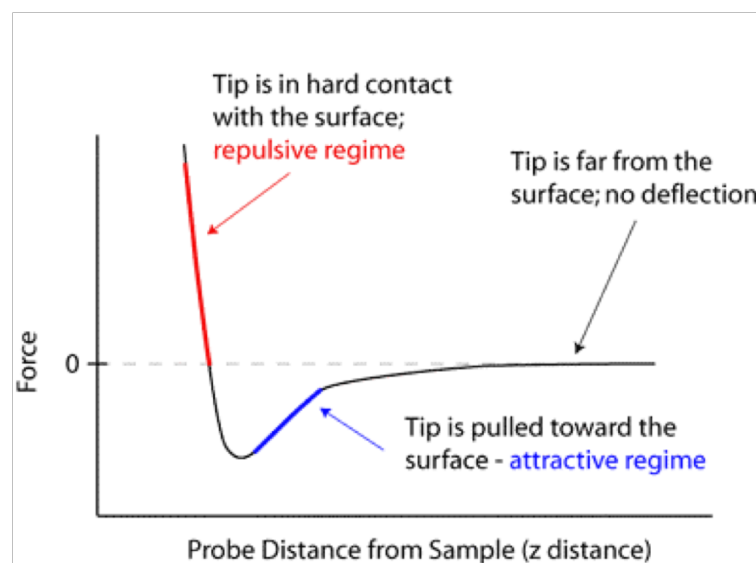


FIGURE 3.2: Force-distance curve showing the regions of operation of contact, semi-contact and non-contact AFM.

Under the operating condition set by the user, the tip is scanned across the sample surface under the action of a XY-piezoelectric actuator, either by moving the sample relative to the tip or vice versa. A laser beam aimed at the reflective backside of the cantilever reflects off to a split photodiode, which detects any kind of variation in the force of interaction from the defined set point during the scan. A feedback loop, shown in fig. 3.1, maintains constant tip-sample interaction at the fixed set point by moving the piezoactuator in the z direction. Depending on the kind of detection signal, AFM is classified to work in different modes.

3.1.2 Contact mode

The mode of detection of tip-surface interaction is the variation in the cantilever deflection that happens while scanning a surface with non-zero roughness. Cantilever deflection can be measured by an optical detection system. Feedback loop maintains a constant tip-sample interaction by adjusting the Z-piezoactuator.

3.1.2.1 Dynamics of the tip in contact mode

At any given location on the surface, tip-sample interaction can be obtained by observing the dynamics of the tip as it approaches or retracts from the surface i.e. as a function of retraction/contraction of the Z-piezoactuator. Due to the forces acting on the tip (mounted on a flexible cantilever), the tip-sample distance is not same as Z-piezoactuator movement. The relationship of tip-surface interaction force with distance is called force spectroscopy. It is typically a force vs. distance curve as shown in fig. 3.3, which is a plot of the cantilever deflection versus position of the Z-piezoactuator that changes the distance between the sample and the cantilever. In general, force spectroscopy is dependent on material properties and often is used to measure

1. the vertical force applied by the AFM tip on the surface [2]
2. the adhesion of surface contaminants [3]
3. the local elastic properties [4]



FIGURE 3.3: Force spectroscopy during approach (blue) and retraction (red).

The force-distance curve is obtained by capturing the deflection signal against the piezo movement in both the directions towards the surface (approach) and away from the

surface (retraction). Let us consider the first case, where the tip is approaching the surface. As depicted in fig. 3.3, when the tip is at position 1 there is negligible force between the tip and surface, hence, no cantilever deflection is observed. As it moves further (position 2), tip comes close enough to the sample surface to experience the attractive van der Waals force, cantilever starts to bend downwards gradually. However, after reaching position 3 a further “approach” causes a sudden jump in the deflection to position 4. This indicates the absence of any stable states between position 3 and position 4. This is explained in fig. 3.4. As already written, the net force on tip is zero (condition of equilibrium). The attractive and repulsive forces that can be computed from Lennard-Jones curve acting on it are balanced by the cantilever’s spring force $k \cdot x$.

$$F_{tip-surface} = k \cdot x \quad (3.1)$$

where x is the cantilever deflection.

All possible positions of the tip near the surface are solutions of equation 3.1 i.e. the possible values of x . As seen in fig. 3.4, at position 3, there are two roots that are both stable. Further “approach” causes suddenly a single root. As the scanner continues to extend, the cantilever deflects away from the surface and hence, bends upwards.

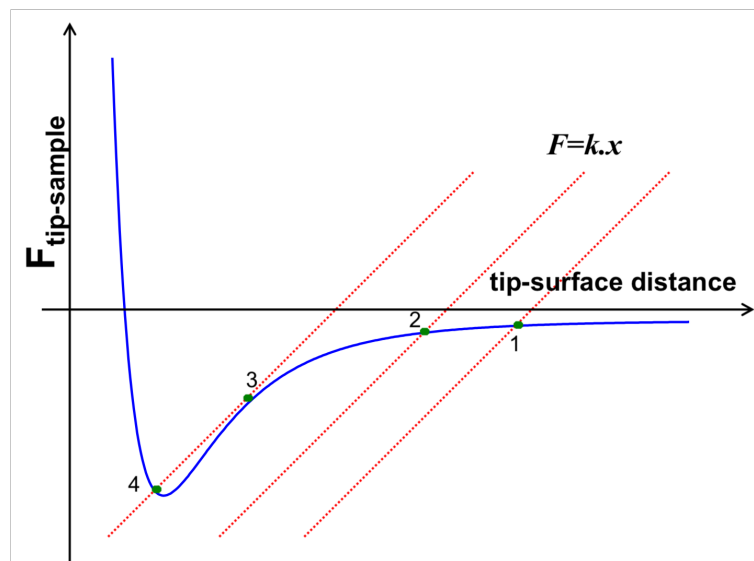


FIGURE 3.4: Solutions of tip-sample distance dependent force with cantilever spring force.

In the second case when the piezo is retracted, the cantilever deflection retraces the same curve, in the reverse direction. The retracting curve is usually different from the approach curve because of the formation of water meniscus between the tip and the surface. This water layer exerts an attractive capillary force on the tip and, as the piezo moves away from the surface, it holds the tip in contact with the surface, strongly

bending the cantilever towards the surface. When further pulled, at a certain point the piezo retraction is large enough to snap free the tip from the surface (transition from position 6 to position 7). As retraction continues, the cantilever goes through the regime of long-range attractive forces (position 8) and later becomes completely undeflected. The positions and amplitudes of the snaps depend upon the adhesion and thickness of the layers present on the surface. This could be very useful in the study of polymers, nanoparticles, biological samples and surface contaminants. In the linear region of the curves (position 5), the slope is related to the cantilever stiffness when the sample is infinitely hard. However, when the cantilever is stiffer than the sample surface, or nearly as stiff as the sample surface, then the slope of the curve would enable investigation of the elastic properties of the sample.

3.1.3 Semi contact mode

In this mode, the cantilever is not static but oscillating at its resonance frequency. An AC bias applied to the z-piezoactuator at an operating frequency, equal to the resonance frequency of the cantilever, acts as the oscillation driving force. In contrary to contact mode, the amplitude of the oscillation acts as the detection signal and the feedback loop maintains constant amplitude of the cantilever oscillation (constant amplitude). Due to the oscillation of the tip, its dynamics is more complex than that of in contact mode. The interactions between the tip and the sample can be categorized as (i) elastic interactions (ii) inelastic interactions with viscous damping (iii) inelastic interactions involving adhesion energy hysteresis.

3.1.3.1 Dynamics of the tip in semi-contact mode

Impact model Dynamics of the tip can be understood by two different approaches: forces acting on the tip in equilibrium and energy conservation. In both the cases, the cantilever is modeled by a spring and a mass as shown in fig. 3.5. The base of the cantilever is subjected to a sinusoidal motion given by $z(t)$. The air damping is proportional to the velocity of the mass with respect to an inertial frame. In most applications, the first-mode approximation for the cantilever vibration is adequate for explaining the experimentally observed characteristics. By assuming one-mode approximation, the dynamics of the cantilever-tip ensemble can be described by a nonlinear, second-order differential equation [5]

$$m \frac{dz^2}{dt^2} = -k_c z - \frac{m\omega_0}{Q} \frac{dz}{dt} + F_{ts} + F_v + F_0 \cos \omega t \quad (3.2)$$

in terms of the amplitude (F_0) and operating frequency (ω) of the periodic driving force, quality factor (Q), resonance frequency (ω_0), and spring constant (k_c) of the cantilever. F_{ts} denotes the tip-sample interaction and the second term on the right hand side denotes the hydrodynamic damping with the medium. The Attractive forces (Van der Waals) and the repulsive forces can be calculated from the simulation of sphere interaction with a flat surface, however, for repulsive forces Hertzian contact [6] has to be assumed [7]. The sample viscous response to the tip movement is calculated by [8]

$$F_v = -\eta\sqrt{R\delta}\frac{dz}{dt} \quad (3.3)$$

where η is the sample viscosity, R is the tip's radius, and d is the sample deformation.

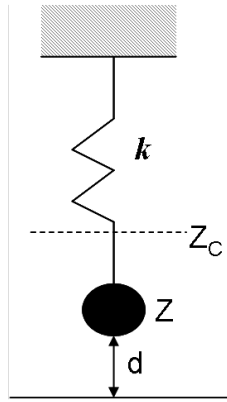


FIGURE 3.5: Impact model of the AFM tip in oscillation.

In this model, the sample is characterized by its elastic and viscosity coefficients. We also considered the effect of adhesion energy hysteresis on phase shifts. This concept is derived from boundary friction studies. The hysteresis was calculated by assuming different adhesion forces between approaching and retracting cycles. Phase shifts are obtained by solving numerically equation 3.2. Experiments and calculations are performed at the cantilever's free resonant frequency. [9] The steady state oscillation or the solution of equation 3.2 was computed to be sinusoidal in nature [10] with a period equal to the period of the driving force as

$$z(z_c, t) = z_0(z_c) + A(z_c) + A(z_c)\cos[\omega t - \phi(z_c)] \quad (3.4)$$

where z_0 , A and ϕ are the mean deflection, amplitude, and phase shift of the oscillation, respectively. It is clear from here that, for any instantaneous variation in the topography

($\Delta h = \Delta z$), the amplitude A can be kept constant by using a feedback control z_c such that Δz_c would follow Δh (Δz) very closely. This would yield the sample topography.

In other terms, equation 3.2 can also be seen as the average rate at which energy is fed into the cantilever must equal the average rate at which energy is dissipated by the cantilever and the tip, under the assumption of energy conservation. Thus, this equation can be re-written as

$$P_{in} = P_{damping} + P_{ts} \quad (3.5)$$

From here one may also calculate the instantaneous power delivered by the driver to the cantilever as . Integrating this over a complete cycle, the average input power results

$$\bar{P}_{in} = \frac{1}{2} k A_d A \omega \sin \phi \quad (3.6)$$

Similarly, average power dissipation due to viscous damping of the cantilever body can be estimated from the expression $F_{damping} = (m\omega_0/Q)dz/dt$ as

$$\bar{P}_0 = \frac{1}{2} b A^2 \omega^2 \quad (3.7)$$

This implies that the power dissipated by the tip-sample interaction would be

$$\bar{P}_{ts} = \frac{1}{2} \frac{k A^2 \omega}{Q} \left[\frac{Q A_d \sin \phi}{A} - \frac{\omega}{\omega_0} \right] \quad (3.8)$$

Though, dynamics observed from the solution of equations based on energy would explain the observed experimental behavior, it does not provide a clear insight on the nature of the forces involved during the interaction. However, force-based equations can provide comprehension of the nature of forces. The behavior of an oscillating tip under long-range attractive and short-range repulsive forces has been computed before [11] based on the following considerations. The long-range attractive forces (van der Waals forces) for a sphere-flat geometry when $d > A_0$ could be estimated as

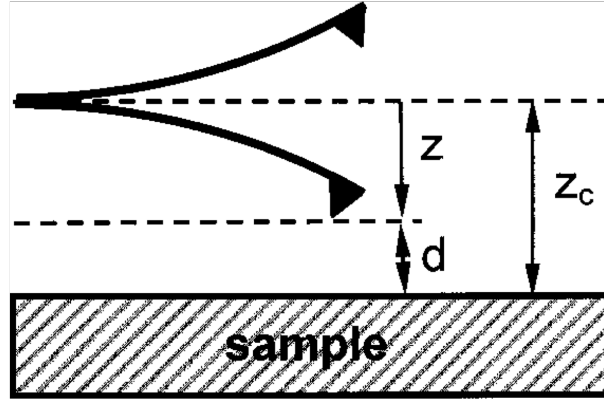


FIGURE 3.6: Scheme of the oscillating tip and the sample. The average cantilever position is defined as the origin of the z coordinate. The instantaneous tip-sample separation d is the sum of the rest separation z_c (positive) and z .

$$F_{ts}(z_c, z) = -\frac{HR}{6(z_c + z)^2} \quad (3.9)$$

where H is the Hamaker constant, R the tip radius, z_c the tip-sample rest distance and d the tip-sample instantaneous separation. Average cantilever's position is defined as its rest position and also the origin of z coordinate. As can be seen in fig. 3.6, $d = z_c + z$. a_0 is an intermolecular distance that is introduced to avoid the divergence of eq. 3.2. For separations $d < a_0$ or short range forces, there are repulsive forces arising from Pauli and ionic repulsion and also the adhesion force during the contact that is given by the Dejarguin-Muller-Toporov (DMT) theory [12]

$$F_{ts}(z_c, z) = 4\pi R\gamma = \frac{HR}{6a_0^2} \quad (3.10)$$

where γ is the surface energy. Then the net force considering the sample deformation as described by DMT contact mechanics could be written as

$$F_{ts}(z_c, z) = -\frac{HR}{6a_0^2} + \frac{4}{3}E^*\sqrt{R}(a_0 - z - z_c)^{3/2} \quad (3.11)$$

where E^* is the effect modulus defined in terms of elastic modulus ($E_{t(s)}$) and the Poisson coefficients ($\nu_{t(s)}$) of the tip (sample) as

$$\frac{1}{E^*} = \frac{(1 - v_t^2)}{E_t} + \frac{(1 - v_s^2)}{E_s} \quad (3.12)$$

Equation 3.2 was numerically solved in Ricardo Garcia et al. [11]. The oscillation amplitude against z_c for various free oscillation amplitudes (A_0) is shown in fig. 3.7(a). In this figure, four well-defined regions can be seen: (1) a flat region when $z_c \gg A_0$. Here the magnitude of attractive force on the oscillation is almost zero. (2) for a fixed A_0 , as z_c tends towards A_0 and lower, the oscillation comes under the long-range attractive force causing a reduction in its amplitude. However, if the working frequency is smaller than the resonance frequency, an initial increase of the amplitude should be expected (Anczykowski, Krüger, and Fuchs). (3) there is a sharp transition region where the amplitude increases. (4) after the transition the amplitude decreases linearly with slope unity.

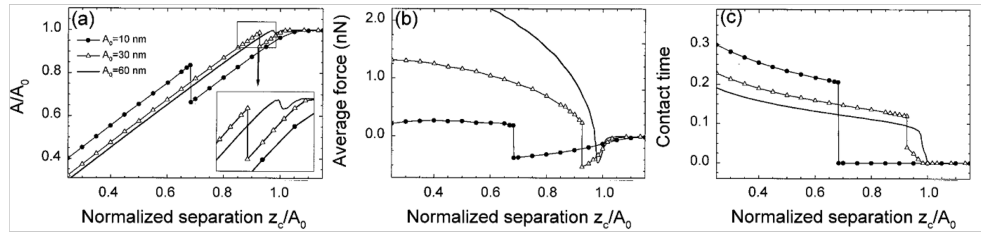


FIGURE 3.7: Calculation of (a) Amplitude, (b) average force, (c) contact time dependence on tip-sample separation for three free amplitudes. The separation z_c is normalized by A_0 [11].

This behavior is well justified also by the nature of the average force experienced by the tip in a single time period. This is shown in fig. 3.7(b) as a function of z_c that is calculated from equations 3.10, 3.11 and 3.12. This has a one to one correspondence with the behavior of amplitude, indicating a good agreement within the four regions already explained before. In brief, at larger distances, there is low magnitude of attractive force, whose magnitude starts to increase as tip approaches the surface. This is followed by a transition to a repulsive regime at a certain point. From there on, the average force shows a slight increase until a maximum occurs.

The time per oscillation during which the tip is in mechanical contact with the surface is known as the contact time t_c . As shown in fig. 3.7c, at large separations where the long-range attractive forces dominates $t_c = 0$. At a certain z_c a step-like discontinuous transition between a purely attractive regime and a repulsive regime is observed. However, for $A_0 = 30$ nm, t_c also shows a steplike discontinuity but this is preceded by a small but continuous change from 0 to 0.02 T (T is the period of tip oscillation). This means that before the jump, the tip is already in intermittent contact with the sample,

i.e., under the influence of short-range repulsive forces. For $A_0 = 60 \text{ nm}$, the slope of t_c during the transition is high but finite. Once the transition has been completed, i.e., when the net force is positive, t_c grows monotonously with z_c decreasing. For standard working conditions, this contact time represents about 10-30% of the period of the oscillation. The relevant point is that there are z_c values where the attractive regime also involves short-range repulsive forces. In other words, there is tip-sample intermittent contact even in the attractive regime.

3.1.3.2 Phase imaging (elastic and inelastic interactions)

Numerical solution of equation 3.2 solved in Ref. [9] would also yield the phase shift, ϕ . The results suggest that for elastic interactions (i.e. dissipating energy=0), the phase shift is independent of the sample elastic modulus over the four order of magnitude range. This is true for both compliant materials and stiff materials. This can be explained as follows. In constant amplitude (A_t) tapping mode, A_t can be defined in terms of tip-sample equilibrium separation and the sample deformation δ as

$$A_t = z_c + \delta \quad (3.13)$$

The configuration of a tip in constant-amplitude tapping mode on a material with varying local elastic properties at positions indicated as 1 and 2 is schematically shown in fig. 3.8a. For example, instantaneous sample deformation (δ) due to the impact of an oscillating tip on stiffer region would be smaller in comparison to the less stiff region. So, for $\delta_1 > \delta_2$, z_{c1} would be smaller than z_{c2} . This change in z_c in different regions compensates the contribution associated with differences in elastic properties. As a consequence, phase shifts in tapping mode should be independent of local variations in the elasticity of the sample. This can also be understood numerically from equation 3.8. Considering, tip-sample interaction to be conservative in nature~ i.e., $P_{tip} = 0$, would yield $\sin\phi = A/A_0$, under normal operating conditions where $\omega/\omega_0 \approx 1$. This clearly says, if the tip loses no energy, that the phase is only dependent on amplitude. In constant amplitude mode, phase would remain constant.

Fortunately, the nature of tip-sample interaction is usually inelastic in nature and this turns out to be the heart of phase-imaging mode. Inelastic interaction is mostly due to the presence of viscous damping or adhesion energy hysteresis. Calculations for phase shift dependence on elastic properties are shown in fig. 3.8b [9] for all the three types of interactions. In his calculations, following parameters were assumed: viscous damping

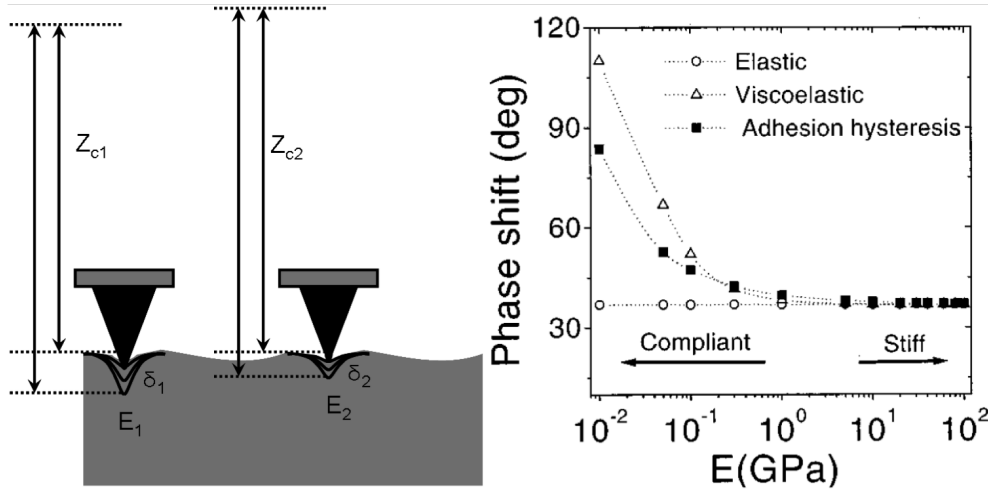


FIGURE 3.8: (a) deformation of sample surface due to tapping (b) numerically calculated phase shift by solving equation 3.2 for materials with varying elasticity.

$\eta = 30 \text{ Pa} \cdot \text{s}$, adhesion energy hysteresis $\gamma_A = 10 \text{ mJ} \cdot \text{m}^{-2}$ (during approach) and $\gamma_R = 60 \text{ mJ} \cdot \text{m}^{-2}$ (during retraction), $A_t/A_0 = 0.6$, $Q = 500$, $k_C = 20 \text{ N/m}$, and $f_t = 200 \text{ kHz}$. It shows that adhesion energy hysteresis and viscous damping both causes a decrease in the phase shift as the sample's stiffness increases. This effect is more pronounced in compliant samples with stiffness below 1 GPa. However, for stiffer samples ($\gg 1 \text{ GPa}$), phase shift remains unaffected. Also, the magnitude of phase shift depends on how the energy dissipates (via damping or adhesion hysteresis). It is important to note that the phase shift would be insensitive to adhesion force variations if the adhesion energy hysteresis were absent.

3.1.3.3 Phase vs tip-sample separation

It is the term “ $\sin\omega$ ” rather than ω that depends on tip-sample power dissipation. Thus, due to symmetric nature of sine $\sim 90^\circ$ it would yield $\phi > 90^\circ$ in attractive regime and $\phi < 90^\circ$ in the repulsive regime. A plot of typical phase against tip-sample separation is shown in fig. 3.9. For separations larger than the free amplitude, there is no phase shift. As the tip comes closer to the sample surface, the attractive force dominates the interaction. The associated positive gradient of the force shifts the cantilever resonance frequency to lower values, which in turn would shift the phase upwards. This is followed by a transition to a lower value, which may be sudden or gradual. During the imaging, if the phase contrast observed is due to this jump from attractive phases to repulsive phases, it is not related to dissipation, but to competition between the attractive and repulsive forces. In samples with weaker viscous damping, a sudden transition

is observed. However, combined effect of viscous damping and adhesion energy hysteresis could reproduce the gradual phase-shift transition from noncontact to intermittent contact. Once there is tip-sample contact, the phase shift decreases with decreasing separation due to the negative gradient of the interaction force. As long as the phase stays on one side of 90° , the microscope is always operating either in the attractive or the repulsive regime. Then, any changes in the phase image are directly due to changes in the energy being dissipated in the tip-sample junction.

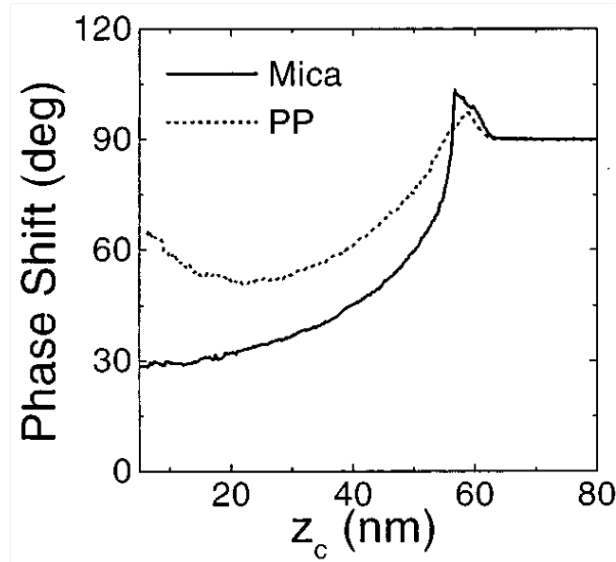


FIGURE 3.9: Phase shift observed in stiff (Mica) and compliant (polypropylene) material against tip-sample separation distance.

The sharp transition between attractive and repulsive forces (shown in fig. 3.7b), can also be observed experimentally as the sharp transition in phase versus tip-sample distance curve (see fig. 3.9). The effect of adhesion energy hysteresis is more noticeable for small tip-sample separations, where adhesion forces may become dominant. The above results emphasize the role of energy dissipation in the sample to obtain phase contrast images during the tapping operation. Phase contrast imaging may arise from differences in elastic properties once the sample has a channel for interacting inelastically with the tip. These results underline the complex behavior of phase shifts in dynamic force microscopy where elastic and inelastic processes alike may be involved. They also open new ways to study relevant interfacial phenomena such as friction, and more generally, energy dissipation at the nanometer scale. In fact, if a few parameters are measured, a phase image can be directly converted into a quantitative image of dissipation.

3.2 Scanning tunneling Microscopy (STM)

The working principle of STM is not very different from AFM. A bias voltage is applied between a sharp metallic tip and the sample. As the tip approaches the surface up to a few Å, the wave functions of tip and surface overlap, resulting in a tunneling current I , which may vary from few pA to nA. The lateral motion of the tip is same as that of AFM. During the lateral motion of the tip over the surface, the feedback loop adjusts the tip-sample distance such that the detected tunneling current remains constant. The mapping of adjusted tip-sample distance over an area is the topography or constant-current image. Compared to AFM, STM has a couple of advantages: (1) Extremely high z-resolution of a few pm can be achieved due to exponential dependence of tunneling current on tip-sample distance. (2) Since the tunneling current flows mainly through the few atoms at the very apex of the tip, STM has a lateral resolution on the atomic scale.

The tunneling current I as a function of bias voltage V is described by Tersoff-Hamann model (TH-model) [13].

$$I(V) \propto \int_{-\infty}^{-\infty} \rho_s(E) \rho_t(E - eV) \tau(E, V, z) (f(E - eV, T) - f(E, T)) dE \quad (3.14)$$

where ρ_t , ρ_s are the local density of states (LDOS) of the tip ρ_t and the sample ρ_s , respectively. τ is the transmission matrix of the tunneling gap and f is the fermi function. An often used expression for τ derived from a trapezoidal barrier is

$$\tau(E, V, z) = \exp\left(-2z \sqrt{\frac{m_e}{\hbar^2} (\phi_s + \phi_t - 2E + eV)}\right) \quad (3.15)$$

where ϕ_s and ϕ_t are the work functions of tip and sample, respectively.

For STM measurements that are performed at bias voltages V close to the Fermi level τ can be assumed to be bias independent since $V \ll \phi$. It follows that τ can be approximated to

$$\tau(E, V, z) = \exp\left(-2z \sqrt{\frac{m}{\hbar^2} (\phi_s + \phi_t)}\right) \quad (3.16)$$

If the finite temperature is neglected, eq. 3.14 simplifies to

$$I(V) \propto \int_0^{eV} \rho_s(E) \rho_t(E - eV) \tau(E, V, z) dE \quad (3.17)$$

In Scanning Tunneling Spectroscopy (STS), I-V curves (or dI/dV curves) is measured under open feedback loop conditions. From equation 3.14, the tunneling current can be calculated. Under the assumption that ρ_t and the transmission matrix τ are independent of V, at low bias and low temperature, the dI/dV signal is directly proportional to the LDOS

$$\frac{dI}{dV} \propto \rho_s(eV)\rho(0) \quad (3.18)$$

Thus, In dI/dV images, the lateral distribution of the LDOS at distinct energies is mapped. This technique is frequently used in this work and combines spectroscopic information with a high spatial resolution.

3.3 Electron beam induced current

The ‘‘Electron Beam Induced Current’’ method (EBIC) employs an electron beam (normally, used as in SEM) on a sample to induce current that can be detected with the amplifier. See the EBIC schematic in figure 3.10. This is then displayed on a monitor that is synchronized with the electron beam scan. The EBIC contrast arising usually depends on the material characteristics. This is often used to study locations of p-n junctions, buried junctions, defects or doping non-homogeneities and to extract minority carrier characteristics: lifetime and diffusion length in the sample.

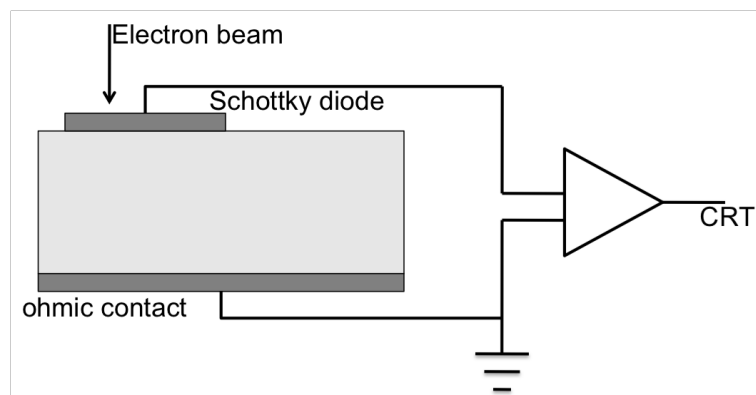


FIGURE 3.10: Schematic of EBIC signal due to electron-hole pair generated from the electron beam incident normal to the rectifying barrier.

3.3.1 Electron-hole pair generation

When a semiconductor sample is bombarded with high-energy electron beam I_b , ΔN number of electron-hole pairs are generated. This phenomenon is known as electron voltaic effect (EVE). ΔN is given by $\Delta N = \frac{GI_b}{q}$. I_b is the beam current and G is expressed as $G = (1 - f)(E_b)/(e_i)$, where f is the average fraction of the energy of the incident electron beam lost by backscattering, E_b is the energy of the incident electron beam and e_i is the ionization energy (effective average energy required to generate electron-hole pair). Formation energy e_i can be calculated from the following relation [14]

$$e_i = 2.1E_g + 1.3 \quad (3.19)$$

The energies required to generate electron-hole pairs in a number of materials are listed in Table [15] 3.1.

TABLE 3.1: Electron-hole pair formation energies for various semiconductors.

Material	e_i (eV)
C(diamond)	13.07 [16]
Ge	2.84 [17]
Si	3.6 [17]
GaAs	4.4 [18]
GaP	7.8
InP	2.2
SiC	9.0 [19]
SiC (6H)	11.3

If the sample is grounded, the current that is measured during the electron bombardment is the specimen current I_s . It is simply given as $I_s = I_b - I_e$, where I_e is the total emitted current. In the presence of a depletion region, the electron hole pairs generated in the depletion region are separated by the built-in electric field, and if the junction is short circuited, a current of this total number of carriers per second will flow externally. This is referred to as short-circuit current I_{sc} or EBIC current. It can be obtained from any form of rectifying electrical barrier such as Schottky junction, p-n junction.

3.3.2 Carrier dynamics

The electron beam is narrowly focused on to the specimen where the electrons scatter in an interaction volume (microns wide). This limits the resolution of EBIC measurements.

Using Monte Carlo simulations, beam-specimen interaction can be accounted for. One may also use this method to compute appropriate values for the backscattering loss factor f and to estimate depth-, lateral- and radial-dose distribution.

For a surface-parallel Schottky and p-n junctions, the continuity equation for excess minority carrier density $n(r,t)$ at location r and time t is established as

$$-\frac{\partial n(r,t)}{\partial t} = -D\nabla^2 n(r,t) + \mu\nabla(E(r,t)) + \frac{n(r,t)}{\tau(r)} - g(r,t) \quad (3.20)$$

in terms of diffusion current $D\nabla^2 n(r,t)$, drift current $\mu\nabla(E(r,t))n(r,t)$, recombination rate $-\frac{n(r,t)}{\tau(r)}$ and beam induced generation rate $g(r,t)$. Here D is the carrier diffusion constant, τ the total minority carrier lifetime defined as $\tau(r) = (\tau_r^{-1} + \tau_{nr}^{-1})^{-1}$ and μ the minority carrier mobility. In a neutral bulk semiconductor, electric fields can be neglected and thus continuity diffusion equation formed would be

$$D\nabla^2 n(r) - \frac{n(r)}{\tau(r)} + g(r) = \frac{\partial n(r)}{\partial t} \quad (3.21)$$

and in steady state $\frac{\partial n(r)}{\partial t} = 0$

The point source of carriers at position r is assumed to behave as a delta function ($g(r) = g_0\delta(r - r_0)$) and the solution of equation in steady state at a point at a distance r' from the source is

$$n(r') = \frac{g_0}{4\pi D} \frac{\exp(-r'/L)}{r'} \quad (3.22)$$

where L is the diffusion length.

In the case of a Schottky contact, using the method of mirror images [20] of electrostatics, carrier density is given by the Green's function.

$$n(r) = \frac{1}{4\pi D} \left[\frac{1}{r_1} \exp(-r_1/L) - \frac{1}{r_2} \exp(-r_2/L) \right] \quad (3.23)$$

The number of carriers collected per unit time is obtained by integrating the vertical carrier flux over the surface

$$I = eD \iint_{r=r_b} dA \frac{\partial n}{\partial z} = \exp\left(-\frac{z_0}{L}\right) = \phi \quad (3.24)$$

ϕ is the charge collection probability i.e. the current due to a unit source at the point r at a depth z_0 .

Multiplying the source strength g (number of carriers generated per second) at each point by the collection probability and integrating over the generation volume gives the EBIC current as I_{EBIC}

$$I_p = \int_0^{\infty} \exp(-z/L) g(z) dz \quad (3.25)$$

If the beam is slowly moved away from the diode, I_{EBIC} decays with beam-to-diode distance, d , according to the relationship [21]

$$I(d) = A \frac{\exp(-d/L)}{d^\alpha} \quad (3.26)$$

where A is a constant. For a planar junction configuration, this equation is accurate for $d < L$. It should be noted that the value of α depends on the surface recombination velocity v_s . It varies from $\alpha = -1/2$, for $v_s = 0$ [22] to $\alpha = -3/2$, for $v_s = \infty$ [23]

When the stationary beam, incident near a detecting barrier, is chopped off, the decay characteristic of the EBIC current is often expressed in the form [24]

$$I(t) = I(0) t \exp\left(-\frac{t}{\tau}\right) \quad (3.27)$$

This indicates that EBIC can be effectively used to calculate minority carrier lifetime.

3.3.3 EBIC Contrast

The contrast in EBIC micrograph, which is mainly due to the differences in recombination rate at certain sites, is given by

$$c(\xi) = \frac{I^*}{I_p} = \frac{I(\xi)}{I_p} \quad (3.28)$$

$$I_p = I(\xi \rightarrow \infty) \quad (3.29)$$

where ξ is the lateral beam position relative to the defect and I_p is the EBIC current in a defect-free region, also known as matrix signal and I^* is the reduction in EBIC current due to recombination at defects. Usually, the central $c(0)$ is denoted “the (maximum) contrast value” $c(0) = \frac{I_p - I_d}{I_p}$.

Mostly, these sites are related to electrically active defects as they are potential recombination centers. Therefore, EBIC is specifically used to study defects. For instance, dislocations are associated with a high recombination rate, and consequently, appear as dark lines in EBIC map [Lander et al. 1963].

The defects can be modeled with a region of reduced minority carrier lifetime τ' with respect to that of the bulk τ . Donolato. All the following formula were first written by Donolato

In the volume recombination model (VRM), the dislocation is characterized by a cylindrical region Ω_D where the total minority carrier lifetime τ' differs from the bulk value τ . The radius r_D of the dislocation cylinder may be interpreted as a “capture cross section” which could be directly associated to the dislocation physical properties such as physical dimensions, strain field, or to the space charge region, if it is charged. The recombination current is given by

$$I^* = \frac{1}{\tau'} \int_{\Omega_D} p(r) d\Omega \quad (3.30)$$

or

$$I^* = \frac{\sigma_D}{\tau'} \int_l p(r) dl \quad (3.31)$$

The first term is defined as the recombination strength or line recombination velocity of the dislocation, expressed as $\gamma = \sigma_D / \tau'$

In case of point defect, its strength is defined as The defect induced recombination strength is given by

$$\gamma = l^3 \left(\frac{1}{L'^2} - \frac{1}{L^2} \right) \quad (3.32)$$

where $L'^2 = D\tau'$. Since, dislocation considered as a row of point-like defects, its recombination strength can be expressed similarly

$$\gamma = \pi r_D^2 \left(\frac{1}{L'^2} - \frac{1}{L^2} \right) = \frac{\pi r_D^2}{D} \left(\frac{1}{\tau'^2} - \frac{1}{\tau^2} \right) \quad (3.33)$$

This is under the assumption that $r_D \ll L$.

For $L' \ll L$, this can be also be expressed in terms of thermal velocity and line density of recombination centers n_r along the dislocation $\gamma = (n_r \sigma_r v_{th})/D$ where v_{th} is defined as $v_{th} = 1/(N_r \sigma_r v_{th})$.

EBIC to provide information on the location or identification of the junction, diffusion length and also to estimate surface recombination parameters. However, EBIC mapping also reveals grain boundaries, which also act as recombination centers. The theory of EBIC contrast is applicable not only on point defects but also on other kind of defects such as, line defects, dislocation half loops or stacking faults etc and as well as grain boundaries. This type of study is used for the determination of the electronic properties of dislocations and to identify dislocations whose characteristics are either dependent on their core structure or on impurity decoration.

3.4 Photoluminescence (PL)

Photoluminescence is the spontaneous emission of photons from a material under optical excitation. PL investigations is typically used to characterize different materials properties, such as band parameters, impurity levels etc. Under pulsed excitation, PL intensity transients can yield lifetimes of excited states. In addition, PL is also used to study thermally activated non-radiative recombination processes. Following is the brief description of PL setup:

Figure 3.11 illustrates the photoluminescence setup. The sample is excited by guiding laser (either with an continuous-wave (cw) laser or a pulsed laser system, producing pulses of 5 ns duration at 20 Hz repetition rate) onto it by a set of lenses and mirrors. An helium cryostat is used to cool down the samples from room temperature 300 K to liquid helium temperature 4.2 K. Using a two lens system, the PL signal is collected into the scalable width entrance slit of a single grating monochromator (Czerny-Turner). An appropriate filter is placed between the telescope system and the entrance slit of the monochromator, to filter out the laser light which is much stronger than the fluorescence signal. The signal is detected with a nitrogen cooled CCD placed at the exit slit of the

monochromator. The detected signal is filtered out and amplified by a lock-in-amplifier locked at the laser frequency. Both the spectrometer and the CCD are controlled through a Labview program and the collected signal is recorded in a personal computer.

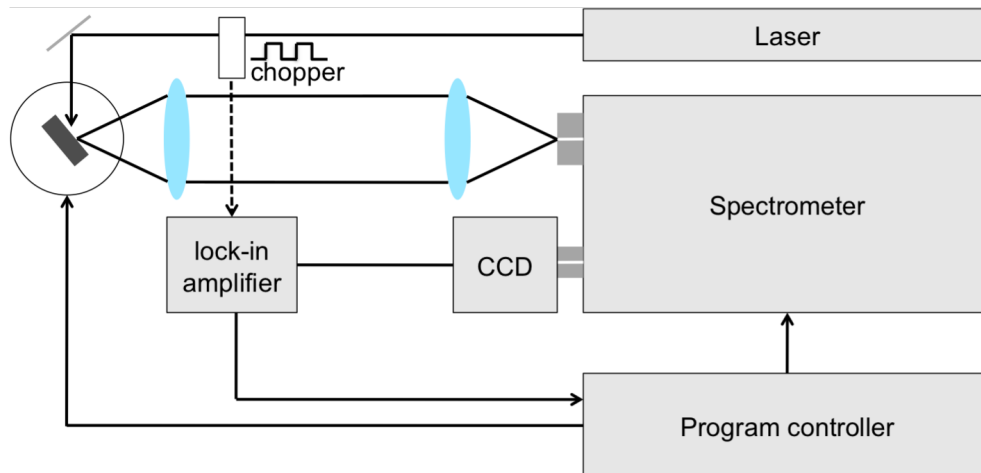


FIGURE 3.11: Photoluminescence spectroscopy setup.

3.5 X-ray photoelectron spectroscopy (XPS)

In XPS, when the sample is bombarded with X-rays, as a result of a photoemission process electrons are liberated from the specimen. The energy of the electrons ejected from the atomic energy levels is analysed by the spectrometer using a Hemispherical sector analyzer (HSA) combined with a detection system (shown in fig. 3.12). Commonly used X-ray source are those providing Al- K_{α} radiations with line energies and line widths of 1486.6 eV and 0.85 eV, respectively. The kinetic energy (K.E) of the electron released is expressed as $K.E = hv - B.E - \phi$, where hv is the incident beam energy, $B.E$ is the binding energy and ϕ is the work function of the spectrometer. XPS measurements requires a ultra high vacuum (UHV) chamber to prevent scattering of low energy electrons by residual gas molecules which leads to loss of energy and loss of intensity.

XPS is commonly used to identify the elements. The quantification of the composition of the specimen can also be carefully performed. The molar fraction x_A in a homogeneous specimen composed of i elements, is given by

$$x_A = \frac{I_A/S_A}{\sum I_i S_i} \quad (3.34)$$

where I_i is the area of the peak generated by constituent i and S_i is its relative sensitivity factor.

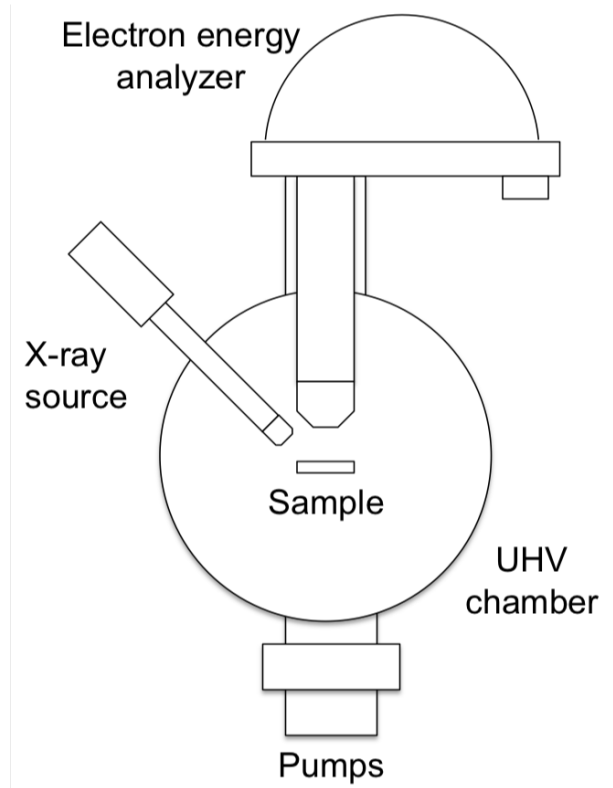


FIGURE 3.12: X-ray photoelectron spectroscopy setup.

The primary beam has a penetration depth of a few micrometers. The photoelectron travel a limited distance, called attenuation length λ , before being inelastically scattered. The characteristic depth d from which photoelectrons are emitted, called the escape depth, is given by:

$$d = \lambda(E) \cos\theta \quad (3.35)$$

where θ is the angle of emission from the surface normal. Typical values of λ are in the range of 1 to 10 atom layers [25].

3.5.1 Angular resolved XPS

When a more surface sensitive is required, this method is approached. In this case, photoelectron is collected from a titled surface. The tilt is defined as α , the angle between the plane of the surface and the analyzer. In this way, the intensity I of electrons emitted from a depth d is given by the Beer-Lambert relationship:

$$I = I_0 \exp\left(-\frac{d}{\lambda \sin\alpha}\right) \quad (3.36)$$

where I_0 is the intensity from an infinitely thick clean substrate.

Bibliography

- [1] G. Binnig, H. Rohrer, Ch. Gerber, and E. Weibel. *Phys. Rev. Lett.*, 50:120–123, 1983.
- [2] R. W. Carpick, D. F. Ogletree, and M. Salmeron. *J. Colloid Interface Sci.*, 211:395–400, 1999.
- [3] B. Bhushan. *Springer Handbook of Nanotechnology*. Springer, 3rd edition, 2010.
- [4] O. Klymenko, J. Wiltowska-Zuber, M. Lekka, and W.M. Kwiatek. *Acta Physica Polonica A*, 115:548–551, 2009.
- [5] A. S. Paulo and R. Garcia. *Phys. Rev. B*, 64:193411, 2001.
- [6] A. C. Fischer-Cripps. *J. Mat. Sci.*, 34:129–137, 1999.
- [7] J. Tamayo and R. Garcia. *Langmuir*, 12:4430–4435, 1996.
- [8] R. Garcia, C. J. Gomez, N. F. Martinez, S. Patil, C. Dietz, and R. Magerle. *Phys. Rev. Lett.*, 97:016103, 2006.
- [9] J. Tamayo and R. Garcia. *Appl. Phys. Lett.*, 71:2394, 1997.
- [10] M. V. Salapaka, D. J. Chen, and J. P. Cleveland. *Physical Review B*, 61:1106–1115, 2000.
- [11] R. Garcia and A. S. Paulo. *Phys. Rev. B* 60, 60:4961–4967, 1999.
- [12] B.V. Derjaguin, V.M. Muller, and Yu.P. Toporov. *J. Colloid Interface Sci.*, 53:314–326, 1975.
- [13] J. Tersoff and D.R. Hamann. *Phys. Rev. B*, 31(2):805–813, 1985.
- [14] C. A. Klein. *J. Appl. Phys.*, 38:2029–2038, 1968.
- [15] D. B. Holt and D. C. Joy. *SEM microcharacterization of semiconductors*. Academic press Ltd., 1989.

-
- [16] M. Hage-Ali S. F. Kozlov, R. Stuck and P. Siffert. *IEEE Trans. Nucl. Sci.*, NS-22:160, 1975.
- [17] C. J. Wu and D. B. Wittry. *J. Appl. Phys.*, 49:2827, 1978.
- [18] R. Kalibjian and K. Maeda. *Sol. State Electron.*, 14:529, 1971.
- [19] G. P. Golubev, V. S. Vavilov, and V. D. Egorov. *Sov. Phys. Sol. State*, 7:3000, 1966.
- [20] C. Donolato. *Optik*, 52:19–36, 1978/79.
- [21] H. K. Kuiken and C. van Opdorp. *J. Appl. Phys.*, 57:2077–2090, 1985.
- [22] J. Boersma, J. J. E. Indenkleef, and H. K. Kuiken. *J. Eng. Math.*, 18:315–333, 1984.
- [23] D. E. Ioannou and C. D. Dimitriadis. *IEEE Trans.*, 29:445, 1982.
- [24] D. E. Ioannou. *J. Phys. D: Appl. Phys.*, 13:611–616, 1980.
- [25] M.P. Seah and W.A. Dench. *Surf. Interface Anal.*, 1:2, 1979.

Chapter 4

GaN

In this chapter, we have studied surface, electrical and optical properties of non-intentionally doped (nid) GaN. Though this kind of commercially available GaN has been widely studied, its characterization provided a setup as a bench to develop techniques that could be further extended to study other complex nitrides, such as InGaN, AlInN and AlGaN. This characterization is also one of the main objectives of this chapter.

4.1 Surface and electrical properties

The GaN template (3 μm thick) used in this study was Aixtron MOCVD grown at $1050^\circ C$ on sapphire using a low temperature ($\sim 530^\circ C$) GaN nucleation layer. Here, we report on the study of electrical properties of threading dislocations in nitrides. We performed C-AFM and SKPM on GaN and studied the behavior of conductivity and surface potential associated with the threading dislocations. The experimental section below would enlighten the working principles of SKPM.

4.2 Experimental section

Scanning Kelvin Probe Microscopy (SKPM) were performed in ambient conditions with NT-MDT Solver pro47. For these measurements, AFM tips coated with Pt/Ir (68 kHz) and B-doped diamond (180 kHz) were used. We explain the fundamentals of techniques in brief here but could also be read somewhere else. When AFM tip is separated by distance z from the surface results in a capacitive energy $dE = dC \cdot \frac{V_c^2}{2}$, where $C(z)$ is the effective capacitance formed and V_c is the potential difference between the tip and surface. C can be approximated by and is dependent on permittivity of the material. V_c

can be approximated by $eV_{CPD} = \phi_{tip} - \phi_{sample}$ in the absence of induced charge or surface dipoles and external bias. Thus, the force of attraction is given by

$$F = \frac{dE}{dz} = \frac{V^2}{2} \frac{dC}{dz} \quad (4.1)$$

EFM measurements were performed when $V_{app} = V_{dc} + V_0 \sin \omega t$ is applied between the tip and sample. In this case,

$$F = -\frac{1}{2} \frac{dC}{dz} \left[\left((V_{CPD} + V_{dc})^2 + \frac{V_0^2}{2} \right) + 2V_0(V_{CPD} + V_{dc}) \sin \omega t - \frac{V_0^2}{2} \cos 2\omega t \right] \quad (4.2)$$

From the above expression, it can be seen that electrostatic interaction in tip-sample system has a DC, first and second harmonic component. By applying a kelvin voltage (dc) to minimize the first order oscillation would give us a surface potential map. The amplitude of the second harmonic oscillation is directly proportional to dC/dz . The term dC/dz is widely accepted as related to local dielectric constant of the material. Our measurements were performed in two-pass mode. In the first pass, surface profile is obtained in semi-contact mode. In the second pass, tip closely follows the same profile but at a distance $z=5$ nm from the surface with an applied bias of bias $V_{ac} = 0.8 \star \sin(67kt)$. Depending on the kind of measurements (SKPM or SCM), either DC bias is applied to minimize the oscillation of the first harmonic or oscillation amplitude of the second harmonic is measured.

4.2.1 Sensitivity of KPFM

In our measurements, the sensitivity of the smallest measureable VCPD was calculated [1] form

$$V_{CPD,min} = \sqrt{\frac{2k_B T k B}{\pi^3 Q f_{res}}} \left(\frac{1}{\epsilon_0 V_{ac}} \right) \left(\frac{d}{R} \right) \quad (4.3)$$

where k_B is the Boltzmann constant, T the temperature, B the bandwidth in which the experiment is performed, k the spring constant and Q the quality factor.

Two types of AFM tip were used for kelvin probe measurements: Pt-coated silicon tip ($f_{res} = 48$ kHz, $k = 0.6$ N/m, $Q = 400$, $R = 35$ nm) and highly p-doped diamond tip ($f_{res} = 210$ kHz, $k = 72$ N/m, $Q = 400$, $R = 150$ nm).

For the silicon tip, the sensitivity of V_{CPD} is ~ 50 μV and for diamond tip, ~ 70 μV .

4.3 Results and discussions

Figure 4.1a shows the $60 \times 60 \mu\text{m}^2$ topography of GaN surface where step-features and V-shape defect can be observed. These are typical features of MOCVD GaN surface. The estimated V-shape defect density was $\sim 10^6 \text{cm}^{-2}$. Their size varied as 20-50 nm in diameter and upto 5 nm in depth. The depth measured here with AFM is underestimated due to comparable sizes of the AFM tip and V-defects. Figure 4.1b is the corresponding C-AFM map obtained with an applied bias of +6 volts to the AFM tip with respect to the grounded sample. By the comparison between fig. 4.1a and b, it is possible to notice that the facets $\{1\bar{1}01\}$ of V-shape defects show a much higher conductivity with respect to the defect-free surface. In the present measurement conditions, local current at the V-defect facets increased up to a maximum of 500 pA. The current in the defect-free area is $\sim 56 \text{ pA}$, which is associated to the noise level. Considering the ‘‘AFM tip-surface’’ contact formation to behave as a metal-semiconductor Schottky junction, the current I in the forward bias would exponentially depend on the barrier height by the relation:

$$I = AA^* \exp\left(-\frac{q\phi_B}{kT}\right) \left(\exp\left(\frac{qV}{nkT}\right) - 1\right) \quad (4.4)$$

As shown in equation 4.4, at constant applied bias, the current increment in the V-defects can be explained by the reduced surface barrier height $\phi_{B,V\text{-defect}}$ at the V-defect facets in comparison to the defect-free surface. This is justified from the surface potential distribution, as described in the following part. The SKPM map of the same area of fig. 4.1a is shown in fig. 4.1c, while the comparison between morphology, current and surface potential profiles is shown in fig. 4.1d. In correspondence to all the V-defects observed in fig. 4.1a, a significant reduction in the surface potential occurs reaching in some cases a maximum value of 1.2 eV. This value is 6 to 12 times higher than the change in surface potential observed for charged dislocations in GaN reported before [2]. This suggests that the reduced surface potential cannot be associated to the negatively charged dislocations emerging at the V-defects. It is also important to worth noting that in case of a negatively charged dislocations, an increment in surface potential is expected.

This huge lowering in surface potential measured at the V-defects in GaN can be explained by either of the two mechanisms (1) N-termination of V-shape defects and/or (2) formation of inversion domains. Ga-terminated $\{1\bar{1}01\}$ surfaces of V-defect facets constitute a high density of dangling bonds (16.0 nm^{-2}) in comparison to low density of dangling bonds, 11.4 and 12.1 nm^{-2} associated with Ga-terminated (0001) and $(1\bar{1}00)$

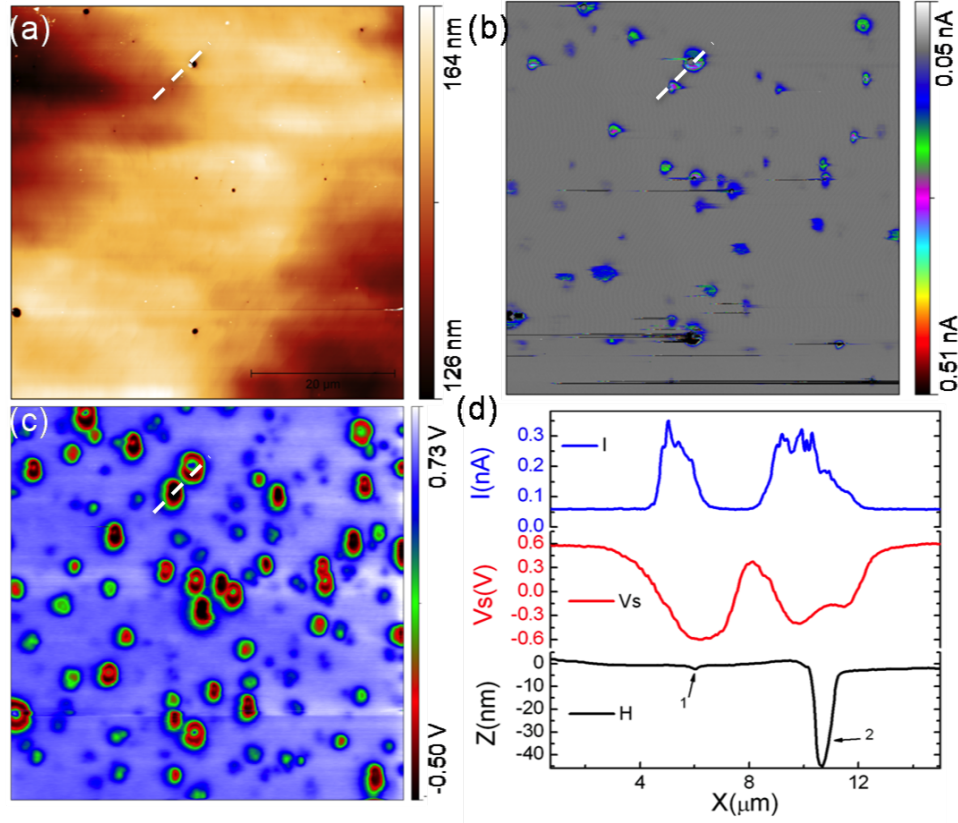


FIGURE 4.1: (a) $60 \times 60 \mu\text{m}^2$ topography and its corresponding (b) C-AFM map obtained at +6V and (c) SKPM map of unintentionally doped $3 \mu\text{m}$ GaN. (d) Height, current and surface potential profile across the two V-defects of different sizes marked with the dashed line in a, b and c.

surfaces, respectively, which makes it energetically less favorable. As observed by Hir-matsu et al. [3], the formation of $\{1\bar{1}01\}$ surfaces associated with V-defects facets, can only be explained if they are N-terminated (schematically shown in fig. 4.2). First principle calculations and experimental values by Grossner et al. [4] and Rosa et. al [5] show that the N-termination of the surfaces of GaN leads to a significant increment in electron affinity by 2 to 3 eV. Consequently, an increment in the electron affinity would decrease the potential barrier height at the V-defects (schematically shown in fig. 4.3) in good agreement with Lochthofen et al. [6]. Though the electrical properties of the V-facets are well explained here, it is important to enlighten their origin. V-shape defects in GaN are usually associated to pinholes and nanotubes and have been reported before [7]. Their termination in the shape of inverted pyramidal hexagonal structure is mostly determined by the presence of impurities (O, Si) during the growth, when an impurity located at a specific site can initiate or forbid the growth along various surfaces such as (0001), $\{1010\}$ and $1\bar{1}01$ surfaces. Pinholes have also been reported to be associated with inversion domains, which suggest presence of N-polar domain in Ga-polar GaN[7].

Under both the mechanisms, either N-termination or formation of inversion-domains, a significant reduction in the surface potential is expected.

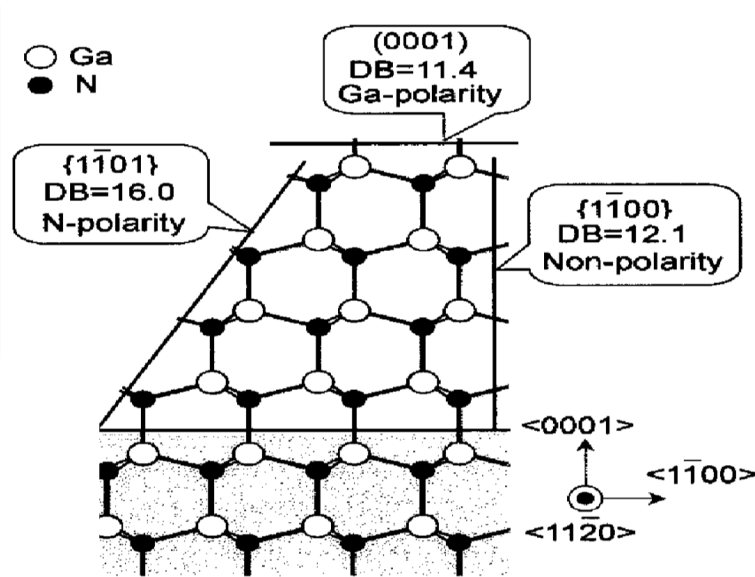


FIGURE 4.2: (a) Schematic of GaN surfaces $\{1\bar{1}01\}$, $\{0001\}$ and $\{1\bar{1}00\}$. Their respective dangling bond density (DB) and polarity is indicated. (from Hirnatsu et al.[3])

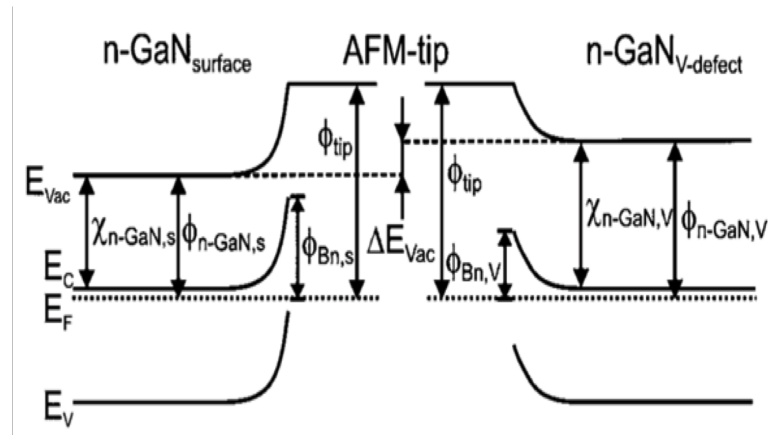


FIGURE 4.3: Schematic band diagram of the interface between the AFM tip and the planar surface (left side) and between the AFM tip and the V-defects (right side). The Schottky barrier for the planar surface is $\phi_{Bn,s}$ and for the V-defects $\phi_{Bn,V}$. The dashed lines mark the difference in the vacuum levels of the planar surface and the V-defects, ΔE_{vac} . (from Lochthofen et al. [6])

In order to sort out the right mechanism, we have carried out EBIC measurements on Au-Schottky junction. Figure 4.4 (a) and (b) show the EBIC map obtained separately with incident beam energies of 3.5 keV and 5.3 keV, respectively. The energy dissipation volume would be larger and deeper at 5.3 keV in comparison to 3.5 keV. Monte carlo simulation of energy distributions for the two beam energies are shown in fig. 4.5, (a) is obtained for 3.5 kV and (b) for 5.3 kV. It is clear that the maximum energy

distributed for 3.5 kV is near the Au/GaN interface and for 5.3 kV is more in the bulk. The EBIC map at 3.5 kV shows regions with dark contrast that would relate to (1) recombination at dislocations and (2) local reduction in barrier height at V-defects, as EBIC is also known to be influenced by inhomogeneous barrier height. However, EBIC map at 5.3 kV shows an additional appearance of bright contrast (enhanced EBIC current) occurring with a density $\sim 10^6 \text{ cm}^{-2}$, which is close to the density of V-shaped defect calculated with AFM. This can be explained from the band diagram (fig. 4.4d) near an inversion domain in c-GaN. An inversion domain would lead to the formation of buried (0001)/(000 $\bar{1}$) junction with a high charge density distribution across the junction owing to the presence of strong spontaneous polarization fields in GaN. Using Schrödinger-Poisson solver (nextnano), the electric field across this junction is $\sim 0.6 \text{ MV/cm}$ was calculated. A Schottky barrier height of $\sim 0.6 \text{ eV}$ was used as the boundary condition. The enhancement of EBIC current near this high internal electrical field at the V-defects can be understood in terms of EBIC gain (defined as the ratio of EBIC current to the beam current). Using the model proposed by Gibson et al. [8] for inhomogeneous Schottky barrier distribution, EBIC current gain $G_{V\text{-defect}}$ at the inversion domain for the incident electron beam energy E is by given by

$$G_{V\text{-defect}} = \frac{E}{2\varepsilon} \left[1 + \frac{\alpha^2(3 - \alpha)}{4} \right] \quad (4.5)$$

where $\alpha = \frac{2W}{R_p}$, W is the depletion width and R_p is the mean electron range. In this case, the depletion width at the inversion domain is much higher than the depletion width of Au-Schottky barrier. From our simulations, W is obtained as $\sim 200 \text{ nm}$. However, in the case of a defect free area where depletion is caused by the Schottky contact was obtained as $\sim 150 \text{ nm}$ for a barrier height of 1.6 eV. This suggests that α is higher for inversion domains with respect to Schottky contacts.

From the equation 4.5, one would obtain $G_{V\text{-defect}} > G_{\text{defect-free}}$, which implies a higher EBIC current near the inversion domain. This clarifies that the association of inversion domains to V-shaped defects is the main cause of very low surface potential, localized high conductivity in GaN.

Besides such deep lowering of surface potential at the V-defects, shallow/mild reductions were also observed (fig. 4.6b) near the sites where GaN terrace steps terminate (fig. 4.6a). The dislocations are marked as 1 and 2. The termination of the steps is due to the interaction of dislocation (screw-type) with the terraces [9]. Since, the minimum step size in GaN $\sim 0.25 \text{ nm}$, the termination would appear as shallow grooves as shown in fig. 4.6(a). This suggests that the two dislocations marked are either pure screw-

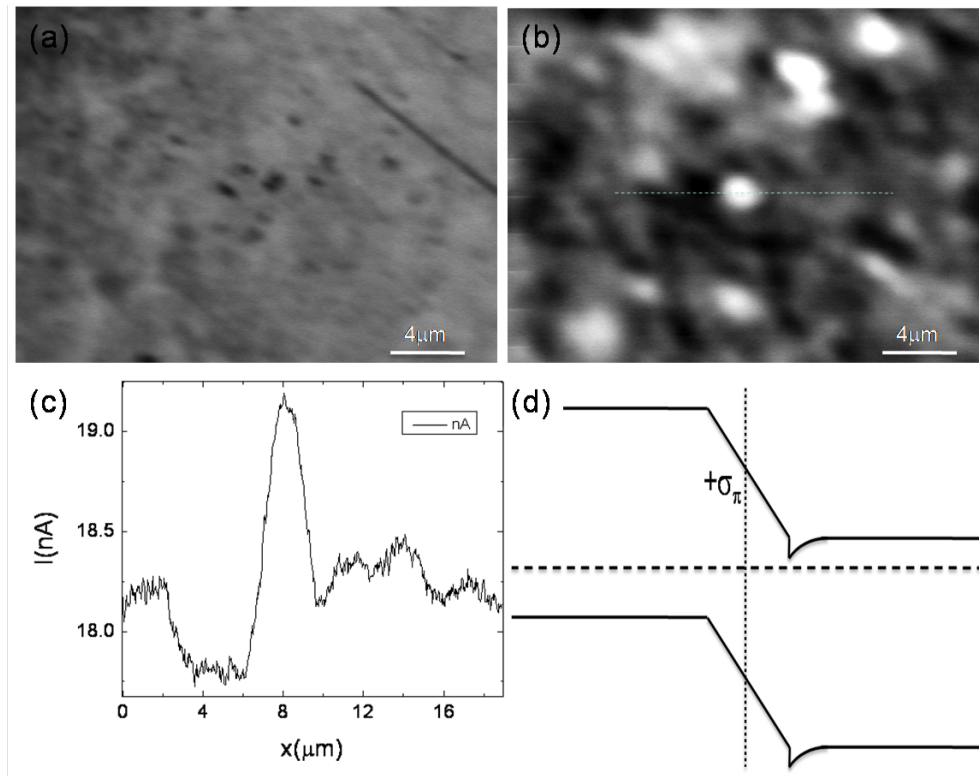


FIGURE 4.4: EBIC map obtained at (a) 3.5 kV and 5.3 kV. Dark contrast in (a) is due to lower barrier height at V-defects and recombination at dislocations. Bright contrast in (b) is associated to the presence of inversion domains, which (c) EBIC current profile across the inversion domain marked with dashed line in (b). (d) Band diagram showing the presence of polarization induced high electric field at the $(000\bar{1})/(0001)$ junction.

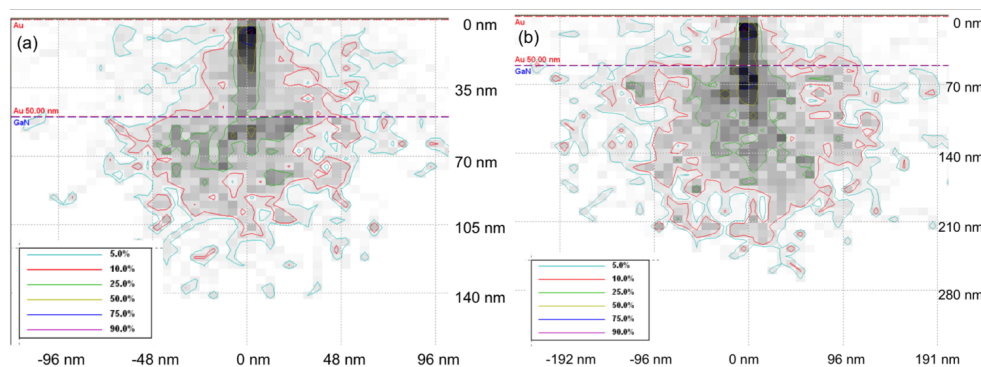


FIGURE 4.5: Monte Carlo Simulation of energy distributions in Au(50 nm)/GaN for (a) 3.5 kV and 5.3 kV.

or mix- type threading dislocations. Figure 4.6(b) is the corresponding SKPM map of the topography shown in fig. 4.6(a). Topography and surface potential profile across the two dislocations 1 and 2 are shown in fig. 4.6c. The maximum potential lowering observed was around 75 meV in dislocation 1 and 0.1 V in dislocation 2.

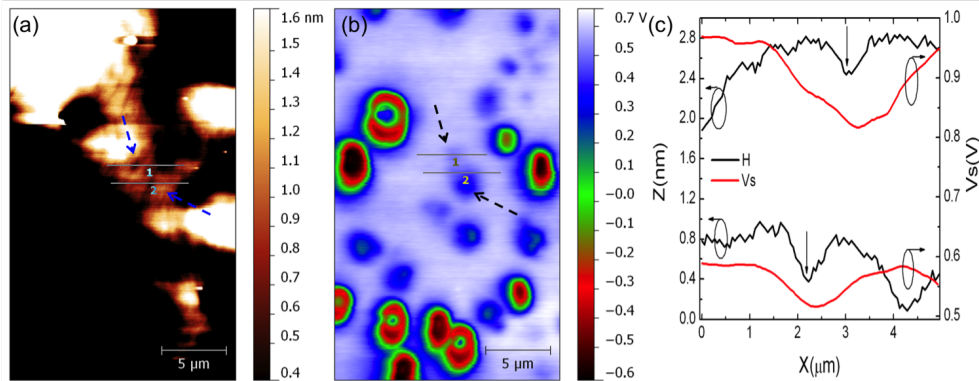


FIGURE 4.6: (a) $15 \times 30 \mu\text{m}^2$ topography and its corresponding (b) SKPM map of unintentionally doped $3 \mu\text{m}$ GaN. (c) Surface potential profile across the two dislocations (with screw component) marked with dashed line in (a) and (b).

Our micro-electrical characterization results suggest that leakage current in GaN devices would strongly depend on the growth condition. In cases where there is a high density of inversion domains and/or large density of V-defects, leakage current would be dominated by their presence, instead of edge or screw dislocations. In the next section, luminescent properties of GaN will be deeply discussed.

4.4 Optical characterization of GaN: Photoluminescence

Figure 4.7 shows PL spectra of GaN measured at 5 K using HeCd. The PL spectra exhibits prominent transitions at 3.492 eV with a couple of shoulders; one at a higher energy of 3.500 eV and another at lower energy of 3.486 eV. These three emission lines are identified as shallow neutral donor-bound (D_0X) exciton, free exciton A (FX_A) and free exciton B (FX_B) transitions. The donor bound-exciton (D_0X) and free exciton B is located $\sim 6 \text{ meV}$ below and $\sim 8 \text{ meV}$ above the free exciton (FX_A) energy (splitting between FX_A and FX_B), respectively. These values are in good agreement with [10] [11]. Alongside, 1-LO phonon replica of FX_B is also visible at 90 meV below it.

4.4.1 Temperature dependent PL

PL spectra for varying temperature from 5 to 100 K are shown in figure 4.8. The temperature dependence of photoluminescence of GaN shows a redshift in all the emission

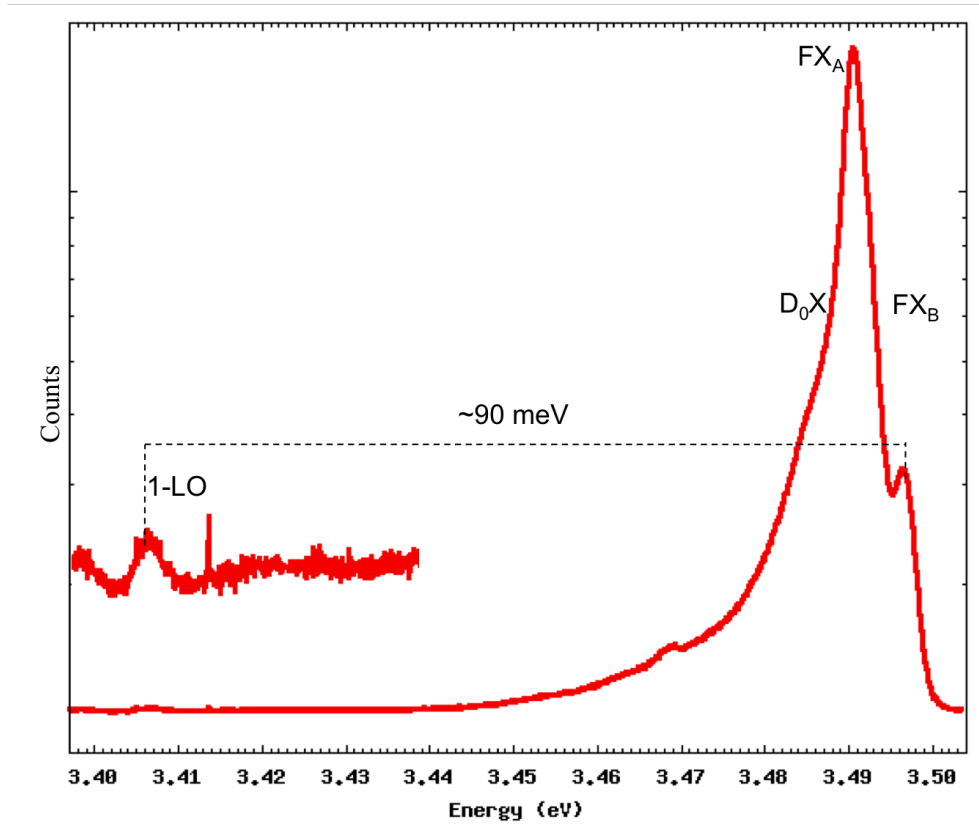


FIGURE 4.7: PL spectra of GaN on sapphire at 5K. Low energy side of the spectra is magnified to show the presence of 1-LO phonon replica of FX_B

lines, broadening of all emission lines and reduction in intensity (referred as thermal quenching) with increasing temperature. As shown in figure 4.9, the energy position of lines D_0X , FX_A and FX_B exhibit similar temperature dependence and the energy shift from 5 K and at 100 K observed here is 6.4 meV. This characteristic red-shift with increasing temperature is attributed to band gap reduction from lattice expansion and to electron-phonon interactions [12]. The temperature dependence of the linewidth is attributed to phonon-induced band broadening [13].

Figure 4.10 shows PL intensity variation of the main emission peaks (D_0X , FX_A and FX_B) as a function of temperature or the thermal quenching. As the temperature increases, universal reduction in PL intensity is observed, however, all the three emission lines exhibit a characteristic reduction in their intensity related to their different activation or binding energies. The shallow neutral donor-bound (D_0X) transition is extinguishes at 100 K, while free excitons A and B continue to exist. The temperature dependence of PL intensity can be given by the equation 4.6 for D_0X and FX_A , and equation 4.7 for FX_B (given below).

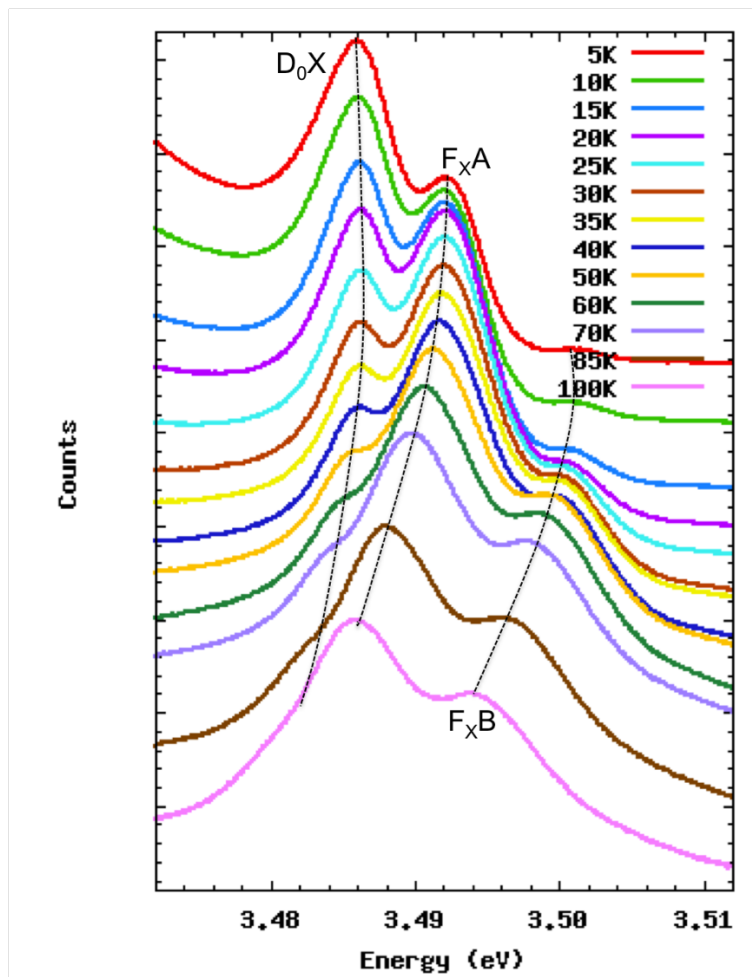
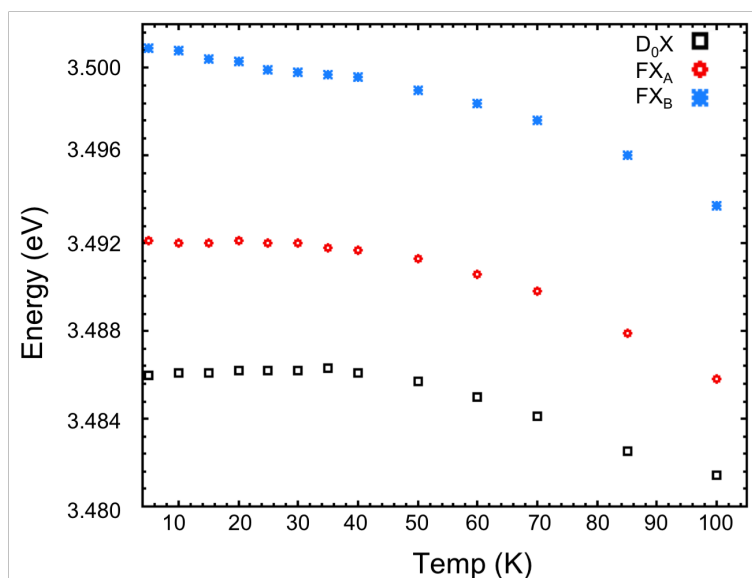


FIGURE 4.8: PL spectra of GaN at various temperature.

FIGURE 4.9: Temperature dependence of energy position of F_{XA} , F_{XB} , and D_0X in GaN substrate.

$$I(T) = \frac{I(0)}{1 + A_1 \exp(\frac{E_1}{kT}) + A_2 \exp(\frac{E_2}{kT})} \quad (4.6)$$

$$I(T) = \frac{I(0)}{1 + A \exp(\frac{E_1}{kT})} \quad (4.7)$$

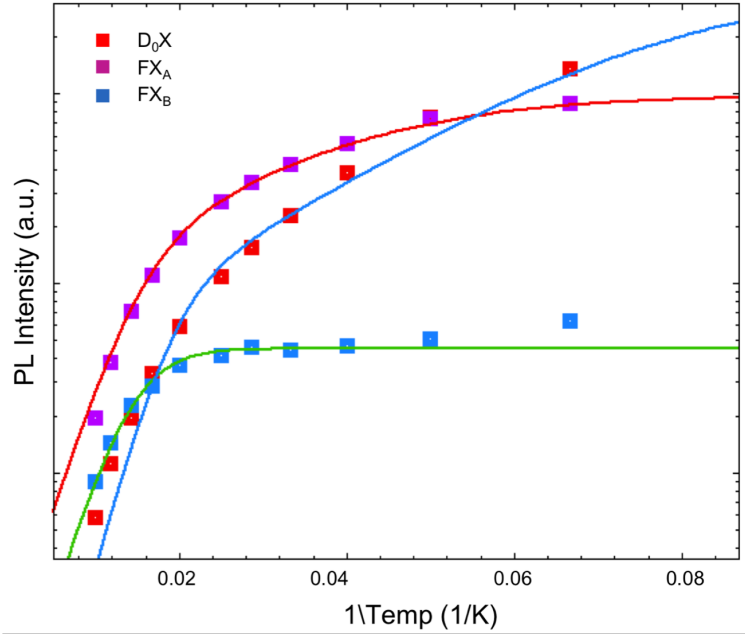


FIGURE 4.10: PL intensity of FX_A , FX_B , and D_0X in GaN substrate with varying temperature. The fit curves (solid line) were described by equation 4.6.

4.4.2 Thermal quenching of free excitons

Solid lines in figure 4.10 are the fit curves obtained from equations 4.6 and 4.7. The thermal quenching of the FX_A emission is fitted with two nonradiative processes with activation energies of ~ 6 meV and ~ 27.5 meV. The value of 6 meV (which is also the splitting between FX_A and FX_B) obtained clearly evident the transition of A exciton to B exciton [14]. This is further supported by the observation of an increase in PL intensity of FX_B below 25K (also visible in fig. 4.10 as data points above $0.04K^{-1}$), which is due consequent increase of the free exciton B population.

The activation energy for FX_B comes out to be same as that of the second activation energy (~ 27.5 meV) of FX_A , which is obtained at higher temperature. These are in good agreement with the other reports on the binding energies of the free excitons A,

B in strained GaN (1 to 3 μm) grown on sapphire. However, in unstrained GaN, the binding energies would shift to lower values by 1 to 2 meV [14] [15] [16] [17] [18].

4.4.3 Thermal quenching of donor bound excitons

Similarly to FX_A emission, two nonradiative processes would also describe the quenching of the donor-bound exciton D_0X emission. The activation energy of 5.3 meV obtained indicates the first process is due to thermal disintegration of shallow donor-exciton bound at low temperatures (below 25 K). This value is comparable to the difference between D_0X and FX_A emission lines (~ 6 meV). At higher temperature, activation energy of 32.3 meV is obtained for the second process. This value comes very close to the binding energies of the $SiGa$ (30.18 ± 0.1 meV) and O_N (33.2 ± 0.1 meV) donors [19], indicating it to be related to ionization of the donors. However, simultaneous exciton delocalization and exciton dissociation cannot be excluded [14] [20].

4.4.4 Conclusions

Advanced microscopy techniques such as scanning kelvin probe microscopy and conductive atomic force microscopy have been used to image surfaces of MOCVD grown GaN. Detailed analysis of the same area using both techniques allowed imaging and comparing both current map with localized current leakage paths associated with screw-dislocations and V-shape defects and surface potential variations originating from negatively charged threading dislocations and N-terminated surfaces of V-defects. Based on correlated topography, dislocation quantification and identification of edge and screw-components in dislocation, our results suggest that dislocations with edge component are negatively charged while screw dislocations and V-defects owing to their surface properties are responsible for the observed leakage paths.

The photoluminescence (PL) of GaN epitaxial layer was investigated for various temperatures from 5K to 100K. The PL of GaN capped with a thin epitaxial layer of $AlInN$ ($\sim 10\text{nm}$) clearly shows distinct free-exciton A, B and exciton A bound to neutral donors (D_0X) at 3.492 eV, 3.500 eV and 3.486 eV, respectively. Their binding energies are evaluated as ~ 6 meV for free exciton A at low temperature, ~ 27.5 meV at high temperature and ~ 27.5 meV for free exciton B. The possible non-radiative recombination processes of free and bound excitons occurring at various temperatures were also discussed.

Bibliography

- [1] M. Nonnenmacher, M. P. O'Boyle, and H. K. Wickramasinghe. *Appl. Phys. Lett.*, 58:2921, 1991.
- [2] B. S. Simpkins, D. M. Schaadt, E. T. Yu, and R. J. Molnar. *J. Appl. Phys.*, 91:9924, 2002.
- [3] K.Hirmatsu, K. Nishiyama, A. Motogaito, H. Miyake, Y. Iyechika, and T. Maeda. *phys. stat. sol. (a)*, 176:535, 1999.
- [4] U. Grossner, J. Furthmu ller, and F. Bechstedt. *phys. stat. sol. (b)*, 216:675, 1999.
- [5] A.L.Rosa and J. Neugebauer. *Physical Review B*, 73:205346, 2006.
- [6] A. Lochthofen, W. Mertin, G. Bacher, L. Hoepfel, S. Bader, J. Off, and B. Hahn. *Appl. Phys. Lett.*, 93:022107, 2008.
- [7] Z. Liliental-Weber, Y. Chen, S. Ruvimov, and J. Washburn. *Phys. Rev. Letts*, 79:2835, 1997.
- [8] J. M. Gibson, D. C. Joy, R. T. Tung, J. L. Ellison, C. Pimentel, and A. F. J. Levi. *Mat. Res. Soc. Symp. Proc.*, 56:163, 1986.
- [9] H.P.D. Schenk, P. Vennegues, O. Tottereau, T. Riemann, and J. Christen. *Journal of Crystal Growth*, 258:232, 2003.
- [10] D. Y. Song, M. Basavaraj, S. A. Nikishin, M. Holtz, V. Soukhoveev, A. Usikov, and V. Dmitriev. *J. Appl. Phys.*, 100:113504, 2006.
- [11] W. Shan W, T. J. Schmidt, X. H. Yang, S. J. Hwang, J. J. Song, and B. Goldenberg. *Appl. Phys. Lett.*, 66:985, 1995.
- [12] R. B. Capaz, C. D. Spataru, P. Tangney, M. L. Cohen, and S. G. Louie. *Phys. Rev. Lett.*, 94:036801, 2005.
- [13] S. Rudin, T. L. Reinecke, and B. Segall. *Phys. Rev. B*, 42:11218, 1990.

-
- [14] P. P. Paskov, T. Paskova, P. O. Holtz, and B. Monemar. *Phys. Rev. B*, 70:035210, 2004.
- [15] B. Monemar, J. P. Bergman, I. A. Buyanova, W. Li, H. Amano, and I. Akasaki. *Material Research Soc. Internet Journal of Nitride Semiconductor Research*, 1:2, 1996.
- [16] L. Eckey, J. Chr. Holst, A. Hoffmann, I. Broser, T. Detchprohm, and K. Hiramatsu. *Material Research Soc. Internet Journal of Nitride Semiconductor Research*, 2:1, 1997.
- [17] M. A. Reshchikov and H. Morkoc. *J. Appl. Phys.*, 97:061301, 2005.
- [18] A. V. Rodina, M. Dietrich, A. Goldner, L. Eckey, A. Hoffmann, A. L. Efros, M. Rosen, and B. K. Meyer B K. *Phys. Rev. B*, 64:115204, 2001.
- [19] W. J. Moore, J. A. Freitas, S. K. Lee, S. S. Park, and J. Y. Han. *Phys. Rev. B*, 65:081201, 2002.
- [20] M. Leroux, N. Grandjean, B. Beaumont, G. Nataf, J. Massies, and P. Gibart P. *J. Appl. Phys.*, 86:3721, 1999.

Chapter 5

AlGaInN/(AlN)/GaN

5.1 Structural properties

Seven samples of AlInN/AlN/GaN heterostructures were grown by AIXTRON metal organic chemical vapor deposition (MOCVD) on c-plane sapphire substrates. Here, the $3\ \mu\text{m}$ thick GaN buffer (unintentionally doped) layer or substrate was grown at $1050\ ^\circ\text{C}$ on sapphire using low temperature ($530\ ^\circ\text{C}$) GaN nucleation layer. The other two layers, the AlInN barrier layer and the AlN interlayer, were grown at $780\ ^\circ\text{C}$. The nominal thickness of the AlInN was kept constant as $\approx 15\ \text{nm}$ and that of AlN layer was varied, as shown in Table 6.2. Using high resolution X-ray diffraction (HR-XRD) measurements (figure 5.1) and by applying Vegard's law, indium percentage between 10% and 14% in AlInN [1] were estimated in these samples. The difference between the nominal and estimated indium percent is well presented in table 6.2. The eighth sample 3232 had a slight different growth condition. In this case, $3\ \mu\text{m}$ thick GaN layer was grown on 100 nm thick AlN buffer on sapphire and thickness of AlInN layer estimated was 33 nm. HRXRD measurements reveal an indium percentage of 13-14%.

5.2 Surface analysis

5.2.1 Topography

By AFM analysis, the average rms roughness varied between 0.3 and 0.5 nm in these samples on an area of $5\ \mu\text{m} \times 5\ \mu\text{m}$. Most of the samples were found to consist typically of grain-like features and V-pits. The average grain diameter calculated on it was around 120 nm. These grain-features are typical of MOCVD grown nitrides [2] and it is well known that the grain size depends on the growth conditions (gas flows, growth

TABLE 5.1: The nominal characteristics of the samples of AlInGaN/AlN/GaN.
 COURTESY: 1. XRD data marked with * by Dr. Duc Van Dinh, TUB Berlin, Germany
 2. Data marked ** are from Clemente et al. [1]

Sample	$AlInN$	$In(\%)$	AlN	GaN
3234	15	13.9** 11.0*	0	3
3236	15		0.5	3
3237	15	11.0*	1	3
3239	15		1.5	3
3238	15	11.0*	2	3
3233	15	13.9** 11.0*	2.5	3
3235	15	13.9**	7.5	3
3232	33	12.7*	1	3

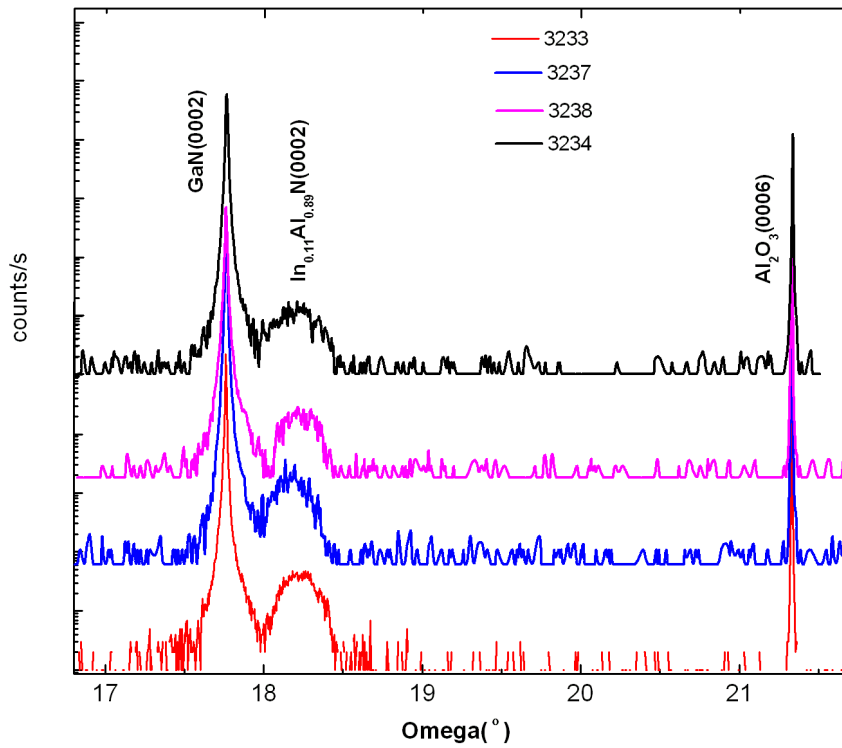


FIGURE 5.1: (0002) XRD rocking curves of sample 3234, 3237, 3238 and 3233. COURTESY: Dr. Duc Van Dinh, TUB Berlin, Germany

temperature etc.). Depending on the topography, the samples were distinguished into three types. Typical topography ($2 \mu m \times 2 \mu m$) for samples 3233, 3234, 3236, 3237, 3238 and 3239 is shown in figure 5.2(a). V-pit density in these samples was calculated in the range of 10^8 cm^{-2} . This is very typical of TD density present in GaN template, indicating their association with the TDs in GaN. Topography of sample 3235 with AlN thickness $\sim 7.5 \text{ nm}$ is shown in figure 5.2(b) and apart from high density of V-pits (10^{10} cm^{-2}), nano-sized cracks are also observed. In sample 3232 (see fig. 5.2(c)), apart from grains and V-pits (10^9 cm^{-2}) thread-shaped features were uniquely present on the surface.

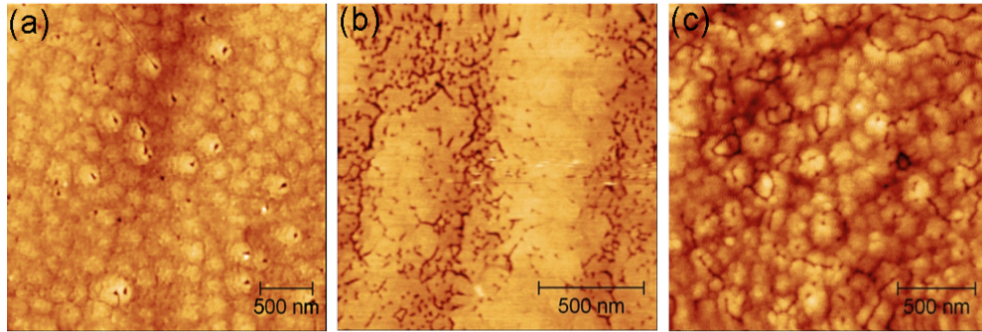


FIGURE 5.2: typical topographies of samples with (a) AlInN thickness 15 nm, AlN thickness between 0 and 2.5 nm (b) 15 nm AlInN, 7.5 nm AlN and (c) 33 nm AlInN, 1 nm AlN

The formation of pits on the grains and thread-like features were already observed [1] but not thoroughly investigated before. Thus, this thesis also aims towards studying their formation and electronic properties. Besides surface roughness Δ that plays a very important role in HEMTs, another important factor related to the topography is the autocorrelation length Λ , estimated by the one-dimensional height-height correlation function $H(r)$ [3],[4].

The one-dimensional height-height correlation function is defined by

$$H(r) = 2\Delta^2 \left[1 - \exp\left(-\frac{r}{\Lambda}\right) \right] \quad (5.1)$$

where r is the variable corresponding to the distance between two points on the surface and Δ , the roughness. The function $H(r)$ is directly obtained from the topography and Λ can be extracted by it using as the fitting parameter in equation 5.1. Autocorrelation correlation length calculated from the topography data of an area of $10 \times 10 \mu m^2$ in these samples was around 55 nm.

High-resolution topography maps were acquired by STM in the constant current mode at room temperature in ultra-high vacuum (UHV) conditions, by using an electrochemically-etched tungsten tip. Similarly, autocorrelation length was estimated to be around 2 nm for an area $120 \times 120 \text{ nm}^2$.

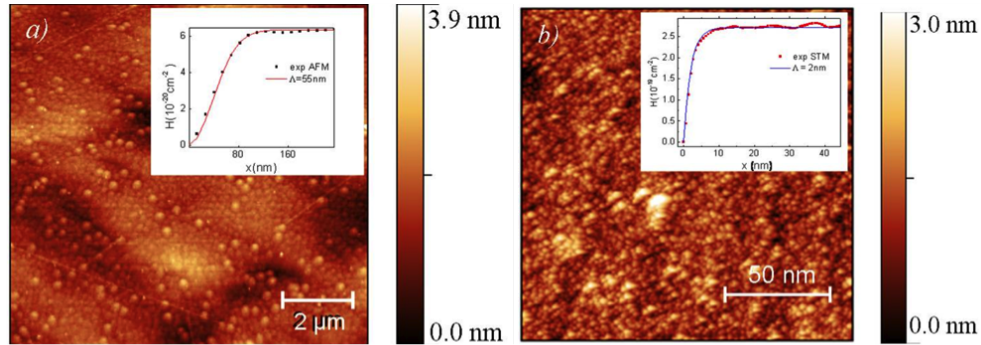


FIGURE 5.3: Typical topography maps of AlInN/AlN/GaN heterostructure with AlN layer thickness of 2 nm obtained by AFM (a) and STM (b). The fitting of the one-dimensional height-height correlation function H is also shown in the inset of (a) for the AFM line profile, and in the inset of (b) for the STM line profile.

5.2.2 Surface structure

During the growth or when a crystal is cleaved to expose a surface, the surface atoms are left with unsaturated chemical bonds. In an effort to reduce the density of these dangling bonds, the atoms in the top few layers rearrange, giving rise to a surface reconstruction. The ab-initio surface energy calculations for various surface structures have revealed that the stable surface reconstruction depends on the chemical potential of constituent atomic species. For instance in GaN, if it has a cation surface (Ga-terminated), each dangling bond is occupied with $3/4$ electrons and if it has anion surface (N-terminated), each dangling bond is occupied with $1/4$ electrons (figure 5.4). Although epitaxial growth is possible in both directions, experiments have shown that growth on (0001) is generally superior to $(000\bar{1})$ and in practice the (0001) GaN surface exhibits 1×1 , 2×2 , 4×4 , 5×5 and 6×4 surface unit cells, while in the case of GaN $(000\bar{1})$ 1×1 , 3×3 , 6×6 and 6×12 structures have been observed. The study of surface reconstruction is of significant importance from both a technological and fundamental point of view as any change in surface reconstruction may significantly change the device properties. For the development of devices, it is very essential to acquire a good understanding of the structural, electronic, and chemical properties of the surfaces.

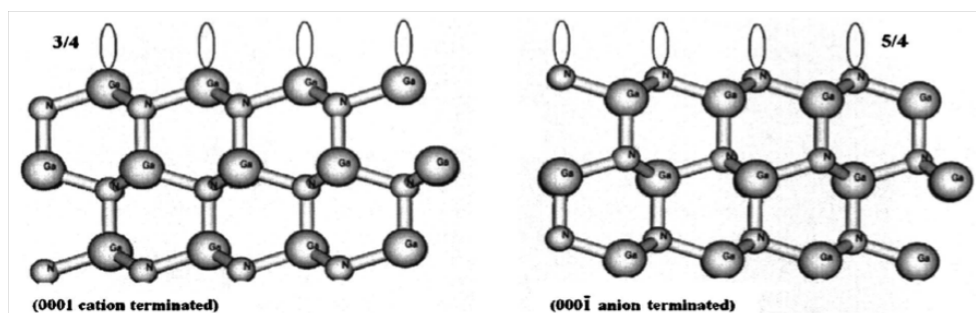


FIGURE 5.4: Atomic structures of wurtzite (0001) and (000 $\bar{1}$) GaN surfaces. The number indicates the nominal number of electrons per dangling bond. [5]

5.2.3 LEED

The surface crystallinity assessment was done by low energy electron diffraction (LEED). The annealing effect on the surface reconstruction of sample 3233 was studied. The unannealed sample showed a 1×1 surface and the subsequent annealing at $450^\circ C$, $550^\circ C$ and $650^\circ C$ indicated no new stable surface reconstruction. See figure 5.5. LEED images have shown 1×1 reconstruction typical for nitrides. This also indicates that there was no surface damage after annealing in these temperature ranges.

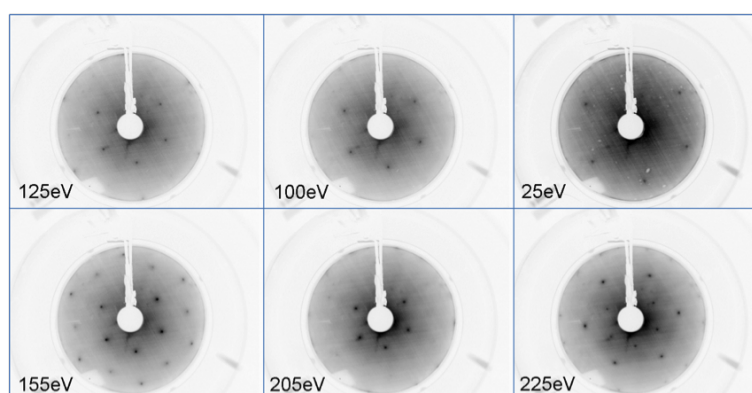


FIGURE 5.5: LEED image showing 1×1 surface reconstruction. COURTESY: D. Skuridina, TUB Berlin, Germany

5.2.4 XPS, AES: Ga incorporation

XPS spectra of 3233, 3234, 3238 and 3232 were measured at room temperature for varying photoemission angles (0 to 80°) i.e. the angle formed between the surface normal and the detector. In the XPS measurements, the samples were probed with a photon beam of energy $h\nu = 1486.9 \text{ eV}$ produced by a monochromatic anode $Al K\alpha$ x-ray source. XPS spectrum of sample 3232 is shown in figure. The spectrum shows the expected core levels related to $Al2s$, $Al2p$, $In3d$, $N1s$ along with contaminants/impurities

O1s and C1s but also the unexpected core levels Ga3s, Ga3p, Ga3d and GaLMM auger transition. The core levels of Ga cannot be related to GaN as the XPS signal appears mainly from the top 10 nm (maximum) of the layer and the estimated AlInN barrier layer is 15 nm. Similar evidence of Ga inclusion in AlInN was also observed in other samples.

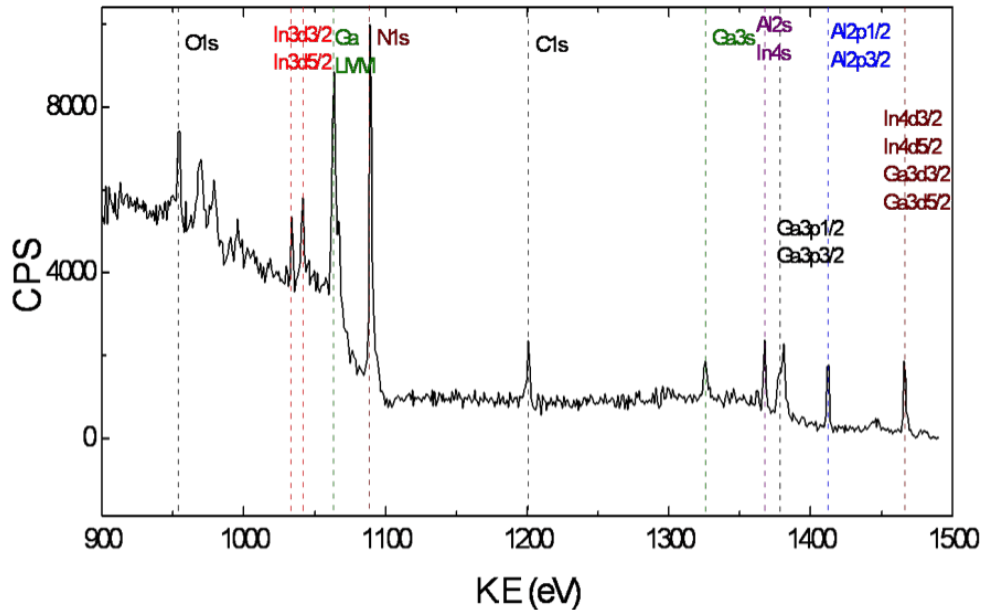


FIGURE 5.6: XPS spectrum of sample 3232 obtained at room temperature. Peaks related to Ga LMM, Ga3s and Ga3p are clear visible. COURTESY: D. Skuridina, TUB Berlin, Germany

5.2.5 Estimation of Ga

In $3d_{3/2}$, Al2s, N1s and Ga3s core level peaks were selected to estimate their percentage in the layer. It can be clearly seen in the spectrum that In4d overlaps with Ga3d, Al2p $_{1/2}$ with Al3p $_{1/2}$, this makes it difficult to use them for the estimation. However, in case of Al2s and In4s core levels that share a similar energy, the latter was neglected. From the previous XPS measurements on InN samples, In4s peak observed is very weak. So, we have assumed a significant contribution of Al2s, instead of In4s in the peak observed. However, any deviation from such an assumption could relatively change the percentage of Al and In. Table 5.2 shows the In, Al, Ga and N estimations in samples 3233, 3234, 3238 and 3232.

TABLE 5.2: Estimation of In, Al, Ga and N from XPS measurements. COURTESY: D. Skuridina, TUB Berlin, Germany

Sample	Temp	In	Al	Ga	N
Sample	K	%	%	%	%
3234	298	1.0	30.9	12.9	55.2
3238	298	0.7	28.5	13.6	57.2
3233	298	1.0	30.9	12.9	55.2
3232	298	3.3	30.4	12.6	53.8

TABLE 5.3: Estimated composition of sample 3233 from XPS at different emission angles. T is the annealed temperature.

T (°C)	In(%)	Al(%)	Ga(%)	N(%)
<i>emission angel = 0°</i>				
25	1	30.9	12.9	55.2
450	1	30.1	13.3	55.6
650	0.9	29.4	13.0	56.6
<i>emission angel = 44°</i>				
450	0.9	25.1	12.0	62
650	0.9	25.4	12.7	61

5.2.5.1 Determination of composition at the surface (Angle resolved XPS)

Apart from the surface structure, another factor that is very important is the surface composition. In case of GaN, growth properties or device properties can significantly change when they are N-terminated or Ga-terminated. The emission angle i.e. the angle between the surface normal and detector was varied for the samples from 0 ° to 80 °. In, Al, Ga and N% determined at different emission angles for samples 3233, 3234, 3238 are shown in tables 5.3, 5.4 and 5.5. One may see that the amount of Al and Ga in the region near surface for all samples shown here are very similar. However, percentage of indium in sample 3232 is almost three times of other samples (see fig. 5.7). As shown in fig. 5.7, decline of In, Ga and N with increment in emission angle in sample 3232, and the determination of 84% of Al from a depth of not more than 1 nm (at 80 ° emission angle) indicates that these surfaces are Al-terminated.

5.2.5.2 Gallium incorporation

The growth of AlInN with low Ga incorporation and high In concentration uniformity across the wafer seems to be difficult and might turn up to be a serious problem. Here, the unexpected Ga atoms in AlInN layer could be ascribed to (1) the decomposition

TABLE 5.4: Estimated composition of sample 3234 from XPS at different emission angles. T is the annealed temperature.

Temp ($^{\circ}\text{C}$)	<i>In</i> (%)	<i>Al</i> (%)	<i>Ga</i> (%)	<i>N</i> (%)
<i>emission angel = 0$^{\circ}$</i>				
25	0.9	30.1	14.4	54.6
<i>emission angel = 60$^{\circ}$</i>				
25	1.1	31.6	15.7	51.6

TABLE 5.5: Estimated composition of sample 3238 from XPS at different emission angles. T is the annealed temperature.

Temp ($^{\circ}\text{C}$)	<i>In</i> (%)	<i>Al</i> (%)	<i>Ga</i> (%)	<i>N</i> (%)
<i>emission angel = 0$^{\circ}$</i>				
25	0.7	28.5	13.6	57.2
550	0.7	28.2	11.8	59.3
<i>emission angel = 55$^{\circ}$</i>				
25	0.6	29.6	14.2	55.6

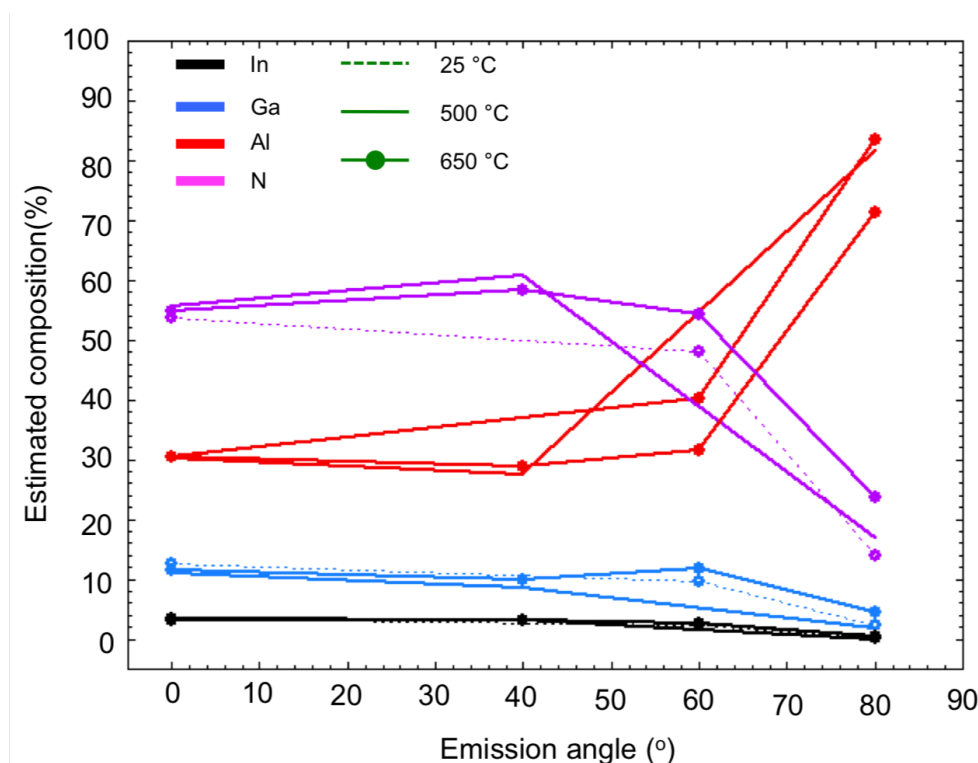


FIGURE 5.7: Composition determined in sample 3232 from XPS performed at different emission angles. [Courstey: D. Skuridina, TUB Berlin, Germany]

of GaN particles deposited on the inner wall of reactor, (2) the dissociation of residual TMGa in the gas distributing tubes and (3) the desorption of Ga from GaN template during the growth. Zhu et al. observed a large amount of Ga atoms, as high as 45% of the total group III constituents in MOCVD grown AlInN films, even when no Ga precursor was introduced. They attributed at most 2% Ga to residual Ga-contained sources in the reactor and speculated the rest to atom interdiffusion between In, Al, and Ga atoms. A high growth temperature and the H_2 added in carrier gas may enhance the Ga atom incorporation into AlIn(Ga)N epilayer by promoting decomposition of GaN template and increasing atom diffusing ability [6], [7].

5.3 Electrical characterization

5.3.1 Fermi-level determination by XPS

XPS was utilized to determine the separation of the surface Fermi level to the valence band maximum (VBM) for the InGaN alloys. The Fermi level position was calibrated using the Fermi edge of Molybdenum reference sample. Figure below shows the XPS spectra focusing on the valence band of sample 3233. The measurements were performed before and after the sample were annealed at $450^\circ C$ and $650^\circ C$. Fermi-level and valence band maximum was determined from the XPS spectra at the highest kinetic energies observed and then using the following relations

$$hv = K.E + B.E \quad (5.2)$$

where $hv = 1486.9 eV$ is the Al $k\alpha$ source and kinetic energy (K.E) is directly measured.

$$B.E = 1486.9 - K.E = E_f - E_v \quad (5.3)$$

$E_f - E_v$ in un-annealed sample was around 3.53 eV, which reduced to 3.23 eV and 3.08 eV after annealing at $450^\circ C$ and $650^\circ C$, respectively. Assuming the bandgap around $\approx 4.01 eV$, the Fermi-level at the surface is situated around 0.93 eV from the conduction band. During annealing, as O and C-impurities desorbs from the surface, native oxide present on the surface is eradicated.

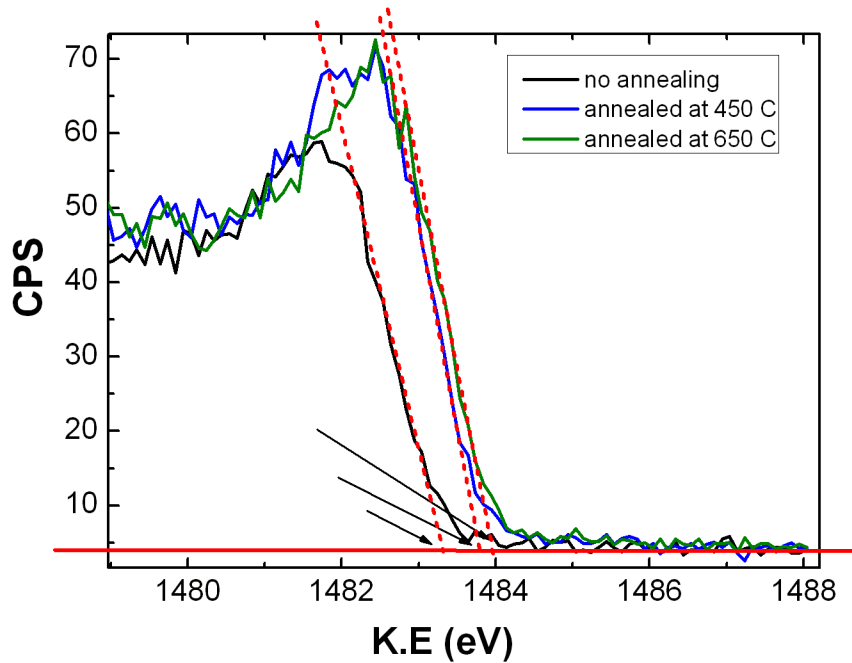


FIGURE 5.8: XPS spectra focusing on the valence band of sample 3233.

5.3.2 Local current transport

5.3.2.1 Nano-electrical characterization of defect free surface

Several transport mechanisms have been considered to be responsible for current voltage characteristics in III-nitrides based devices. Poole-Frenkel effect and electrical transport via dislocations could both play a major role as the high dislocation density (10^7 cm^{-2} to 10^9 cm^{-2}) [8] present in nitride based heterostructures is the dominant source of reverse bias leakage current in HEMT Schottky gate [9],[10],[11]. Tunnelling, thermionic emission, field emission or all of them could also explain current transport. This becomes complicated while dealing with heterostructures, as the current transport is no more explained only by phenomena occurring at the MS junction but the presence of heterojunctions could also significantly act in limiting the current. In order to study this, there was a need to perform I-V measurements on defect-free surface.

I-V characteristics were obtained by AFM (NT MDT- Solver PRO 47) by using conductive nano-needles (*Ag₂Ga*-Nanogneedles LLC, (see fig. 5.9) as AFM probe. The sample is grounded as shown in figure fig. 5.9(b). This contact was made with conductive silver on one of the sides of the sample piece. We also observed that there were no significant changes when the contact was made on the sample surface, except a shift in

the I-V curve. The I-V curves have been measured with the tip located at dislocation free areas and the measurements were systematically performed in many different areas, giving comparable results. All AFM based measurements were performed in ambient conditions.

The above-described mechanisms involving dislocations do not play an important role when the heterostructure is studied locally (i.e. area of few nm^2) because position of the AFM tip can be precisely controlled on a dislocation free region.

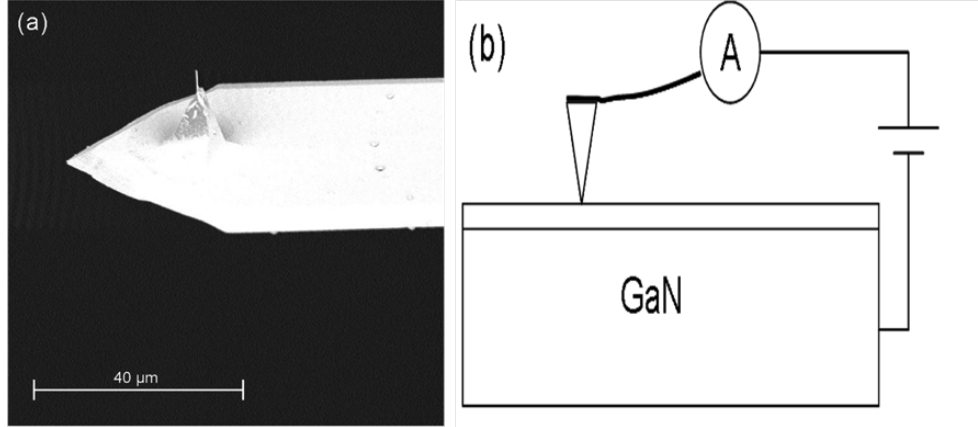


FIGURE 5.9: (a) SEM image of Ag_2Ga -Nauganeedles LLC (b) AFM tip-sample configuration for I-V measurements.

5.3.2.2 Model of the electrical transport

As mentioned before, I-V characteristics were obtained in forward bias, i.e. a varying positive bias is applied to the AFM-tip with respect to the sample. Therefore, the electrons will flow from the sample to the AFM-tip (we can neglect the hole current, as the main contribution to the current is given by the 2DEG). The band diagram of the system (metal- the tip- and the heterostructure), simulated by solving Schrödinger-Poisson equation, is shown in fig.5.10. The tip and the heterostructure form a Metal Semiconductor structure as the native oxide layer (likely containing (Al,Ga,In)-O complex) covering the sample in ambient condition does not play a significant role as the highly sharp and conductive tip can be considered to be in direct contact with the semiconductor. Also, its band gap could be significantly low (less than AlO_x) due to the inclusion of indium. Furthermore, presence of defects would prohibit it to act as a good insulator.

Assumptions: For the heterostructure band diagram modeling the following parameters were assumed: barrier height $\phi_b = 1.6 eV$ [12],[13], conduction band-offsets $\approx 1.4 eV$ and $\approx 0.4 eV$ using 70:30 ratio, polarization charge density $\sigma = 6 \times 10^{13} cm^{-2}$ [14]. These parameters were modified during the fitting and carefully checked for the values they

hold, which is a common procedure.

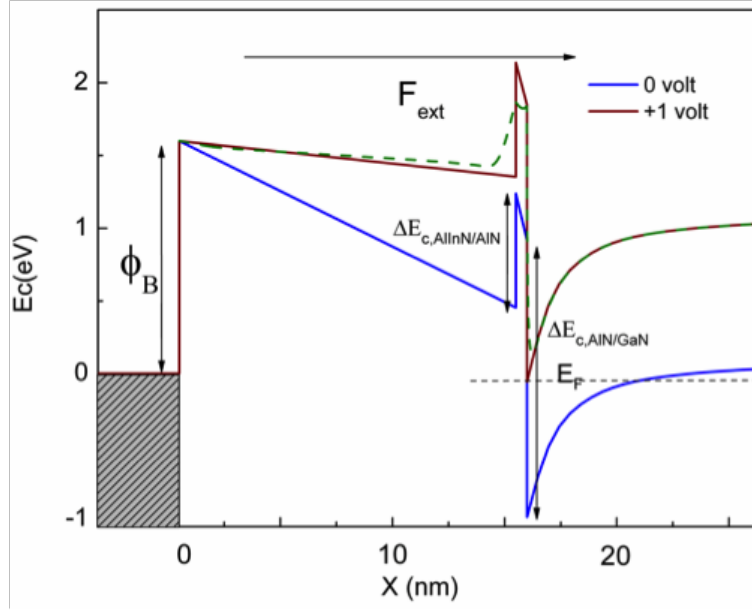


FIGURE 5.10: Equilibrium (blue, $V = 0$ V) and non equilibrium (brown, $V = 1$ V) band diagrams of the AlInGaN (15 nm)/AlN (1 nm)/GaN heterostructure obtained by self-consistently solving Schrödinger-Poisson equation for barrier height of 1.6 eV. The symbols are defined in the text. Here the dashed line shows the effect of image charge on band diagram.

Fig. 5.13 shows the measured I-V characteristics obtained for various samples with Ag_2Ga based nanoneedle AFM tip. Several conduction mechanisms could be invoked to understand the electrical transport at this junction and they will be discussed in the following. The first one is the thermionic emission over the barrier. We can consider as the possible conduction mechanisms in forward bias: emission of electrons (1) from the barrier layer (i.e. AlGaInN) into the metal contact (i.e. AFM tip), and (2) emission from the 2DEG region into the barrier layer (see fig. 2). The most general form of emission considered here is the thermionic emission (TE) and consequently, the current density for an applied bias $V > 3kT/q$ is given by:

$$I = I_0 \exp \left[\frac{q(V - IR_s)}{nkT} \right] \quad (5.4)$$

with $I_0 = A^* T^2 \exp\left(\frac{-q\phi_b}{kT}\right)$

where A^* is the Richardson's constant, ϕ_b the barrier height at the metal-/AlGaInN for the former case (1.6 eV) and ϕ_{2DEG} at the AlN/GaN interface for the latter case (defining $\phi_{2DEG} = \Delta E_{c,(Al,In)N/GaN} - E_0$, R_s the series resistance, ΔE_c the conduction

band offset between the interlayer and GaN or between the barrier and GaN (in the absence of interlayer). E_0 is the first subband energy for the 2DEG given by [14]

$$E_0 = \left[\frac{9\pi\hbar e^2 n_s}{8\varepsilon_s \text{sqrt} 8m^*} \right]^{2/3} \quad (5.5)$$

with n_s the 2DEG density, $\varepsilon = \varepsilon_0\varepsilon_s$ (ε_s - static permittivity) and m^* effective electron mass in GaN. One should note that AFM-tip/AlGaInN junction is in forward bias, while the electrical transport at AlN/2DEG junction is similar to the Metal Semiconductor junction in reverse bias. The obtained I-V can be explained either by process 1 or process 2. As shown in fig. 5.11, the current calculated through the thermionic emission (equation 5.4) does not account for the measured I-V characteristic.

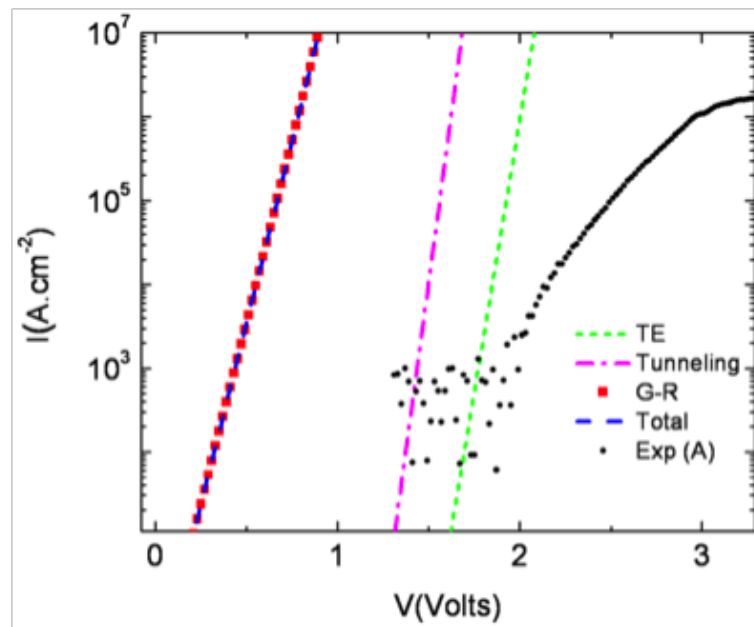


FIGURE 5.11: Measured current-voltage characteristics of sample A (solid circles) and calculated curves by theoretical models: thermionic emission (short dashed line), generation-recombination (solid squares) and tunneling (dash-dotted line). The total calculated current is also shown (dashed line).

The second transport mechanism that we will consider here is the tunneling of electrons through the insulating layer formed by the thin AlN layer and, eventually, the oxide. The tunneling probability in the form of direct tunneling (DT) or Fowler-Nordheim tunneling (FNT) through AlN layer could be moderate for the range of AlN varying between 0.5 nm and 2.5 nm. Experimentally, we observed that I-V curves for samples with varying AlN layer (from 0 to 2.5 nm) show similar behavior under the whole bias range up to a threshold voltage. This threshold voltage would be the value beyond which the 2DEG

is no more confined by the barrier height [15] and hence I-V curves deviate beyond this point. Moreover, the comparison between one experimental I-V curve has with the theoretical one calculated by the FNT model shows that that tunneling mechanisms via the AlN layer can be also ruled out (fig. 5.11). The total current flowing through the device can be given by the sum of all the contributions, if the generation-recombination current $I_{gen-rec}$ is considered [12], [13], [16], the total current becomes:

$$I_{TOT} = I_{thermionic} + I_{tunneling} + I_{gen-rec} \quad (5.6)$$

$$I_{gen-rec} = I_{gr} \exp \left[\frac{q(V - IR_s)}{2kT} \right] - 1 \quad (5.7)$$

where IR_s is the total voltage drop across the structure.

$I_{gr} = \frac{qn_i W_d}{2\tau}$, where n_i is the intrinsic carrier concentration, W_d is the depletion layer width and τ is the effective carrier lifetime.

$I_{tunneling} = CE^2 \exp \frac{-B}{E}$, where E is the electric field, C is the pre-exponential factor and B is the slope constant [17].

The comparison shown in figure 5.11 demonstrates that the total current estimated by equation 5.6 strongly overestimates the experimental one indicating the presence of another mechanism not occurring at the metal-AlGaInN junction which would act as a conduction bottleneck. This could occur at the GaN/barrier junction or GaN/interlayer junction. Thus, it is necessary to propose an alternative conduction mechanism.

The conduction mechanism here proposed is the thermionic emission through a Schottky barrier which is modified by the image force lowering, where the image force is produced by the 2DEG. The role of image charge in current transport at Schottky junction is well-known [18], while the image potential of a 2DEG region has been theoretically calculated [19] and its role in current-transport of 2DEG tunnel junction FET transistors has been investigated [20], but its role on current transport at the nanoscale has not been shown yet. Because of the high density of free carriers in the 2DEG channel, the 2DEG/AlGaInN interface could be considered as a pseudo-metal/semiconductor junction. Here, the effect of image charge at the interface AlN/GaN is the lowering of the barrier ($CBO - E_0$). It should be noted that, as the 2DEG density is function of the applied bias V [14], E_0 changes with the applied bias, too. If we consider the 2DEG at a

distance x_0 from the surface, one test electron with charge q at position x will experience a potential given by:

$$\phi(x) = -\frac{q}{r\epsilon_0\epsilon_d(|x| + |x_0|)} \quad (5.8)$$

The potential at the 2DEG channel, given by the net band bending close to the interface, can be approximated by $F \cdot x$, where F is the electric field (see fig 5.10). The total potential in the presence of image charges can thus be expressed as:

$$\phi_{TOT}(x) = -F \cdot x + \phi = -F \cdot x - \frac{q}{r\epsilon_0\epsilon_d(|x| + |x_0|)} \quad (5.9)$$

by equating $\frac{d\phi_{TOT}}{dx} = 0$, the position at which an electron will experience the maximum barrier lowering can be obtained

$$x_m = \sqrt{\frac{q}{4\epsilon_0\epsilon_d F}} - x_0 \quad (5.10)$$

It can be noted that the maximum total potential $\phi_{TOT}(x_m)$ comes out to be a function of F ,

$$\phi_{TOT}(x_m) = 2\sqrt{\frac{q}{r\epsilon_0\epsilon_d F}} + F \cdot x_0 \quad (5.11)$$

As the barrier lowering depends on F , F on n_{2D} and n_{2D} on V , the barrier lowering can be calculated as a function of the applied bias V . The relation between $n_{2D}(V)$ and F is derived from solving Poisson's equation

$$F = \frac{q \cdot (\sigma - n_{2D})}{\epsilon_0\epsilon_s} \quad (5.12)$$

Rewriting $(\sigma - n_{2D})$ as $f(n_{2D})$, net potential simplifies as

$$\phi_{TOT}(x_m) = 2.42 \times 10^{-9} [\sqrt{f(n_{2D})} + 1.44 \times f(n_{2D})x_0] \quad (5.13)$$

Here, units of ϕ , n_{2D} and x_0 are in volts, m^{-2} and m, respectively. Assuming that electron density in the second subband is negligible compared to that in the first subband, the electron density can be approximated in the electric quantum limit, by:

$$n_{2D} = \frac{m^* (E_F - E_0)}{\pi \hbar^2} \quad (5.14)$$

n_{2D} can be obtained as a function of the applied bias by solving the following electrostatic equation [14] :

$$\phi_b - F_{AlGaInN} d_{AlGaInN} + \Delta E_{C,AlGaInN/AlN} - F_{AlN} d_{AlN} + \Delta E_{C,AlN/GaN} + E_F = 0 \quad (5.15)$$

with $F_{AlGaInN}$, F_{AlN} polarization fields $d_{AlGaInN}$, d_{AlN} thickness in AlGaInN and AlN layer, respectively, and E_F is the fermi-level in GaN, that can be written as:

$$\left(\frac{9\pi \hbar e^2}{8\epsilon_0 \epsilon \sqrt{8m^*}} \right) n_{2D}^{2/3} + \left(\frac{\pi \hbar^2}{m^*} + \frac{e^2 t}{\epsilon} \right) n_{2D} + \left(e\phi_b - eV - \frac{e^2 t \sigma}{\epsilon} - \Delta E_{C,eff} \right) = 0 \quad (5.16)$$

where t is the total thickness and σ is the effective polarization constant.

This is numerically solved to obtain n_{2D} as a function of V (see fig. 5.12). Here we have approximated the relation between n_{2D} and V as linear. However, would change as a function of thickness of AlGaInN and AlN layers. The variation in thickness may arise from the inhomogeneous growth.

Taking into account the reduction in confinement due to image charge, we can modify current density in eq. 5.4 as

$$I = A^* T^2 \exp\left(-\frac{q\phi_{2DEG}}{kT}\right) \exp\left(-\frac{q\phi_{net}}{kT}\right), \quad (5.17)$$

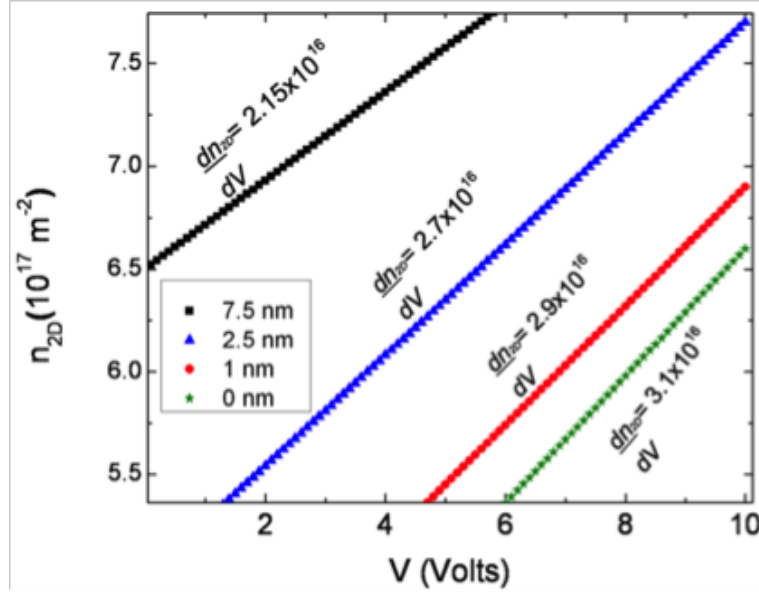


FIGURE 5.12: 2DEG density calculated from equation 5.16 as a function of applied bias for different thickness of AlN layer showing approximately a linear behavior. The slope $dn_{2D}/dV(m^{-2}/V)$ decreases as AlN thickness increases.

which further simplify as follows:

$$I = A \star T^2 \exp \left[-\frac{\Delta E_{C,2DEG} - E_0(V) - q\phi_{TOT}(V)}{kT} \right] \quad (5.18)$$

where ϕ_{TOT} is given by eq. 5.13 and n_{2D} is obtained by solving numerically equation 5.16.

5.3.2.3 Comparison of n_{2D} with Hall measurement data

In order to compare the proposed model with the I-V curves measured with the nano-tip, equations 5.16-5.18 have been applied to the present experimental condition. We have used $\Delta E_{C,AlGaInN/2DEG}$ and $\Delta E_{C,AlN/GaN}$ as 0.98 eV and 1.98 eV, respectively. Estimated value of E_0 is obtained by simulation for 13%-indium with boundary condition as ≈ 1.6 eV. Value of E_0 would vary from its calculated value due to inhomogeneity in indium-concentration (alloy disorder). As shown in figure 5.13, I-V characteristics obtained by AFM tip agree very well with the model expressed by equations 5.16-5.18. Alongside the range of values of key parameters (E_0 , ΔE_C etc) assumed, the 2DEG density value was used as the key fitting variable. We found a good agreement between the 2DEG density obtained in this manner and the values obtained with Hall Measurements (fig. 5.14), demonstrating the reliability of the proposed model. In addition, it could

be possible to extract, besides n_{2D} , other parameters such as ΔE_c and E_0 . The present comparison clearly demonstrates that the conduction mechanism observed in these heterostructures when contact area is few nm^2 , is assisted by image charge induced lowering of the potential barrier. This effect does not play a major role when the contact area is macroscopic, likely because of other dominant contributions, for example tunneling, dislocation-assisted conduction and generation-recombination currents.

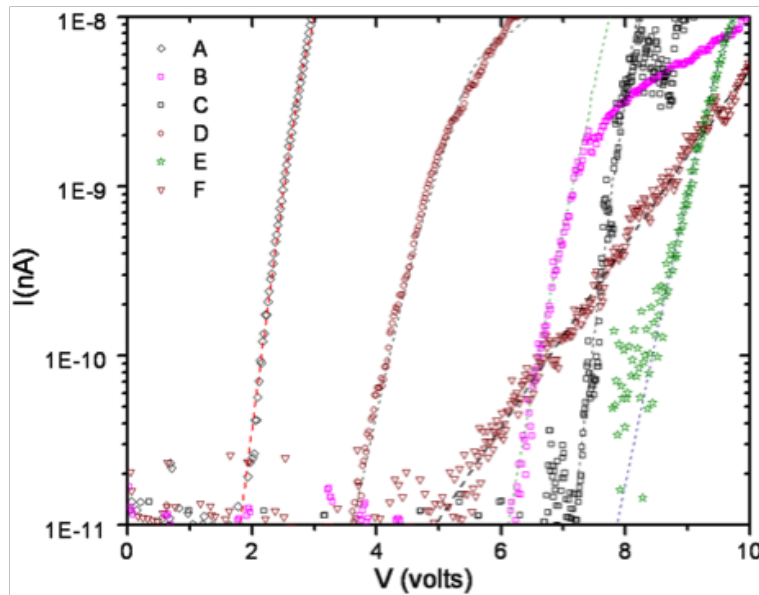


FIGURE 5.13: 2DEG density calculated from equation 5.16 as a function of applied bias for different thickness of AlN layer showing approximately a linear behavior. The slope $dn_{2D}/dV(m^{-2}/V)$ decreases as AlN thickness increases.

We have demonstrated that current- voltage measurements performed with conductive AFM tip on AlInGaN/AlN/GaN can be modeled by the thermionic emission from the 2DEG assisted by image charge induced barrier lowering. Other transport mechanisms that could be active in these heterostructures, such as tunneling or dislocation assisted conduction mechanisms have been ruled out due to the contact dimension (of the order of nanometer). The barrier lowering is caused by the image charge induced by the 2DEG and depends on the 2DEG characteristics. The 2DEG density (n_{2D}) and the first subband energy (E_0) can be thus be obtained by fitting the experimental data. The so obtained 2DEG density values have been found to be in very good agreement with the Hall measurements.

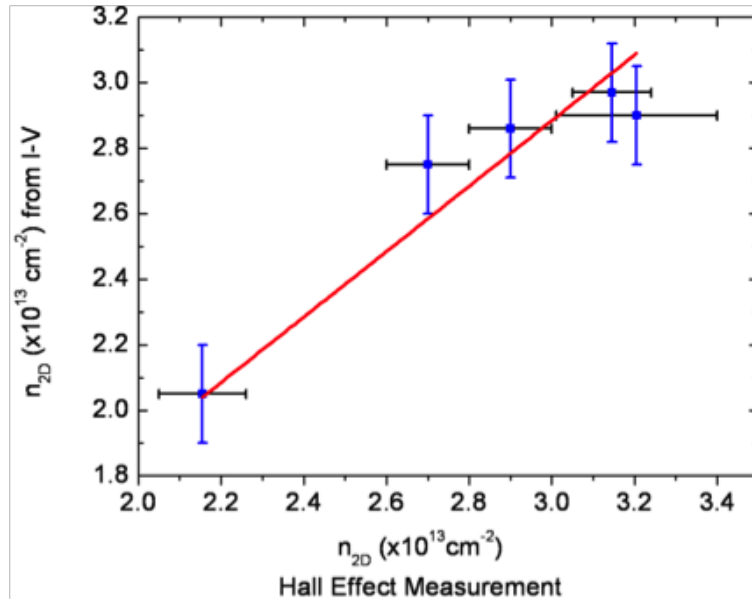


FIGURE 5.14: 2DEG density calculated from equation 5.16 as a function of applied bias for different thickness of AlN layer showing approximately a linear behavior. The slope dn_{2D}/dV (m^{-2}/V) decreases as AlN thickness increases.

5.4 Electrical characterization of extended defects

5.4.1 Threading dislocations

Figure 5.15a shows $1\mu m \times 1\mu m$ topography image and figure 5.15 b shows its corresponding phase-contrast image of sample 3232. As already stated before and also seen in the topography, the sample consisted of V-pits and thread-like features. The thread-like features may appear due to a series of V-pits in proximity below the resolution of AFM and also could be attributed to tilts and twist boundaries. In Figure 5.15b, there is a sharp contrast around these features that clearly distinguish them from their boundaries. The phase contrast image is directly related to the compositional contrast on the surface [3] [4]. Figure 5.15(c) shows phase-profile corresponding to a height-profile across a thread-like feature (focused in Fig 5.15a, b). It shows a strong shift in the phase from a negative value (at the edges of the feature) to a positive value (at the center). The positive and negative value of phase is defined by conservative and dissipative force of interaction between AFM tip and surface molecules, respectively.

In order to analyze the electrical properties of pits and channels, current-AFM and STM was used. Figure 5.16a and 5.16b shows the topography and its respective current-map as obtained by conductive-AFM using a Pt/Ir coated silicon tip. To avoid artifacts due to wearing of Pt-coating on silicon tip during scanning, conductive-diamond tip and conductive-nano needles [21] were also used to confirm the measurements. AFM

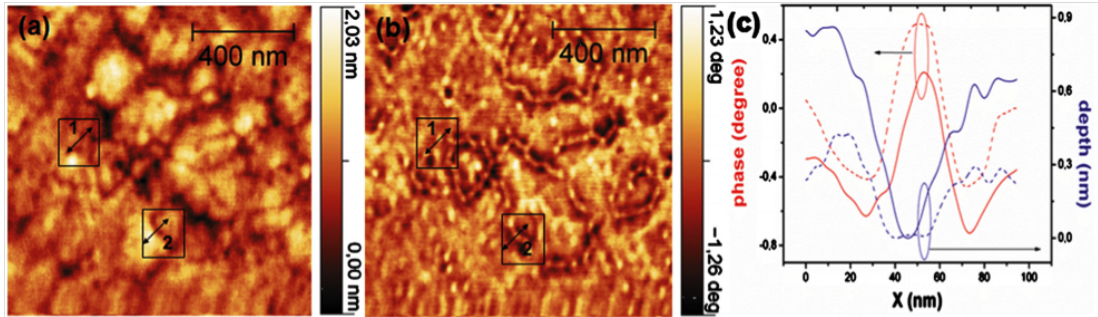


FIGURE 5.15: (a) Topography image of AlGaInN surface obtained in semi-contact mode. Pit is marked as 1 and channel is marked as 2. (b) Phase-contrast image of AlGaInN surface corresponding to (a) showing phase-contrast change around pits and thread-like features. There is dark contrast around the edges of thread-like features and pits whereas bright-contrast in their interior. (c) (Color online) Depth-profile (blue-curve) and the corresponding phase-contrast profile (red-curve) across a channel and a pit marked in (a) and (b) Solid-line and dashed-line indicates channel and pit, respectively.

probe was biased with 10 volts and scanned over the surface in contact-mode. It can be observed from the comparison of topography with the current map (see Fig. 5.16(c)) that the regions corresponding to pits and channels are more conductive than other regions.

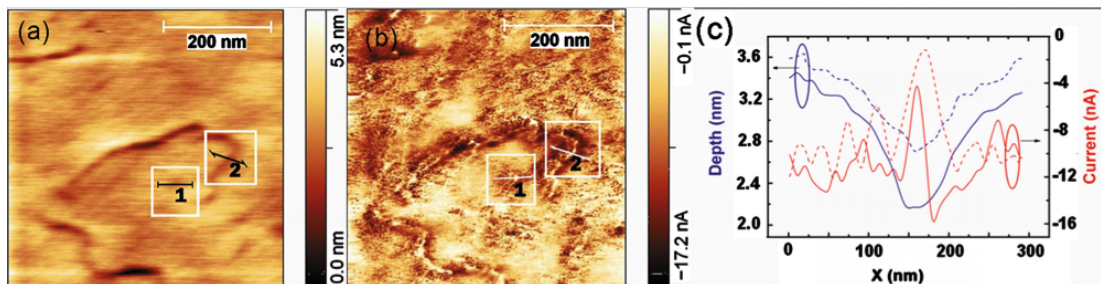


FIGURE 5.16: (a) Topography image of AlGaInN surface obtained in contact mode focusing on V-defects (marked as 1) and channels (marked as 2) in its insets. (b) Current-map of AlGaInN surface corresponding to (a) showing the presence of high conductivity along the edges of channel and pit. Bias voltage = 10V. (c) (Color online) Depth-profile (blue-curve) and the corresponding current-profile (red-curve) across a channel and a pit marked in (a) and (b) Solid-line and dashed-line indicates channel and pit, respectively.

The presence of pits and channels are evident in AlGaInN/AlN/GaN surface. From phase-contrast images and current-maps, we determined that the characteristics of these features are associated with the inhomogeneity or compositional variation present around them. But the absence of channels in samples with lower thickness of AlGaInN barrier layer (15 nm) suggests that by optimizing the thickness of AlGaInN layer to a lower value would be an effective way to prevent such inhomogeneity without affecting the 2DEG density.

The emergence of these pits with similar structure, already observed in AlGaInN [22] and in AlInN [23], on the grain-like structures is explained as the formation of V-defects on AlInN surface. These V-defects arise from the termination of highly strained threading dislocations at the surface in order to reduce their stress. It has been shown that V-defects have pyramidal shape comprising of six $\{1011\}$ sidewall facets [23]. TEM image in figure 5.17 shows termination of a threading dislocation from GaN substrate with a V-pit in the barrier layer.

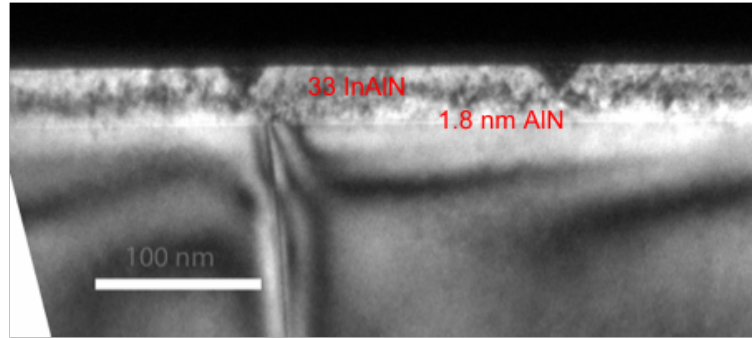


FIGURE 5.17: TEM cross-sectional view of sample 3232 showing the termination of a threading dislocation arising in GaN at the surface of barrier layer in the form of V-pit.

During the stabilization (strain relaxation) of V-defects, In-atoms migrate in such a way that stronger Al-N bonds from the regions nearby in AlInN matrix replace weaker In-N bonds in the bulk of V-defects [23], [24]. As a result, In-atoms segregate at the edges and the surrounding regions like surface of the sidewalls of the V-defects reconstruct to form Al-rich regions. In the case of quaternary alloy AlGaInN too, this should be true, however, presence of high amount of Ga in the matrix would cause segregation of both of Ga and In-atoms. As already mentioned, phase contrast image is directly related to the compositional contrast on the surface, therefore Al-rich regions and Ga/In-segregated regions, also observed in [23], could explain the bright-contrast and dark-contrast around V-defects respectively (V-defect and its edges in Fig. 5.15(b)). Similar effect can also be explained around channels where high-Al content resides on the channels and In-atoms on its edges.

Scanning tunneling spectroscopy (STS) measurements were performed on this sample and they also suggested the presence of inhomogeneity around the dislocations. Primarily, I-V behavior in STS is due to the tunneling of electrons from occupied states to unoccupied states. If the sample is positively biased with respect to the tip (grounded), the tunneling current occurs when the Fermi level of the tip (filled states) is above the conduction band edge of the sample surface (unfilled states). Similarly, if the sample is negatively biased, tunneling current occurs when the valence band edge of the sample

surface (filled states) is above the Fermi level of the tip (unfilled states). This summarizes for the tunneling current observed for the energies ($eV_f > E_{F,m} - E_{CBM}$ and $eV_r < E_{VBM} - E_{F,m}$) outside the forbidden gap E_g . However, for tunneling biases corresponding to energies within the E_g , observation of current could occur if (i) intrinsic surface states exist in the band gap and/or (ii) defects are present at the surface.

Figure 5.18a shows the $50 \times 50 \text{ nm}^2$ STM image of sample 3232. It comprises two V-defects marked in region 1 and region 2 (dashed box). Along with regions of V-defects, STM measurements were also performed in a defect-free region (marked as 3) to verify if there exist a difference in density of states in two different regions. Normalized differential conductivity $(dI/dV)/(I/V)$ measured against sample bias V for dislocation free region and at the V-defects is shown in fig. 5.18b. One may see that for dislocation-free region (°3), no substantial differential conductivity can be seen below -2.26 volts in the reverse bias. However, for regions 1 and 2 consisting of V-defect, significant differential conductivity between -1 V and -2 V is observed forming a peak around -1.4 volts. Thus, it is very clear that inhomogeneity exists around the V-defects. A possible explanation would be formation of metal-rich region around the dislocations.

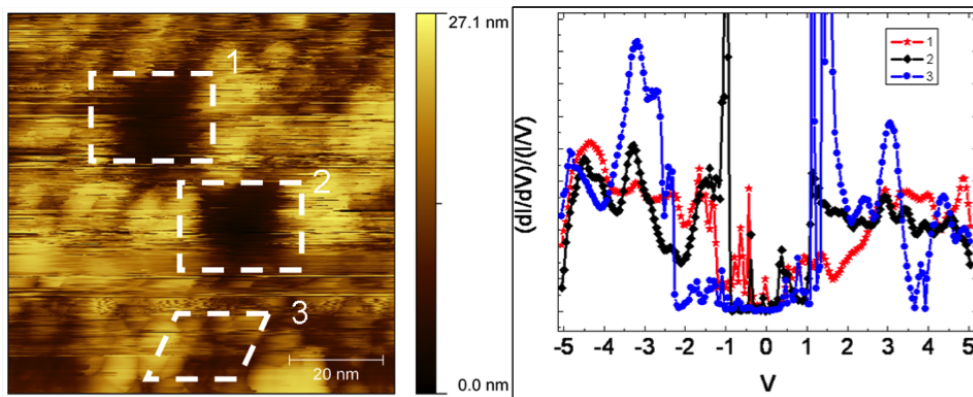


FIGURE 5.18: (a) shows STM image of $50 \text{ nm} \times 50 \text{ nm}$ area of sample 3232. The two dislocations are marked (dashed box) in regions 1 and 2 and a dislocation free region is marked as 3. (b) is the average $(dI/dV)/(I/V)$ against bias in region 1, 2 and 3. The function $(dI/dV)/(I/V)$ roughly represents the density of states.

From channels and V-defects as shown by C-AFM analysis (Fig. 5.16) it emerges that edges of channels and V-defects (In-rich) are more conductive while interior of V-defects and channels themselves (Al-rich regions) are less conductive. Presence of AlO_x layer explains low conductivity in Al-rich regions. AlO_x layer would act as a barrier/insulator for electron-conduction and lowers the conductivity. Presence of such conductive channels and V-defects would facilitate high gate leakage current in AlGaInN/GaN heterostructure based HEMT devices.

Apart from the threading dislocations and/or V-defects, another kind of extended defects that are formed in heterostructures are cracks. Because of the nano-size dimensions of the cracks observed in the samples studied, we have used the terminology *nanocracks*. The next section focuses on the origin of nanocracks and their possible effect on a Schottky diode characteristics.

5.4.2 Formation of nanocracks

AlGaIn/GaN heterostructures are widely used in HEMT devices due to the presence of strong spontaneous and piezoelectric polarization fields that cause the formation of high two-dimensional electron gas (2DEG) density ($1 \times 10^{13} \text{cm}^{-2}$) [25]. However, AlGaIn/GaN heterostructures are strongly lattice-mismatched, especially at high Al-content. Recently, lattice-matched AlInN/GaN heterostructures have been investigated in view of their potential application to HEMT devices [26]. In AlInN/GaN the strong spontaneous polarization field induces a 2DEG electron density reaching up to $2.4 \times 10^{13} \text{cm}^{-2}$ [26]. Nevertheless, the alloy-disorder effect in the AlInN barrier layer prevents such structure from achieving a high mobility in the channel. In order to reduce alloy-disorder effect, the insertion of an AlN layer between AlInN and GaN is often used [26], [27]. The idea of using AlN as an insertion layer was drawn from its use in AlGaIn/GaN heterostructures, where it was introduced to grow crack-free thick AlGaIn layers [27]. In that case it was found that the introduction of a relaxed AlN thin film (i.e., with thickness beyond its critical value) causes compressive strain in the AlGaIn layer, thus, preventing it from cracking. Moreover, crack propagation from the AlN interlayer into the AlGaIn layer was not observed.

In lattice-matched AlInN, there is an additional advantage, as the higher conduction band offset due to presence of the AlN layer provides a better electron confinement [28]. It was shown that electron mobility and 2DEG concentration vary with the thickness of AlN layer [29], [30], both increasing for higher AlN thickness. As crack formation was only observed in sample 3235, even though the barrier layer AlGaInN composition is almost identical to other samples, this strongly suggests that crack formation is induced by the interlayer AlN.

When AlN is grown over GaN (0001), it is under tensile strain. Its critical thickness reported for strain relaxation is around 6.5 nm [28]. It is known that beyond the critical thickness strain in AlN layer would be released non-pseudomorphically by crack formation and generation of threading dislocations (TDs). However, in the case of sandwich structure of AlN between GaN and AlGaInN layer as ours, cracking mechanism may take

place for thickness lower than 6.5 nm because of the additional tensile strain induced by AlGaInN layer. As a result, we have observed crack-formation and high density of V-pits (around 10^{10} cm^{-2}) in AlGaInN barrier layers. Cross-section view of this sample is shown in figure 5.19. It clearly shows nano-cracks and pits originating amid AlN interlayer.

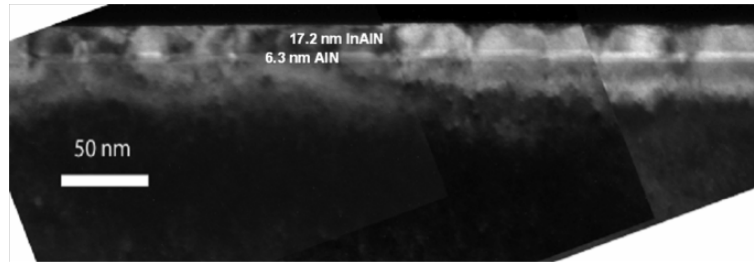


FIGURE 5.19: TEM cross-sectional view of sample 3235 showing formation of nano-cracks and V-pits amid AlN interlayer [COURTSEY:Arantxa, Caen]

In this work, we have studied the role of relaxed AlN interlayer in AlGaInN/-AlN/GaN heterostructures in terms of crack propagation and additional threading dislocations into the barrier layer, together with the effect that the AlN interlayer plays on the electrical properties.

Conductivity maps at the nanoscale have been obtained using *Ag₂Ga* nano-needle (Nauga nano-needles) as AFM tip [21]. The contact area formed between AFM tip and sample surface was around $5 - 10 \text{ nm}^2$. The ohmic and Schottky contacts have been prepared by evaporating Ti/Al/Ni/Au metals (annealed at 850°C for 30 s in N_2 ambient) and Ni/Au metals (circular Schottky contacts - 1mm diameter), respectively, for current-voltage characterization.

We have observed that cracks are not uniformly distributed over the surface. Non-uniformity of the AlN layer thickness could be the possible reason for the observed inhomogeneous distribution of the crack density. Micro-cracks (from few μm to few 100 μm) have been already reported in literature [31], [32], but the nano-cracks investigated in the present work are significantly smaller in size. In our sample 3235, cracks are at most 150 nm long and 15-50 nm wide.

Phase-contrast mode (semi-contact AFM) and C-AFM have been useful in the detection of metal (Ga, In) segregation at TDs [33]. During the growth of AlGaInN on the AlN layer with crack channels, segregation of Ga/In-adatoms around the edges of crack tips is energetically favored, because low coordination sites and are preferentially occupied by the weaker Ga-N and In-N bonds rather than by the stronger Al-N bonds [23]. This

would result in the formation of gallium/indium-rich path between the surface and the AlGaInN/AlN interface at the crack as AlInN layer grows. Figure 5.20(b) is a $1 \times 1 \mu\text{m}^2$ current AFM map obtained with a bias voltage of 3.5 V on this sample, with the dark regions corresponding to higher currents. This clearly shows that the edges of the crack channels (dark-contrast) are more conductive than the other regions. 5.21(a) shows the topography and figure 5.21(b) shows the phase-contrast map obtained simultaneously in semi-contact mode AFM. In the latter figure, a strong contrast occurs at the crack-edges, which is related to changes in composition or strain energy [3], [4]. Since, migration of Ga/In-adatoms is governed by strain-energy [23], [24], this contrast would also depict the compositional variation near the crack edges. As described above, this could be associated to Ga/In-adatoms concentrating along the edges of cracks, leading to the formation of conductive paths between the surface and the 2DEG. Therefore, we can ascribe the dark contrast observed at these regions, both in phase-images and in current-maps, to the presence of metal-rich region.

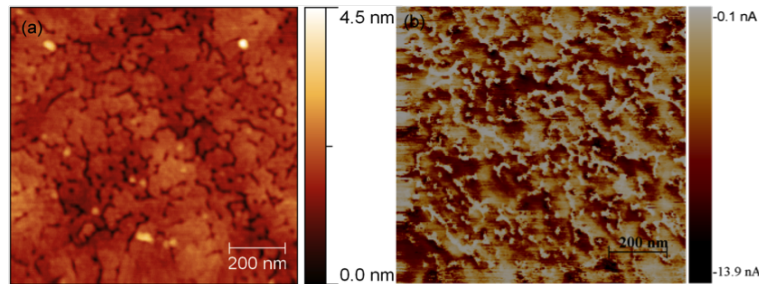


FIGURE 5.20: Topography image (semi-contact) of sample with AlN thickness = 7.5 nm showing cracks. (b) Current map of the same sample but in an area different from (a). Dark-contrast regions indicate high current/In-rich regions.

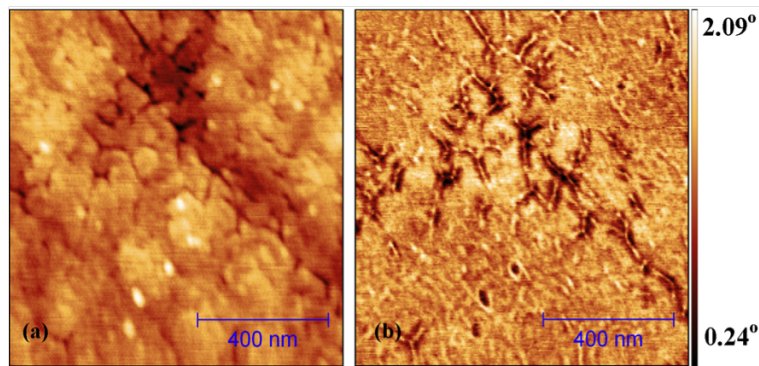


FIGURE 5.21: topography image (semi-contact mode AFM) of sample with AlN thickness = 7.5 nm showing cracks, and (b) corresponding phase-image. Dark-contrast regions are associated to In-segregation.

I-V characteristics obtained with AFM probe at the cracks, figure 5.22(a), show a significant increase in the current with increasing applied bias, almost symmetric in forward bias and reverse bias. This indicates that cracks act as shunts between the surface and

the 2DEG even at low voltages, hence providing a conductive electrical path. On the contrary, I-V at a crack-free surface shows the conduction onset in forward bias only at voltages larger than 7 volts.

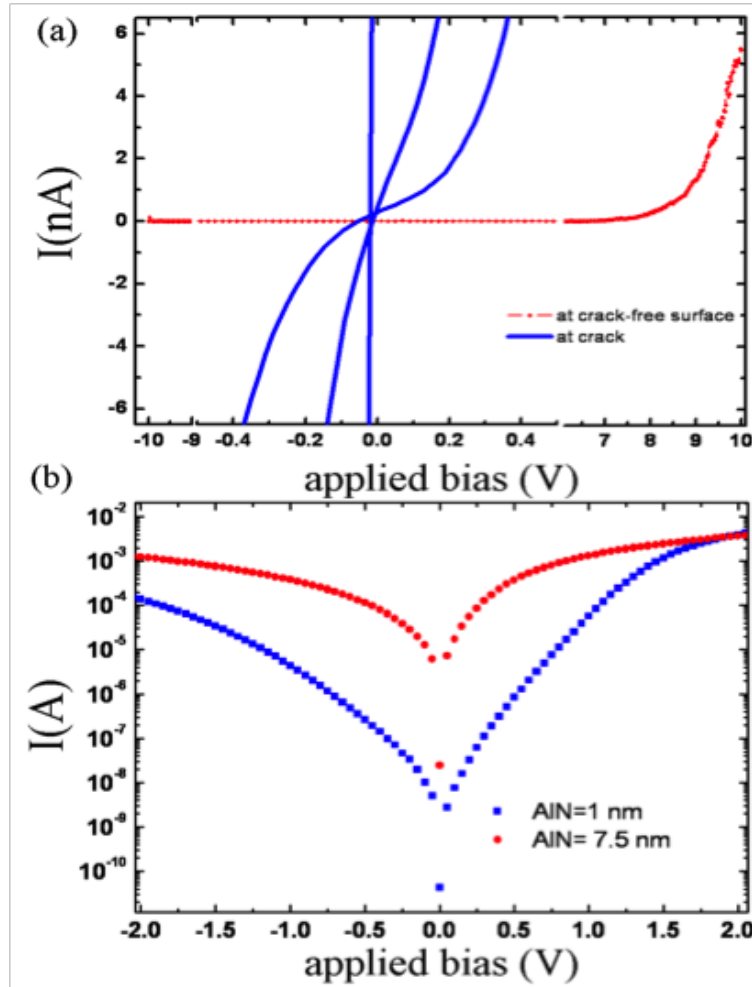


FIGURE 5.22: (a) Microscopic current-voltage characteristics obtained with the AFM-probe at the cracks and on a crack-free surface of AlGaInN/AlN (7.5 nm)/GaN heterostructures. (b) Macroscopic current-voltage characteristics of Ni/Au Schottky contacts on AlGaInN/AlN/GaN heterostructures with AlN layers of 7.5 nm and 1 nm.

Figure 5.22(b) shows the comparison between room temperature I-V curves of Ni/Au Schottky contacts on AlGaInN/AlN/GaN heterostructures with AlN thickness of 7.5 nm and of 1 nm. The leakage current density for the 7.5 nm thick AlN layers is $0.157 \text{ A} \cdot \text{cm}^{-2}$ at a reverse bias of 2 V, which is almost one order of magnitude higher than for samples with 1 nm thick AlN layers ($0.017 \text{ A} \cdot \text{cm}^{-2}$). It is noteworthy that the presence of the cracked 7.5 nm thick AlN layer induces a marked degradation of the rectifying properties of the Schottky contacts ($I_{ForwardBias}/I_{ReverseBias}$ at $V=+2\text{V} = 2.96$), leading to an almost ohmic behavior. This effect could be associated to the presence of electrically active nano cracks and to a high density of V-defects. These results, dealing with the

macroscopic electrical behavior, well correlate with what we observed at microscopic level from I-V obtained with AFM probe at the cracks, shown in 5.22 4(a).

As reported in [15], Hall measurements demonstrate for the sample with 7.5nm thick non-pseudomorphic AlN layer a lower 2DEG concentration ($2 \times 10^{13} \text{cm}^{-2}$) and a lower mobility ($300 \text{cm}^{-2}\text{V}^{-1}\text{s}^{-1}$) than those samples with a pseudomorphically grown AlN interlayer (described in previous chapter and in [15]). These results in terms of 2DEG density differ from those calculated for pseudomorphic AlN with 7.0 nm or more (for thickness more than critical thickness of AlN), where high sheet carrier concentration is hypothesized [28]. To understand the effect of these structural defects formation that includes both nanocracks and threading dislocations, the non-pseudomorphic AlN layer (7.5 nm) grown over GaN can be roughly modeled as a layer with local thickness fluctuations, reducing to 0 nm as the worst case. As we know, the sheet carrier concentration is a function of the barrier height, of the band-offset and of the barrier and interlayer thickness [14]. Because of the possibility of low quality of MOCVD grown AlN (as they were grown at a low temperature, $T = 750^\circ\text{C}$) in terms of its surface roughness, local fluctuations in thickness can be expected. However, still local fluctuations in AlN thickness cannot explain the observed lowering of sheet carrier concentration because high 2DEG density was observed in all the samples with varying AlN thickness from 0 to 2.5 nm. On the other hand, the presence of high gallium and indium segregation at these defects would cause local reduction in polarization fields, in barrier height and in band-gap and this would explain the observed low 2DEG electron density. In order to understand the low mobility values, scattering mechanisms need also to be accounted for. Scattering due to structural defects (such as cracks or high density of dislocations) [34] and alloy disorder [29] in ternary alloys stand as the dominating candidates for the cause of low mobility.

In conclusion, AFM analyses carried out in semi-contact and conductive mode allowed for the identification and characterization of nano-cracks in AlGaInN/AlN/GaN heterostructures. We have here assessed that this propagation is associated with metal segregation. Current-Voltage characteristics show that the nanocracks are electrically conductive, induce very high leakage current and strongly affect the rectifying behavior of Schottky contacts fabricated on AlGaInN layer.

Up to now, we have explained the effect of 2DEG on the current transport paths. In the next section, the impact of 2DEG on luminescence properties will be discussed.

5.5 Optical characterization: PL

PL spectra of AlGaInN/GaN and AlGaInN/AlN/GaN with varying AlN thickness were acquired (see figure 5.23). As shown here, the spectra is dominated with recombination transitions typical of bulk-GaN such as the ones related to donor bound excitons (D_0X), free exciton A (FX_A) and free exciton B (FX_B). D_0X recombination dominates at lower temperature ($T < 20K$) and FX_A recombination at higher temperatures (see also Chapter 4). Other than the commonly known emissions in GaN, a new band at 3.464 eV at 5K, which is ~ 22 meV below the GaN donor bound exciton emission peak, was observed in sample 3232. This emission does not shift but quenches rapidly with increasing temperature, almost disappearing at $\sim 50K$. When compared with samples with different AlN thicknesses (3234, 3237, 3238 and 3233), the peak position of this new emission shows a strong dependence on AlN and AlGaInN thickness, hence, either a red or blue-shifts are observed (fig. 5.24). Since its temperature dependence is the same in all the samples, we can ascribe its origin to the same cause. We attribute this band to the recombination of electrons confined in the 2DEG region near AlGaInN/GaN or AlN/GaN interface and photo-generated holes in the valence band edge of GaN. This phenomenon has already been observed in AlGaAs/GaAs, AlGaIn/GaN and AlInN/GaN heterostructures [35] [36] [37] [38] and the band is often referred to as H-band [39].

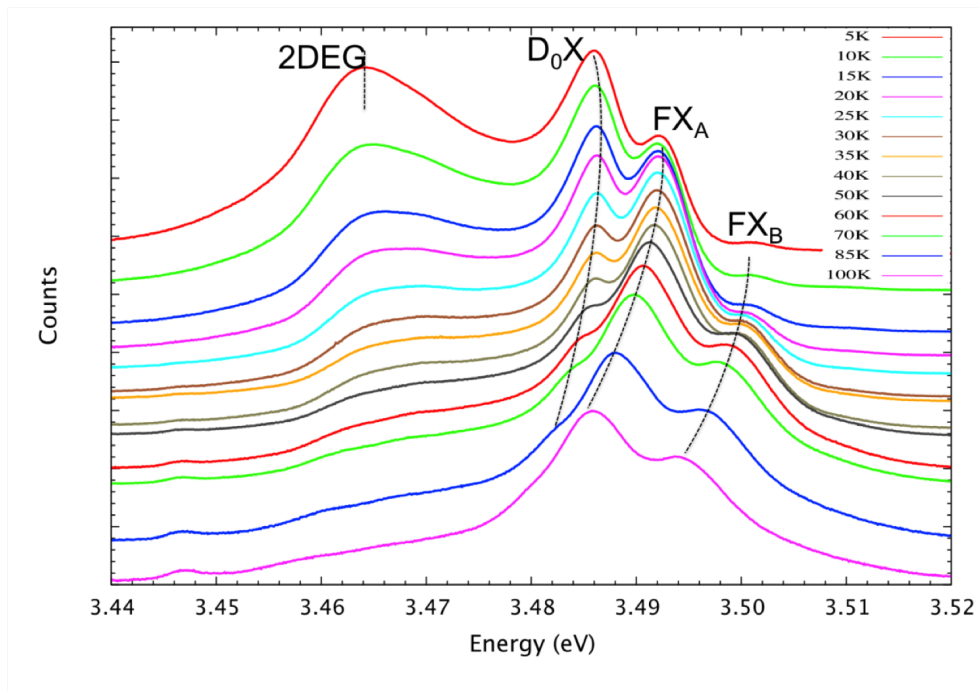


FIGURE 5.23: PL spectra of sample 3232 obtained with HeCd laser at different temperatures.

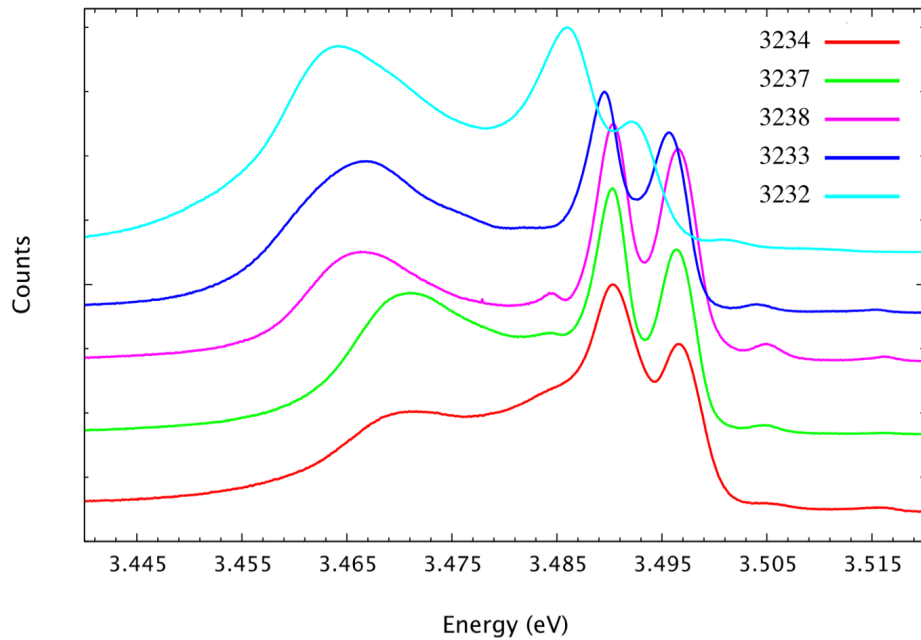


FIGURE 5.24: PL spectra of samples of various AlGaInN/(AlN)/GaN heterostructures at 5K obtained with HeCd laser.

Band structure and the quantized energy levels in the triangular well (2DEG region) of the AlGaInN/AlN/GaN heterostructure were obtained by solving self-consistently Schrödinger-Poisson equation using nextnano software (ref). In this calculation, pseudomorphic growth of AlN and AlGaInN on GaN was assumed. The compressive strain present in GaN (as assessed from HR-XRD) was taken into account. The free electron concentration of $3 \times 10^{17} \text{ cm}^{-3}$ in GaN was used, as measured by C-V measurements. Under these conditions, we observed three occupied energy levels (corresponding to $n=1, 2$ and 3) in the quantum well. As shown in fig. 5.25, the probability density function $|\Psi|^2$ for each occupied energy level shifts away from the AlN/GaN heterojunction as the energy level increases. Since the electron wavefunction for $n=1$ is situated in close proximity to the heterojunction and holds a deeper energy level, electrons occupy this level in this level are more confined with respect to those relevant to $n=2$ and $n=3$ 5.25. This suggests the electrons in excited states are more likely to cause the H-band. In table 5.6, is shown the energy difference between excited energy state ($E_{n=1}, E_{n=2}, E_{n=3}$) and valence band edge in the flat band region. This energy difference should correspond to the recombination of 2DEG electrons with photo-generated holes, giving rise to the H-band peak. From the comparison of the calculated values of the energy difference and the measured values for H-band peak (see table 5.6), we find out that recombination involving electrons in $E_{n=2}$ are mostly responsible for the occurrence of H-band. This

could be perceived as the confined electrons in the first excited quantized state penetrates further into GaN substrate and leads to a higher probability for the concerned recombination. On the other hand, $E_{n=3}$ which lies very close to the Fermi level may not be significantly populated to produce a detectable luminescence.

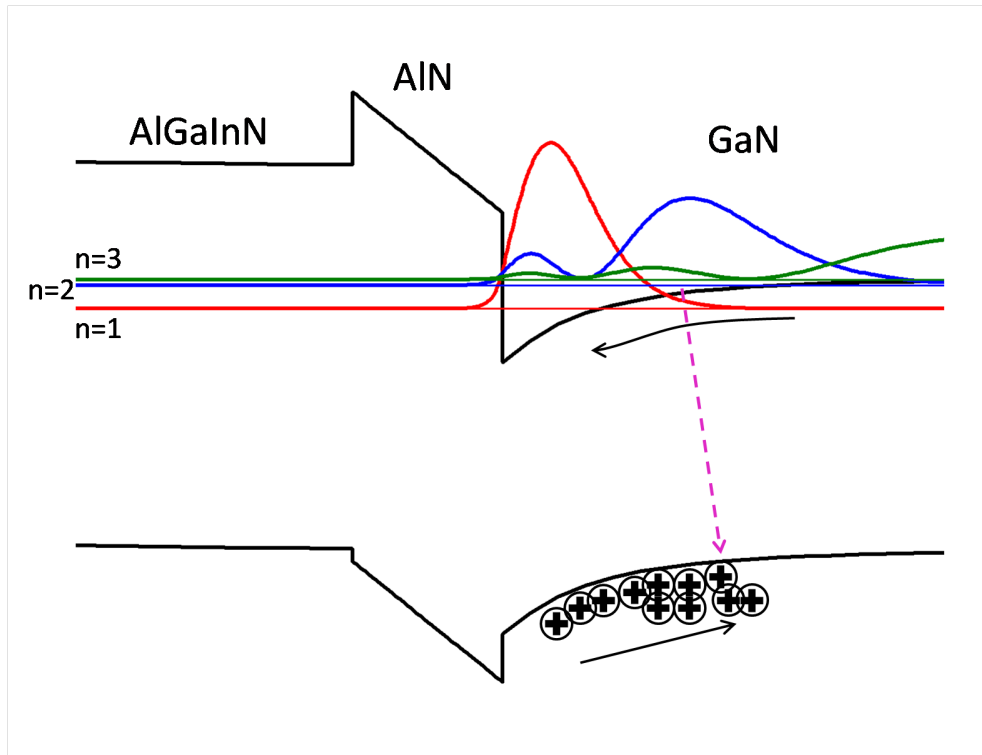


FIGURE 5.25: Schematic of the carrier recombination associated to 2DEG-related emission.

TABLE 5.6: Comparison of possible emission energies occurring via recombination between electrons in quantized energy states ($E_{n=1}$, $E_{n=2}$, $E_{n=3}$) and photo-excited holes in valence band edge (in flat band region of GaN) with experimentally measured emission peak in sample 3233.

Calculated ($\text{Al}_{0.6}\text{Ga}_{0.4}\text{N}$)		Measured (3233) ($\text{Al}_{0.58}\text{Ga}_{0.38}\text{N}$)
$E_{\text{VBM}}-E_{n=1}$	3.223 eV	3.462 eV
$E_{\text{VBM}}-E_{n=2}$	3.457 eV	
$E_{\text{VBM}}-E_{n=3}$	3.503 eV	

Based on carrier dynamic study by Kwack et al. in AlGaInN/GaN heterostructures [40], the carrier generation, transfer, and recombination dynamics of the 2DEG-related emission can be extended to AlGaInN/AIN/GaN heterostructures, which is explained as follows (schematic in 5.25). (i) After carrier photogeneration of by laser excitation,

effective carriers (photoexcited electrons) transfer from the GaN region to the triangular potential well at the heterointerface occurs due to strong built-in internal field. (ii) Because of the high density of electrons in the 2DEG states by residual and transferred electrons, the decay of the 2DEG recombination relies on the lifetime of the photogenerated holes. Most photogenerated holes must exist in the GaN flatband region due to the strong built-in internal electric field near the heterointerface, and contribute not only to the “spatially-indirect” (slower) 2DEG-related recombination between electrons in 2DEG states at heterointerface and holes in GaN flatband region but also to the “spatially direct” (faster) GaN recombination (between electrons and holes in GaN flatband region). In this stage, recombination occurs with faster decay time. (iii) After exhaustion of most photogenerated electrons in the GaN flatband region via the fast recombination process, recombination between the electrons in the 2DEG states and remaining holes in the flatband region can still proceed to the 2DEG emission. This would usually occur with a slower decay time.

Bibliography

- [1] A. Vilalta-Clemente, M-A. Poisson, H. Behmenburg, C. Giesen, M. Heuken, and P. Ruterana. *Phys. Status Solidi A*, 207:1105, 2010.
- [2] R. Butte, J-F. Carlin, E. Feltin, M. Gonschorek, S. Nicolay, G. Christmann, D. Simeonov, A. Castiglia, J. Dorsaz, H. J. Buehlmann, S. Christopoulos, G. Baldassarri Hoeger von Hoegersthal, A. J. D. Grundy, M. Mosca, C. Piquier, M. A. Py, F. Demangeot, J. Frandon, P. G. Lagoudakis, J. J. Baumberg, and N. Grandjean. *J. Phys. D: Appl. Phys.*, 40:6328–6344, 2007.
- [3] R Garcia, R. Magerle, and R. Perez. *Nature Materials*, 6:405, 2007.
- [4] M. Jung and J. W. Choi. *Ultramicroscopy*, 110:670–675, 2010.
- [5] V. Timon, S. Brand, S. J. Clark, M. C. Gibson, and RA Abram. *Phys. Rev. B*, 72:0353276, 2005.
- [6] J.J. Zhu, Y.M. Fan, H. Zhang, G.J. Lu, H. Wang, D.G. Zhao, D.S. Jiang, Z.S. Liu, S.M. Zhang, G.F. Chen, B.S. Zhang, and H. Yang. *Journal of Crystal Growth*, 348:25–30, 2012.
- [7] J. H. Leach et al. *Journal of Appl. Phys.*, 107:083706, 2010.
- [8] Z. Lillental-Weber, Y. Chen, S. Ruvimov, and J. Washburn. *Phys. Rev. Lett.*, 79:2835, 1997.
- [9] E. Arslan, S. Altindal, S. Ocelik, and E. Ozbay. *Semicond. Sci. Technol.*, 24:075003, 2009.
- [10] E. Arslan, S. Butun, and E. Ozbay. *Appl. Phys. Lett.*, 94:142106, 2009.
- [11] W. Chikhaoui, J-M. Bluet, M-A. Poisson, N. Sarazin N, C. Dua C, and C. Bru-Chevallier. *Appl. Phys. Lett.*, 96:072107, 2010.
- [12] J. Kovac, R. Sramaty, A. Chvala, H. Sibboni, E. Morvan, M-A. Poisson, D. Donoval, and P. Kordos P. *Appl. Phys. Lett.*, 98:162111, 2011.

- [13] D. Donoval, A. Chvala, R. Sramaty, J. Kovac, J-F. Carlin, N. Grandjean, G. Pozzovivo, J. Kuzmik, D. Pogany, G. Strasser G, and P. Kordos. *Appl. Phys. Lett.*, 96:223501, 2010.
- [14] M. Gonschorek, J-F. Carlin, E. Feltn, Py. M. Marcel, and N. Grandjean. *International Journal of Microwave and Wireless Technologies*, 2(1):13–20, 2010.
- [15] S. Pandey, B. Fraboni, D. Cavalcoli, A. Minj, and A. Cavallini. *Appl. Phys. Lett.*, 99:012111, 2011.
- [16] E. Arslan, S. Altindal, S. Ozcelik, and E. Ozbay. *J. Appl. Phys.*, 105:023705, 2009.
- [17] R. K. Chanana, K. McDonald, M. Di. Ventra, S. T. Pantelides, and L. C. Feldmanb. *Appl. Phys. Lett.*, 77:2560, 2011.
- [18] E. H. Rhoderick and R. H. Williams. *Metal-semiconductor contacts*. Oxford University Press, New York, 1988.
- [19] A. A. Grinberg. *Phys. Rev. B*, 32:8187, 1985.
- [20] L. Yuan, H. Chen, Q. Zhou, C. Zhou, and K. J. Chen. *IEEE Electron Device Lett.*, 32:1221, 2011.
- [21] M. M. Yazdanpanah, S. A. Harfenist, A. Safir, and R. W. Cohn. *J. Appl. Phys.*, 98:073510, 2005.
- [22] B. Pecz, Zs. Makkai, M. A. di Forte-Poisson, F. Huet, and R. E. Dunin-Borkowski. *Appl. Phy. Lett.*, 78:1529, 2001.
- [23] Th. Kehagias, G. P. Dimitrakopulos, J. Kioseoglou, C. Giesen H. Kirmse, M. Heuken, A. Georgakilas, W. Neumann, Th. Karakostas, and Ph. Komninou. *Appl. Phys. Lett.*, 95:071905, 2009.
- [24] J. E. Northrup, L. T. Romano, and J. Neugebauer. *Appl. Phys. Letts.*, 74:2319, 1999.
- [25] O. Ambacher, B. Foutz, J. Smart, J. R. Shealy, N. G. Weimann, K. Chu, M. Murphy, A. J. Sierakowski, W. J. Schaff, L. F. Eastman, R. Dimitrov, A. Mitchell, and M. Stutzmann. *J. Appl. Phys.*, 87:334–344, 2000.
- [26] M. Gonschorek, J-F. Carlin, E. Feltn, M. A. Py, and N. Grandjean. *Appl. Phys. Lett.*, 89:062106, 2006.
- [27] C. McAleese, M. J. Kappers, F. D. G. Rayment, P. Cherns, and C. J. Humphrey. *J. Crys. Growth*, 272:475–480, 2005.

- [28] Y. Cao and D. Jena. *Appl. Phys. Lett.*, 90:182112, 2007.
- [29] A. Teke, S. Gokden, R. Tulek, J. H. Leach, Q. Fan, J. Xie, U. Ozgur, H. Morkoc, S. B. Lisesivdin, and E. Ozbay. *New J. Phys.*, 11:063031, 2009.
- [30] J. Xie, X. Ni, M. Wu, J. H. Leach, U. Ozgur, and H. Morkoc. *Appl. Phys. Lett.*, 91:132116, 2007.
- [31] S. J. Hearne, J. Han, S. R. Lee, J. A. Floro, D. M. Follstaedt, E. Chason, and I. S. T. Tsong. *Appl. Phys. Lett.*, 76:1534–1536, 2000.
- [32] M. Germain, M. Leys, S. Boeykens, S. Degroote, W. Wang, D. Schreurs, W. Ruythooren, K. Choi, B. Van Daele, G. Van Tendeloo, and G. Borghs. *Mat. Res. Soc. Symp. Proc.*, 798:Y10.22.1, 2004.
- [33] A. Minj, D. Cavalcoli, and A. Cavallini. *Appl. Phys. Lett.*, 97:132114, 2010.
- [34] D. C. Look and J. R. Sizelove. *Phys. Rev. Lett.*, 82:61237–61240, 1999.
- [35] J. P. Bergman, Q. X. Zhao, P. O. Holtz, B. Monemar, M. Sundaram, J. L. Merz, and A. C. Gossard. *Phys. Rev. B*, 43:4771–4776, 1991.
- [36] Q. X. Zhao, J. P. Berman, P. O. Holtz, B. Monemar, C. Hallin, M. Sundaram, J. L. Merz, and A. C. Gossard. *Semicond. Sci. Technol.*, 5:884, 1990.
- [37] I. V. Kukushkin, K. V. Klitzing, and K. Ploog. *Phys. Rev. B*, 37:8509–8512, 1998.
- [38] R. Kudrawiec, M. Syperek, J. Misiewicz, M. Rudzinski, A. P. Grzegorzczuk, P. R. Hageman, and P. K. Larsen. *phys. stat. sol. (c)*, 6:2117–2120, 1985.
- [39] Y. R. Yuan, M. A. A. Pundes, G. A. Vawter, and J. L. Merz. *J. Appl. Phys.*, 58:397, 1985.
- [40] H-S. Kwack, Y-H. Choa, G. H. Kim, M. R. Park, D. H. Youn, S. B. Bae, K.-S. Lee, J-H. Lee, J-H. Lee, T. W. Kim, T. W. Kang, and K. L. Wang. *Appl. Phys. Lett.*, 87:041909, 2005.

Chapter 6

InGaN

InGaN alloys are widely used as active layers and are already commercialized for optoelectronic applications such as light-emitting diodes (LEDs) and laser diodes (LDs) operating in the UV/blue spectral range, even under high temperature and high power conditions. Their behavior is associated with phenomena such as indium-segregation at dislocations, formation of InN quantum dots in the bulk, misfit dislocations, etc [1][2][3][4]. They can cause enhanced leakage current and can significantly affect the emission properties of the devices and hence prevent the devices to achieve high performance. The main aim of this chapter is to give a deep insight into the surface properties, electronic properties of extended defects and their correlation with the emission properties of InGaN, which would be very useful to realize more efficient optoelectronic devices.

6.1 Structural properties

We have studied undoped-InGaN/GaN heterostructures for indium content varying between 13% and 19.5%. InGaN layers with a nominal thickness of 50 nm were MOCVD grown along (0001) direction on GaN/sapphire template. Indium percent in these samples were determined by HRXRD. Table 6.1 shows the characteristics of all InGaN samples studied here in terms of surface roughness, threading dislocation density (TDD), misfit dislocation density (MDD). Here, the surface roughness, TDD and MDD were calculated from $5 \times 5 \mu m^2$ AFM topography images. Due to limitations associated with AFM, TDD and MDD could be underestimated. Based on the surface morphology (see fig. 6.1), all the samples here can be categorized into three types.

Type I: High quality samples: A1, A2, A4, A3, A2 and A5. Their surface exhibits granular features, low surface roughness from 0.35 to 0.60 nm, a TDD of $\approx 2.0 \times 10^8$

TABLE 6.1: Details (indium percentage, roughness, TDD, MDD) of the samples used in our work.

	Sample	In%	Roughness (nm)	TDD (cm ⁻²)	MDD (μm ⁻¹)
type I	A1	13.0	0.351	2.2 x 10 ⁸	-
	A2	16.2	0.505	2.0 x 10 ⁸	-
	A3	16.3	0.414	1.3 x 10 ⁸	-
	A4	16.8	0.602	2.8 x 10 ⁸	-
	A5	17.0	0.585	2.4 x 10 ⁸	-
type II	B1	18.1	0.616	3.0 x 10 ⁸	*0.7-3.0 ²
	B2	18.8	0.831	2.9 x 10 ⁸	*0.8-7.2 ¹
	B3	19.2	0.789	2.9 x 10 ⁸	*1.1-5.6 ³
	B4	19.5	0.858	2.8 x 10 ⁸	*1.3-7.0 ³
type III	C1	16.0	0.582	-	-
	C2	17.0	0.776	-	-

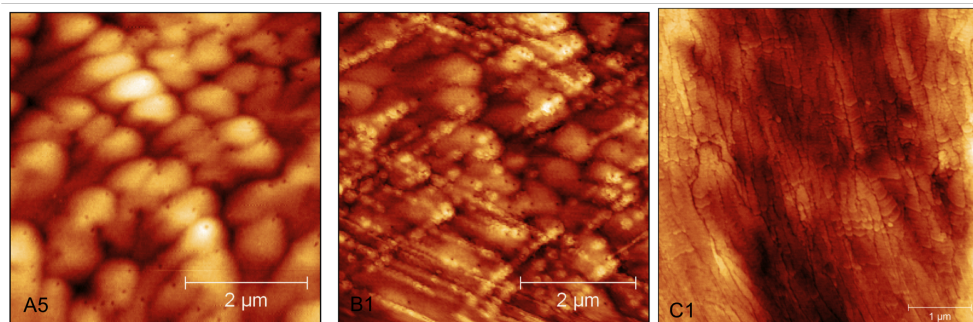


FIGURE 6.1: Surface morphology of samples categorized as TypeI, II and III .

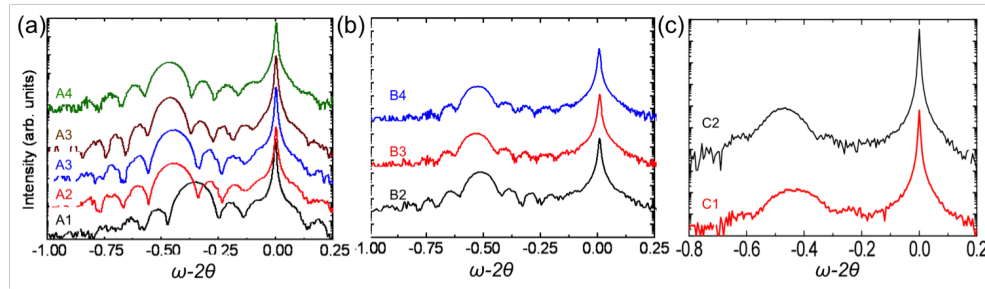


FIGURE 6.2: XRD $\omega - 2\theta$ curves of InGaN with varying indium percent from 13% to 19.5%. Samples C1 and C2 (on right side) showed no XRD interference fringes.

and almost no misfit dislocations. We expect these TDs to originate from the substrate GaN which contains TDD of $\approx 3 \times 10^8$ at the surface. XRD interference fringes indicates presence of good quality interface (see fig. 6.2a).

Type II: B1, B2, B4, B3 and B4 are samples containing misfit dislocations, as observed from their AFM topography, but they still show smooth surfaces and XRD interference fringes (6.2b). There are no significant differences in the TDD with respect to the above discussed samples.

Type III: Samples C1 and C2 showed a poor surface morphology (see fig. 6.1c) with presence of high density trenches. Due to this, dislocation density could not be determined with AFM. The absence of any interference fringes in their XRD plot confirms poor structural formation and interface (fig. 6.2 2b).

A number of reports suggest that it is quite hard to grow good quality In-related alloys (InGaN in our case), which may often suffer from problems such as In-segregation, droplet formation and formation of extra threading dislocations for InGaN with a higher indium content. Even if one is able to avoid them, non-basal slip planes are found to be active at misfit dislocations [5]. We present here an example of this. As shown in fig. 6.33, as the indium-content increases in InGaN, slip-planes start to evolve. Though there are theoretical limits to the critical thickness for different percentage of indium in InGaN, they would be mostly overestimated because formation of misfit dislocations is also strongly dependent on the growth conditions. Two sets of samples were prepared to study the effect of growth parameters on the sample quality. The first set of sample (shown in fig. 6.3a) shows the effect of growth pressure while keeping all other growth parameters constant. It is very well demonstrated here that as the growth pressure increases, indium is consequently more incorporated in InGaN, i.e. from 17% to 17.6% and further to 19.5%. However, another effect observed here is the formation of misfit dislocations. At 17% of indium, there are no misfit dislocations observed but they appear at an indium percent of 17.6 and as the indium percent increases to 19.5 their density increases. Similar observation, i.e. from low density to high density of misfit dislocations,

is also seen as the growth temperature increases, while keeping other growth conditions constant (shown in fig. 6.3b).

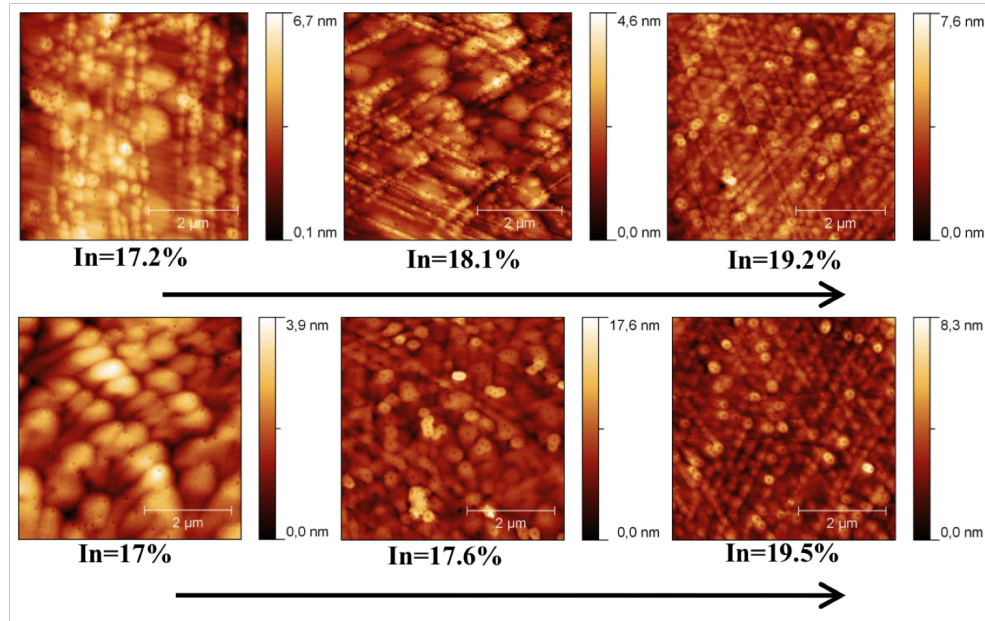


FIGURE 6.3: Two set of samples grown at increasing growth pressure (top) and temperature (bottom) resulting in an increase in indium incorporation in InGaN. Density of V-pits remains in the same order of 10^8 while density of non-basal slip planes increases with In percentage.

At this point, it would be interesting to study two kinds of extended defects: threading dislocations and misfit dislocations associated to non-basal slip planes. This will be one of the purposes of this thesis.

6.2 Electrical characterization of the surface

We already introduced the concept of threading dislocations, their origin and their structural and electrical properties in GaN in chapter 4. The surface characterization techniques (C-AFM, SKPM and EBIC) are further extended to characterize the behavior of threading dislocations in InGaN and the role of indium incorporation in InGaN.

6.2.1 Effect of indium incorporation

InGaN sample A5 with 17% indium was chosen to focus on the threading dislocations. The topography in (fig. 6.4a) shows a very smooth surface with a root mean square roughness of 0.585 nm over $5 \times 5 \mu m^2$. Other features observed are grain-like features that are typical of MOCVD growth [6].

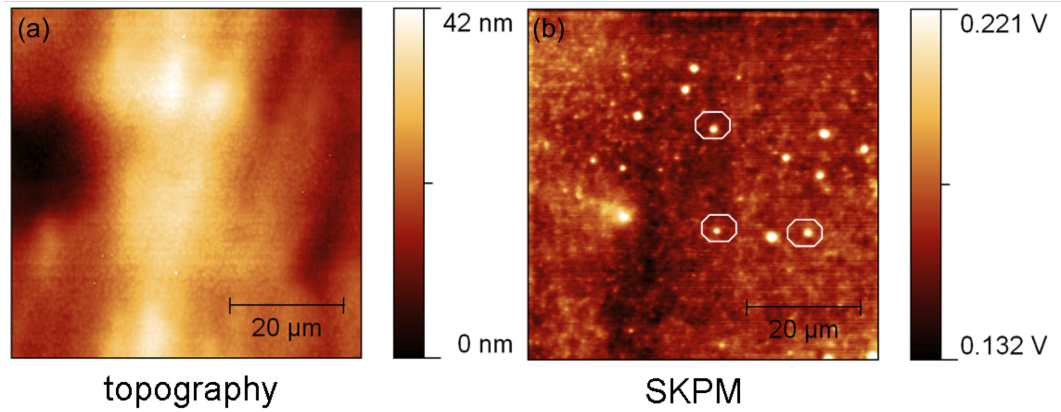


FIGURE 6.4: (a) topography and its corresponding (b) SKPM map of InGaN obtained at tip-sample distance = 5 nm.

As shown in fig. 6.4b, which is the corresponding SKPM map of the topography in fig. 6.4a, a contrast inversion in the surface potential variation around dislocations is observed in contrary to the case of unintentional doped GaN (chapter 4). This suggests an increment in the surface potential at the dislocations with respect to the dislocation free surface. This was not the case in GaN where the facets were N-terminated. In InGaN or, in general, indium-related alloys with high In%, independently of the polarity, the surfaces are usually indium terminated. This was demonstrated by Chen et al. [7] using LEED and STM techniques. One monolayer of indium atoms is formed over last N-layer in $000\bar{1}$ surface. In (0001) surface and indium adatoms are formed over the In-Ga layer. This is well represented in figure 6.5 below. Formation of In-monolayers or bilayers could have a great impact on the electronic properties of the surface. This is evident in InN where the surface is more degenerate than the bulk [8] i.e. conduction band edge is bended downwards at the surface and Fermi level lies above the conduction band edge. This is important to mention because downward bending of the conduction band at the surface refers to a non-depleted surface, and could cause charging of acceptor states.

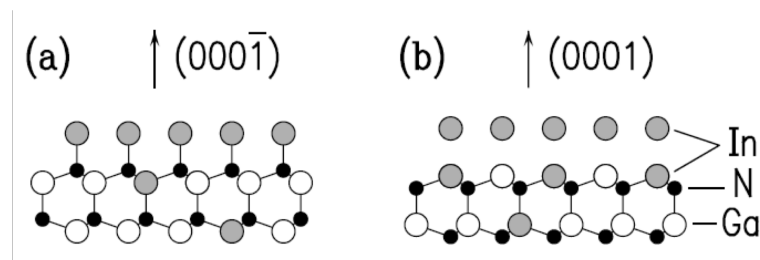


FIGURE 6.5: Basic structure of InGaN surfaces: (a) $000\bar{1}$, surface is determined by one monolayer of indium atoms. (b) (0001) , surface is terminated with two layers of metal atoms, with the top layer being entirely In, and second layer containing a mixture of In and Ga. [7]

To focus on the surface potential associated with the threading dislocations, $12 \times 12 \mu\text{m}^2$ topography of the same sample is presented in fig. 6.6a. Threading dislocation density measured by AFM in this sample is around $\approx 2.4 \times 10^8 \text{ cm}^{-2}$. Its corresponding SKPM map is shown in fig. 6.6b. One may clearly observe here that at threading dislocations there is an increment in the surface potential. It is worth noting that around 62% of the total number of threading dislocations were associated with increased surface potential, while others were not. For demonstration, some of the threading dislocations are encircled in white in fig. 6.6a. The corresponding surface potentials in the same location of TDs are encircled in either white or blue in fig. 6.6b. Here, the blue or white encircled regions represent the location where surface potential has either increased or hasn't shown any variation, respectively. An increment in surface potential at the threading dislocations is a clear indication that they are associated to negatively charged acceptor states. Since, dangling bonds are typical characteristic of edge threading dislocations (which can cause gap states), we can say that dislocations with an edge component are negatively charge. This gives us an approximate estimate of number of dislocations with an edge component (i.e. pure edge- and mixed- TD a) to be $\approx 62\%$ and only with an screw component to be $\approx 38\%$. As shown in the surface potential profile across the two threading dislocations (marked as A and B in fig. 6.6a,b), in fig. 6.6c, the measured increment in the surface potential is $\approx 20 \text{ meV}$. The fact that these dislocations are related to gap states is also well supported by our EBIC measurements where they appear as dark contrast (fig. 6.7). A new kind of V-pit or dislocation (named as type-C V-pit in this thesis) was also consistently observed in this sample (marked as C) with a density of $2 \times 10^6 \text{ cm}^{-2}$, which were identified with a much higher surface potential $\approx 0.18 \text{ eV}$. Only with other complimentary techniques, this type of V-pit can be identified. Interestingly, the EBIC map shows that they also act as strong recombination centers (encircled in fig. 6.7). Though the free electron concentrations were roughly in the same order of 10^{17} cm^{-3} in both InGaN and GaN samples, the absence of any negatively charged dislocation in GaN can be understood from the fact that GaN surface is depleted in comparison to the non-depleted InGaN surface. Besides this, owing to the wide band gap of GaN, its surfaces are more likely to get charged during local electrical measurements, thus screening any negatively charged regions.

The conductive AFM was performed both in forward bias and reverse bias with a degenerately p-doped diamond tip. As explained in chapter 4, the current distribution on the surface would dominantly depend on the barrier-height variation and resistivity, due to the formation of metal-semiconductor junction between the AFM tip and sample. No major current variations were observed neither in forward nor reverse bias for this indium content. This contradicts the result on C-AFM on InGaN by Cao et al. [9] et al., where high local conductivity was observed around the threading dislocations. C-AFM

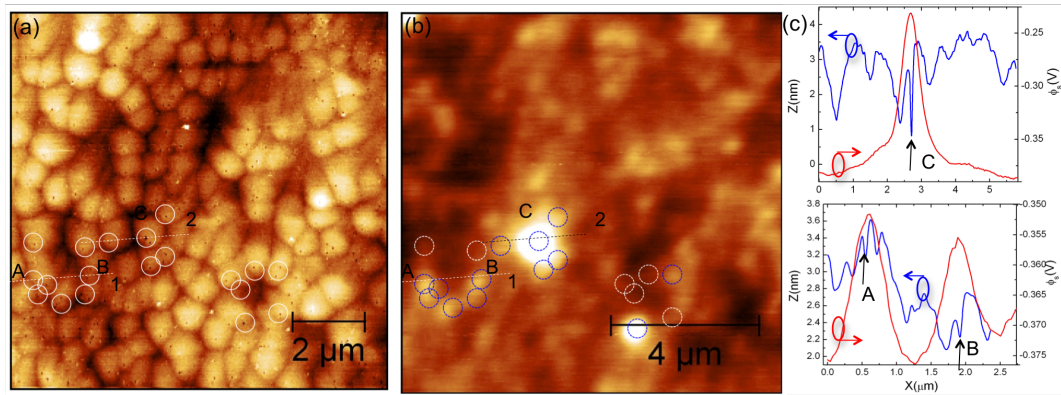


FIGURE 6.6: EBIC micrograph of InGaN obtained at 7.3kV. Dark contrast is represents the recombination center (i.e. threading dislocation) and type-C V-pits (encircled).

map obtained at -19 V is exhibited in fig. 6.8(a). Based on the current distribution in this area (shown in fig. 6.8b), barrier height variation can be estimated from the Schottky thermionic emission equation (given in chapter 4). Estimated average barrier height doesn't deviate from its median value by more than 20 meV. This value is in good agreement with the surface potential variation across the dislocations (see fig. 6.6c). One would also notice in fig. 6.8a that almost no current was observed at the center of the dislocations (appearing as dark contrast). This is mostly due to contact area reduction between the diamond tip and the V-defect depression owing to large tip radius of the tip.

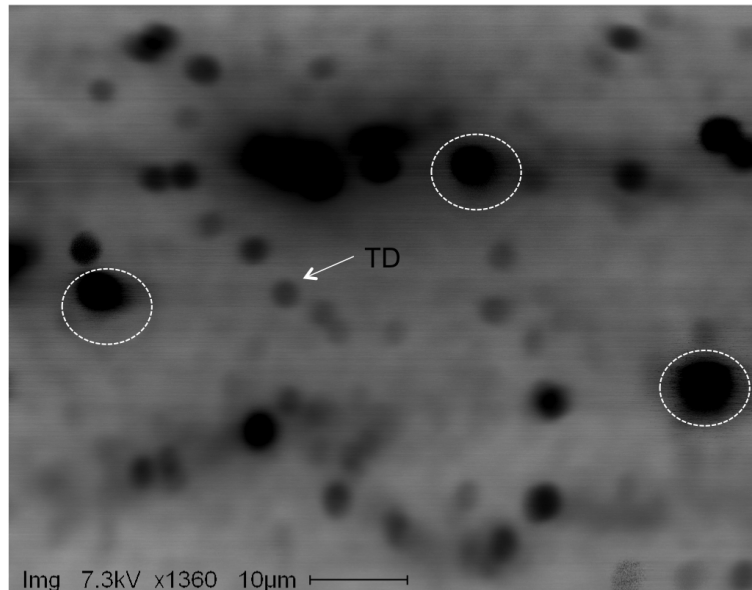


FIGURE 6.7: (a) topography of InGaN (color scale:6.5 nm)and its corresponding (b) SKPM map (color scale: 180 mV); (c) SKPM profile across the threading dislocations. Threading dislocations are encircled in the topography image and in SKPM map showing a one-to-one relation.

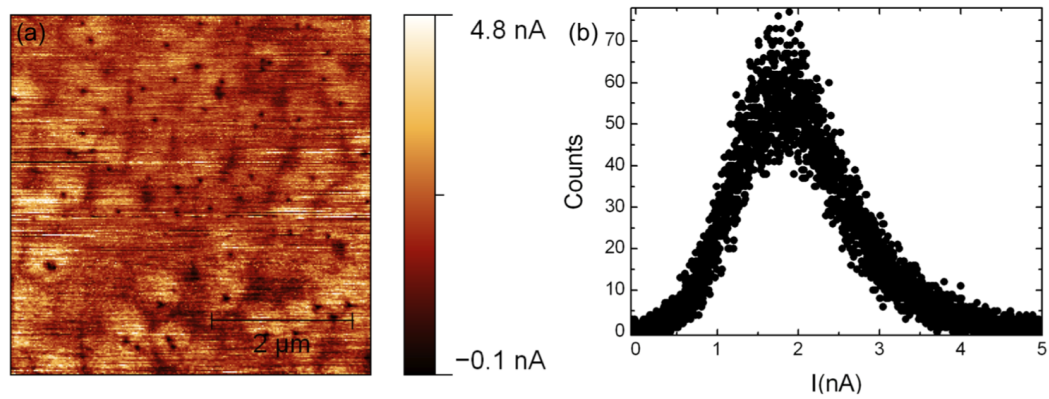


FIGURE 6.8: (a) Current AFM map obtained at -19 V and (b) the statistical distribution of current over this area.

In order to study the effect of indium incorporation in InGaN, same analysis (SKPM and CAFM) was done on $In_{0.19}Ga_{0.81}N$. For this indium percent, features related to misfit dislocations were observed. This was already briefed earlier in this chapter. Figures 6.9(a) and (b) shows the topography and its corresponding Kelvin potential map. As shown before, a higher surface potential was again observed at the threading dislocations. Apart from this, misfit dislocations, too, were associated with high surface potential with an increment of ~ 50 meV. Similar surface potential behavior at threading dislocations and misfit dislocations suggest that MDs, too, are negatively charged owing to the filled acceptor states. MDs in InGaN were already demonstrated in CL measurements to act as non-radiative recombination centers by Srinivasan et al. [5]. Our results summarizes that both TDs and MDs form gap states, which are partially or fully filled.

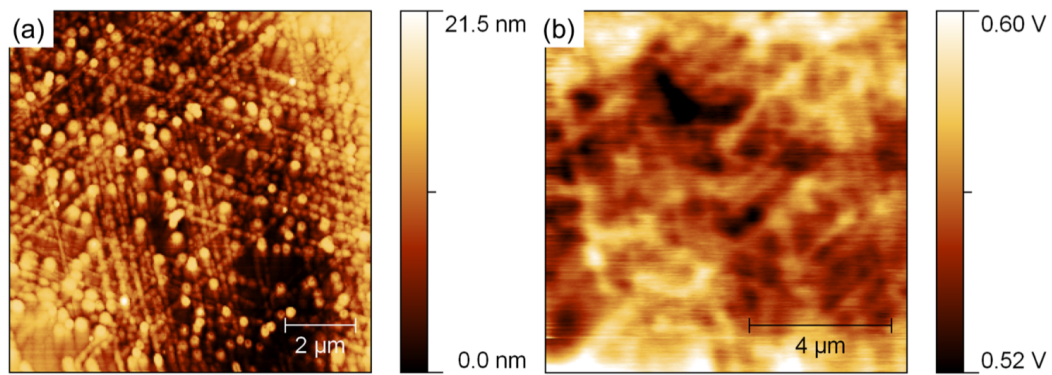


FIGURE 6.9: (a) topography and its corresponding (b) SKPM map of $In_{0.19}Ga_{0.81}N$. Threading dislocations and misfit dislocations appear as bright contrast in SKPM map.

In this sample, conductivity measurements were performed in both forward and reverse bias. When either forward (+2.5 V) or reverse biased (-10 V), unlike sample A5 (In=17%), higher conductivity was observed at the threading dislocations (see fig. 6.10). Thus, as already suggested before, InGaN samples with a higher indium percent

are prone to more indium fluctuations (inclusions in our case), V-shaped opening at the threading dislocations serve as a site for the segregation of high amount of indium [1]. As a consequence of indium inclusion at the threading dislocations, there would be a local band gap lowering and the formation of conduction path via indium-rich threading dislocation core. From the Schottky emission equation (chapter 4), the change in the barrier height at the dislocation can be estimated. Based on the current measured in the reverse bias at dislocation and dislocation free region, the change in the barrier height ($\delta\phi$) at the dislocation is calculated to be around 57 meV. This is in good agreement with the surface potential variation observed near the dislocation (varying between 40 and 60 meV). It is also important to mention that now it is evident from CAFM measurements that misfit dislocations are not associated with enhanced local conductivity, which suggests that they do not contribute to leakage current. Thus, it can be summarized that threading dislocations and misfit dislocations are both negatively charged, but differ from each other on the basis of indium inclusion, since indium inclusion is only present in the former.

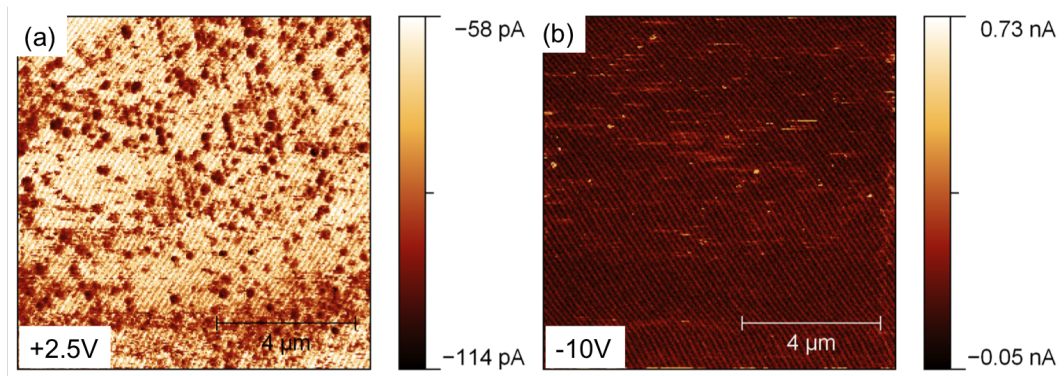


FIGURE 6.10: (a) C-AFM map obtained at forward bias of +2.5 volts and (b) reverse bias of -10 volts..

An increment in local conductivity at threading dislocations is observed. Here we have shown that, threading dislocations and misfit dislocations in InGa_N were negatively charged as assessed from SKPM. Based on the current distribution (C-AFM) over an area for both 17% and 19.5% In in InGa_N, estimated barrier height variation proves that as the indium content in the sample increases, there is a significant indium inclusion locally. This effect is seen more pronounced near the associated threading dislocations. These results support the hypothesis that segregation of indium is a major problem in InGa_N with high In content and would result in high leakage current in InGa_N.

6.3 Optical characterization with PL

PL spectra of the four samples (A1, A4, B2 and B4) at 5K obtained by HeCd excitation are shown in figure 6.11. The emission bands observed in these samples are usually related to recombination of localized excitons trapped at local potential fluctuations. Temperature dependent PL spectra at low excitation for sample A4 (16.8% indium) are shown in figure 6.12, where clearly S-shape behavior of the peak emission energy is observed. This kind of behavior has also been reported frequently before [2],[10],[11]. As clearly demonstrated in fig. 6.13, at low temperatures ($T < 50K$), there is a red-shift ($\sim 5 meV$) in the peak-emission energy, followed by a blue-shift ($\sim 15 meV$) up till 125K and red-shift with further increase in temperature. This blue-shift of 15meV is quite comparable with the ones reported in Ref. [2],[10] and [11]. Following the concept of luminescence in InGaN via band-filling model for tails of the DOS proposed by P.Eliseev et al.[10], we attribute the blue-shift observed in the temperature range 50K-125K to the same phenomenon. There can be various reasons for the formation of band-tail states in InGaN: (1) statistical fluctuation in the composition causing formation of indium rich regions, (2) impurity states, (3) lattice deformation and (4) formation of In-rich quantum dots in the bulk [2]. However, we should not forget that, due to the high lattice mismatch between GaN and InGaN, there is a high density of threading dislocations, $\sim 10^8 - 10^9 cm^{-2}$, and recently many observations of In segregation at these sites were reported [12],[13],[1]. Due to these inhomogeneities, potential minima in the conduction band are formed at the In-rich regions, attributed to band-tail states.

Red-shift (5K-50K): Compared to 5meV red-shift in sample A4, an energy decrease by ~ 6 to $\sim 13 meV$ was observed in sample A1, B4 and B2. Similar low temperature observations were seen before in InGaN [11] and other materials with alloy fluctuations [14], [15]. Smith et al. [16] and Harris et al. [17] showed that in high quality nitrides (InGaN and GaN), at low temperatures localized exciton recombination lifetime is much higher compared to PL recombination lifetime at higher temperatures causing carriers can diffuse/relax towards the potential minima located at the tail states caused by composition fluctuation before recombination. We expect that due to the radiative recombination, where an increase in carrier lifetime with temperature is its typical characteristic, peak emission energy shifts to a lower energy as the temperature increases from 5K to 50 K. Such a red-shift in the low temperature regime could also be seen as a characteristic of good-quality material.

Blue-shift (50K-125K) and red-shift (125K-300K): This phenomenon can be explained by the fact that at higher temperatures, non-radiative processes dominate, reducing the carrier lifetime significantly. As the temperature further increases, the carrier lifetime starts to reduce with recombination occurring before carriers can relax to lower

energies, hence a blue-shift. This was around $\sim 12 \text{ meV}$ and $\sim 7.8 \text{ meV}$ for sample B2 and A1, respectively. These samples do not seem to deviate much from sample A4. From the band-filling model [10], temperature dependent peak emission energy $h\nu$ in the blue-shift region is given by

$$h\nu = E_0(0) - \frac{\alpha T^2}{T + \beta} - \frac{\sigma^2}{k_B T} \quad (6.1)$$

where α and β are Varshni's fitting parameters and σ is a fixed parameter defining Gaussian DOS distribution of band-tail states.

From the fitting of equation 6.1 with temperature dependent PL peak energy (see fig. 6.13), we extracted the key parameters: E_0 , α , β and σ . Red shift for temperature above 125K is due to the dominance of the second term in equation 6.1.

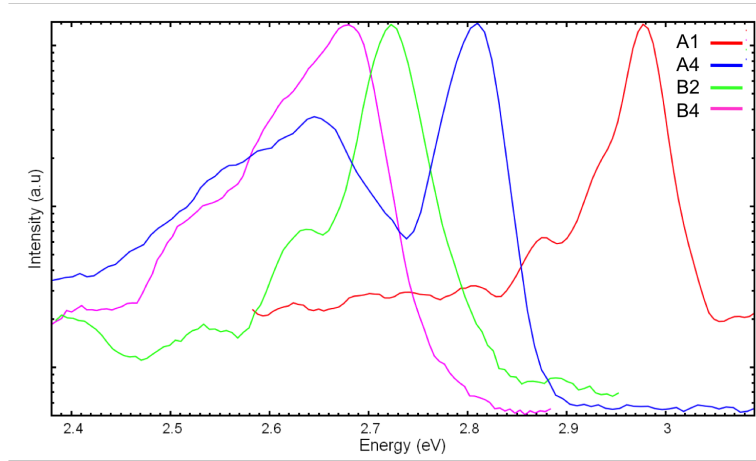


FIGURE 6.11: PL spectra of InGaN samples for 13%, 16.8%, 18.8% and 19.5% of indium.

TABLE 6.2: Varshni parameters for InGaN with In=13.0%, 16.8%, 18.8% and 19.5% extracted from low excitation spectra.

Sample	$E_0(0)$ (eV)	α (meV · K ⁻¹)	β (K)	σ (meV)	Ea (meV)
13.0%	2.995	0.51	700	12.5	10.7
16.8%	2.853	0.60	750	15.1	35.4
18.8%	2.771	0.77	700	18	37.0
19.5%	-	-	-	-	48.6

Calculation of activation energy

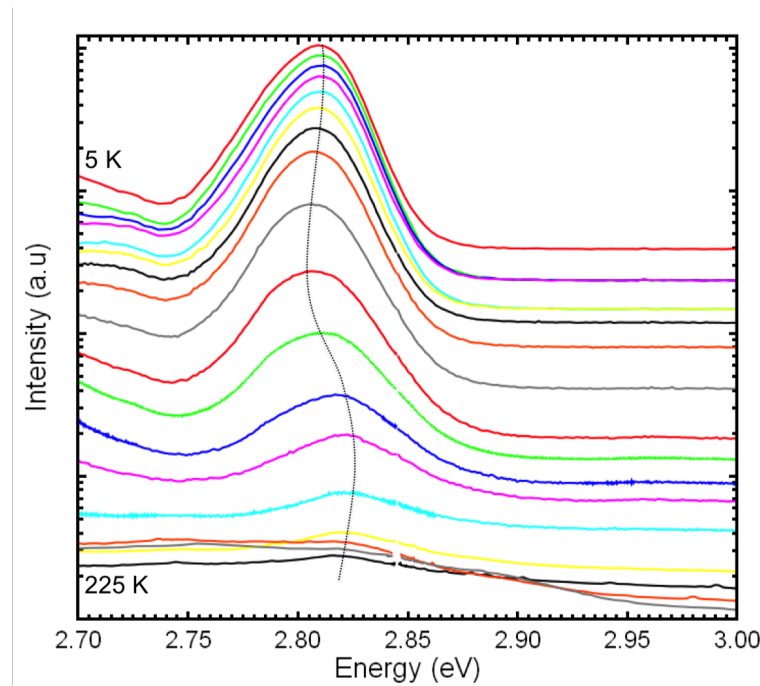


FIGURE 6.12: Temperature dependent PL spectra for sample A4 (In=16.8%). Temperature variation is as 5K, 10K, 15K, 20K, 25K, 30K, 35K, 40K, 50K, 60K, 70K, 85K, 100K, 125K, 150K, 170K, 200K and 225K from top to bottom. Dotted line is used as a guide for the eye to show S-shape behavior.

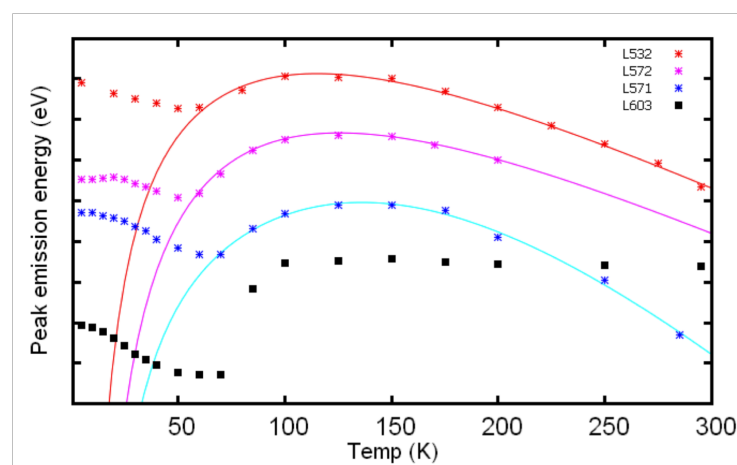


FIGURE 6.13: S-shape behavior of the peak emission energy observed in sample InGaN with In=13.0%, 16.8%, 18.8% and 19.5%. Y-axis division is equal to 10 meV.

Figure 6.14 shows the thermal quenching of the PL intensity at high temperature. Activation energy of an exciton can be extracted from the temperature dependence of the excitonic emission, which is given by

$$I(T) = \frac{I_0}{1 + \exp\left(\frac{-E_a}{kT}\right)} \quad (6.2)$$

From the Arrhenius plot of integrated PL intensity over the temperature range (see fig. 6.14) under investigation, we obtained the activation energies (E_a) of $\approx 10.3 \text{ meV}$, $\sim 35.4 \text{ meV}$, $\sim 37 \text{ meV}$ and $\sim 48.6 \text{ meV}$ for InGaN with 13.0%, 16.8%, 18.8% and 19.5% of indium. These activation energies monotonously increase with increasing indium concentration. This is in line with Eliseev's model where more fluctuations due to more indium replacing gallium atoms statistically lead to deeper potential fluctuations. E_a can be understood as an estimation of the characteristic disorder energy following the same trend as σ of Eqn. 6.1. Activation energies of 35 meV and 40 meV for exciton localization have already been reported [18],[11] in InGaN.

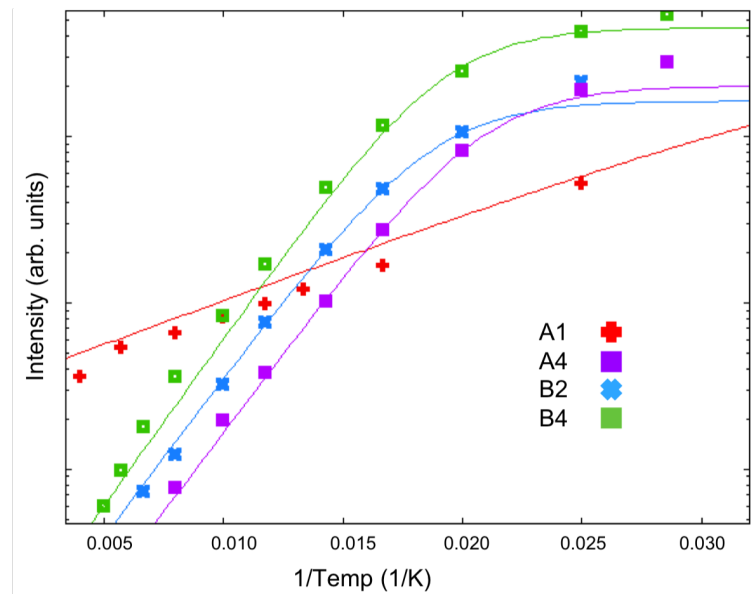


FIGURE 6.14: PL intensity vs temperature for samples A1, A4, B2 and B4.

If we compare the topographies of $5 \times 5 \mu\text{m}^2$ area of samples A1, A4 with B2 and B4, we will notice that other than V-pits or threading dislocations appearing in all the samples, additional features appearing in sample B2 and sample B4. They seem more likely as misfit dislocations aligned along $[1-100]_c$ related to non-basal slip planes. The slip planes in InGaN have been observed before by S. Sreenivasan for $In > 11\%$ and were shown to occur via punch out mechanism in strained InGaN [19]. Though basal slip planes are

inactive in hexagonal wurtzite structures, other slip systems such as $\{11-22\} \langle 11\bar{2}3 \rangle$, are potentially active and would facilitate plastic deformation for strain relaxation [5]. They could be very detrimental for the device, as they appear with a dark contrast in CL measurements indicating nonradiative recombination centers. It is very clear in table. 6.1 5 that density of misfit dislocations is relatively very high in sample B4 compared to sample B2. This is due to high indium content, which determines a lower critical thickness for B4 with respect to to B2 [20]. Since, we observed an increase in activation energy from 37 meV to 48 meV with the misfit dislocation density in InGaN, we could attribute presence of MDs to a higher E_a in sample B4. Apart from this, we have explored more on the correlation between structural properties and luminescence in InGaN that would be discussed in the next section.

6.3.1 Observation of high-excitation bands

We obtained power-dependent PL spectra of optically pumped of InGaN samples with excitation density at varying temperature from 5K to room temperature. There are very few studies on the excitation power dependence of PL in bulk InGaN and InGaN/GaN MQWs. They have reported a blue-shift in the peak-emission energy with an increase in excitation intensity attributing it to band filling effects. On optically pumping at high excitation density, we observe an additional band due to electron hole plasma recombination occurring at energies below that of the localized excitons. This phenomenon was observed only in our samples A1, A4, A3 and A2. All other samples exhibited only band filling effects as observed by others.

Typical spectra of sample A1 obtained with varying pump intensities at different temperatures are shown in figure 6.15 and as described earlier an additional peak in the lower energy region of the localized exciton peak starts to appear at $\sim 0.6 \text{ mJ.cm}^{-2}$, which shifts further to lower energy with increasing excitation density similar at all temperatures.

In order to know the origin of this emission, we have considered all the mechanisms that have been observed at high excitations in nitrides.

Electron-exciton scattering can be ignored here because of very low free electron concentration of $\sim 4 \times 10^{15} \text{ cm}^{-3}$ (calculated using C-V measurements). Exciton-exciton scattering, also known as P-band, which is due to the inelastic collision of excitons, excites one of the excitons involved in this process from its ground state to a higher energy state by absorption and consequently, decays another exciton with an equivalent loss of energy. Using a hydrogen-like model, the energy difference between the ground state and the n th energy state of an exciton can be expressed as [21]

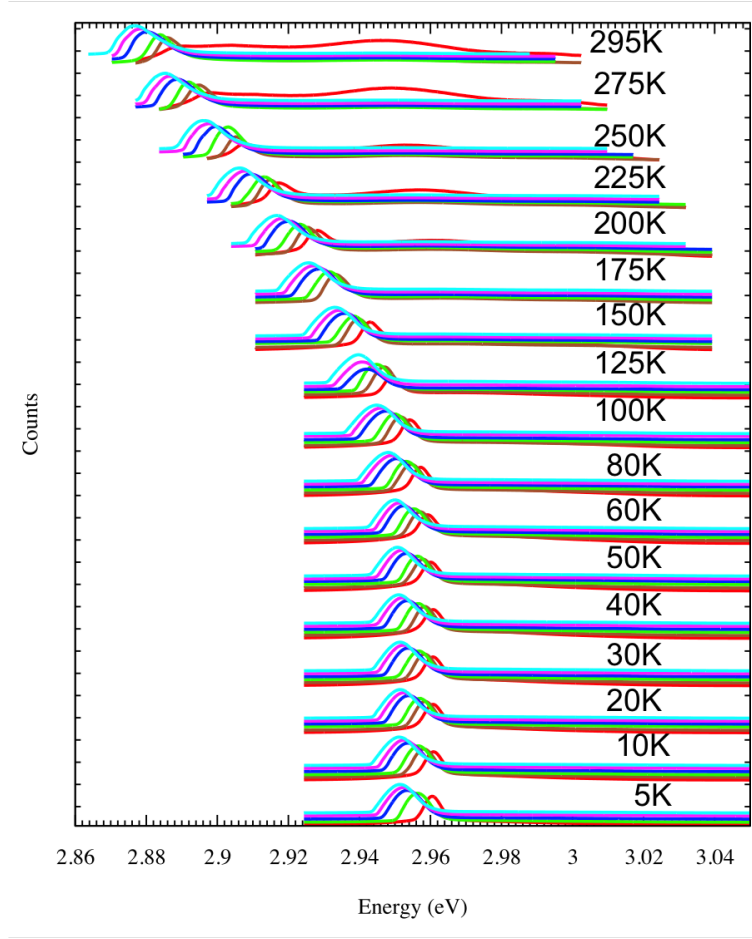


FIGURE 6.15: (a) PL spectra of A1 at 10K for varying excitation power density as 0.6 (red curve), 0.7 (black), 1.0 (green), 2.0 (blue), 3.0 (magenta) and 4.0 (cyan) $mJ.cm^{-2}$ (from bottom to top) at different temperatures (5K to 295K).

$$\Delta E = \left(1 - \frac{1}{(n+1)^2}\right) E_{BE} \quad (6.3)$$

where E_{BE} is the binding energy of the exciton.

As shown in figure 6.15, high excitation band starts to evolve at the laser intensity of $\sim 0.6 mJ.cm^{-2}$ at 5K. If we assign this peak to $P_2(n = 1)$ positioned at $\sim 20 meV$ below the localized exciton energy, would thus give us an exciton binding energy of $\sim 26.6 meV$ (from equation 6.3). This contradicts the activation energy ($\sim 10.3 meV$) calculated from Arrhenius plot, and as well as, the emission peak continued to move towards lower energy (at least by a maximum of 29 meV) with excitation surpassing the expected binding energy. Thus, this cannot be associated with P band.

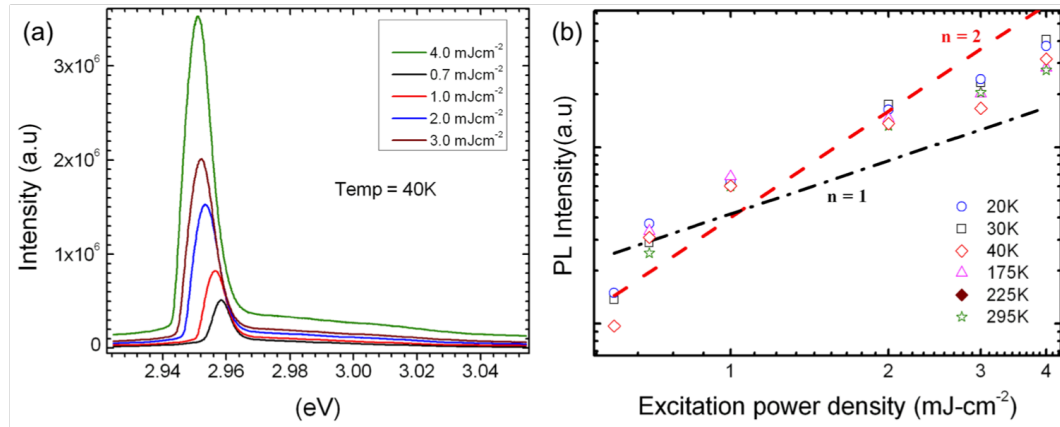


FIGURE 6.16: (a) PL spectra and (b) superlinear growth ($k \approx 1.3$ to 2.0) of PL integrated intensity with for varying input excitation density at 40K.

Further, biexcitons decay cannot either explain our observations, as their characteristic extension of low energy tail of the emission peak wasn't observed in the PL spectra [22]. On the contrary, we consistently observed extension of the tail at the high-energy side of the main emission and its line-width increased with excitation power density (see fig. 6.16a). The most likely mechanism of this high excitation feature is an electron-hole plasma (EHP), where its high-energy side linewidth is related to the plasma temperature. As expected for the EHP recombination, integrated intensity of the luminescence dependence on excitation density shows a superlinear behavior with exponent k between 1.5 and 2 for various temperature (see fig. 6.16b). But at room temperature, k reduces to 1.3. This can be explained by temperature dependent activation of non-radiative processes.

We showed here that at higher excitation densities bulk-like InGaN epilayers exhibit EHP recombination bands causing band gap renormalization contrary to band filling effects which are more frequently observed. After analyzing a set of ten InGaN samples of varying indium content with different structural properties, the differences in photoluminescence behaviour can be related to the structural quality differences of our set of InGaN samples.

Bibliography

- [1] N. Duxbury, U. Bangert, P. Dawson, E. J. Thrush, W. Van der Stricht, K. Jacobs, and I. Moerman. *Appl. Phys. Lett.*, 76:1600, 2000.
- [2] Yong-Tae Moon, Dong-Joon Kim, Jin-Sub Park, Jeong-Tak Oh, Ji-Myon Lee, Young-Woo Ok, H.Kim, and Seong-Ju Park. *Appl. Phys. Lett.*, 79:599, 2001.
- [3] R. Singh, D. Doppalapudi, T. D. Moustakasa, and L. T. Romano. *Appl. Phys. Lett.*, 70:1089, 1997.
- [4] A. Tabata, L. K. Teles, L. M. R. Scolfaro, J. R. Leite, A. Kharchenko, T. Frey, D. J. As, D. Schikora, K. Lischka, J. Furthmuller, and F. Bechstedt. *Appl. Phys. Lett.*, 80:769, 2002.
- [5] S. Srinivasan, L. Geng, R. Liu, F. A. Ponce, Y. Narukawa, and S. Tanaka. *Appl. Phys. Lett.*, 83:5187, 2003.
- [6] R. A. Oliver, M. J. Kappers, C. J. Humphreys, G. Andrew, and D. Briggs, 2004.
- [7] H. Chen, R. M. Feenstra, J. E. Northrup, J. Neugebauer, and D. W. Greve, 2011.
- [8] I. Mahboob, T. D. Veal, L. F. J. Piper, C. F. McConville, H. Lu, W. J. Schaff, J. Furthmuller, and F. Bechstedt, 2004.
- [9] X.A Cao, J.A Teetsov, F Shahedipour-Sandvik, and S.D Arthur, 2004.
- [10] P. G. Eliseev, P. Perlin, J. Lee, and M. Osinski. *Appl. Phys. Lett.*, 71:569, 1997.
- [11] Yong-Hoon Cho, G. H. Gainer, A. J. Fischer, J. J. Song, S. Keller, U. K. Mishra, and S. P. DenBaars. *Appl. Phys. Lett.*, 73:1370, 1998.
- [12] Th. Kehagias, G. P. Dimitrakopoulos, J. Kioseoglou, H. Kirmse, C. Giesen, M. Heuken, A. Georgakilas, W. Neumann, Th. Karakostas, and Ph. Komninou. *Appl. Phys. Lett.*, 95:071905, 2009.
- [13] K. Watanabe, J. R. Yang, S. Y. Huang, K. Inoke, J. T. Hsu, R. C. Tu, T. Yamazaki, N. Nakanishi, and M. Shiojiri. *Appl. Phys. Lett.*, 82:718, 2003.

-
- [14] Z. L. Liu, Z. X. Mei, R. Wang, J. M. Zhao, H. L. Liang, Y. Guo, A. Yu. Kuznetsov, and X. L. Du. *J. Phys. D: Appl. Phys.*, 43:285402, 2010.
- [15] T. A. Wassner, B. Laumer, S. Maier, A. Laufer, B. K. Meyer, M. Stutzmann, and M. Eickhoff. *J. Appl. Phys.*, 105:023505, 2009.
- [16] M. Smith, G. D. Chen, J. Y. Lin, H. X. Jiang, M. Asif Khan, and Q. Chen. *Appl. Phys. Lett.*, 69:2837, 1996.
- [17] C. I. Harris, B. Monemar, H. Amano, and I. Akasaki. *Appl. Phys. Lett.*, 67:840, 1995.
- [18] S. Chichibu, T. Azuhata, T. Sota, and S. Nakamura. *Appl. Phys. Lett.*, 70:2822, 1997.
- [19] R.Liu, J.Mei, S.Srinivasan, H.Omiya, F.A.Ponce, D.Cherns, Y. Narukawa, and T. Mukai. *Jpn. J. Appl. Phys.*, 45 (pt2):L549, 2006.
- [20] W. Zhao, L. Wang, J. Wang, Z. Hao, and Y. Luo. *Journal of Crystal Growth*, 327:202–204, 2011.
- [21] M. Feneberg, R. A. R. Leute, B. Neuschl, K. Thonke, and M. Bickermann. *Phys. Rev. B*, 82:075208, 2010.
- [22] M. Nakayama, T. Hirao, and T. Hasegawa. *J. App. Physics*, 105:123525, 2009.

Chapter 7

Conclusions

We have deeply investigated the electronic properties of various structural defects (threading dislocations, V-defects, nanocracks, misfit dislocations), the current transport mechanism and the origin of the luminescence in GaN, InGaN/GaN and AlInN/(AlN)/GaN.

7.1 GaN

We showed that threading dislocations in MOCVD grown undoped-GaN could be identified with screw- and edge-component by their interaction with the step terraces. Besides threading dislocations, V-shaped defects were also observed, which were related to inversion domains. Surface potential map was mostly dominated by the reduction in potential at the facets $\{1 - 101\}$ of the V-defects, which is due to reduction in barrier height owing to N-termination of this surface and their association to inversion domains. This is speculated based on the existing theoretical prediction of stable surfaces at V-defects. Experimental data from C-AFM and EBIC suggests the same. In C-AFM map, all V-defects facets consistently showed an increment in current in the forward bias, thus, indicating a reduction in barrier height. Their association to inversion domains was evident from EBIC micrographs obtained at different depth. It showed that near the surface, the reduction in barrier height at the V-defect appeared as dark contrast. But in the bulk, V-defects appeared as bright contrast. Bright contrast points out the presence of an in-built electric field in the bulk, which is reasonable at the inversion domains due to the formation of $(0001)/(000\bar{1})$ junction.

From photoluminescence measurements, we identified radiative transitions related to donor bound excitons D_0X , free exciton A and free exciton B. The binding energy of

D_0X was calculated to be around ~ 32.3 meV, which suggests that it is related either to Si_{Ga} or O_N . In case of free excitons A and B, their activation energies were 6 meV and 27.5 meV, respectively. Temperature dependence of PL also shows that transitions related to FX_A evolve into FX_B at around 50 K.

7.2 AlInGaN/(AlN)/GaN

We have shown that with AlN interlayer thickness, surface roughness increases, but dislocation density remained almost unaffected, indicating that no dislocations were generated in the interlayer or the barrier layer. All the dislocations observed on the surface are associated to dislocations present in GaN. Almost all dislocations either open as V-defects or have large diameter core. Unlike GaN, dislocations couldn't be identified as screw- or edge- as the surface morphology showed three-dimensional growth and step terraces were almost absent. Exceptionally, for sample with AlN thickness as 7.5 nm, nanocracks were observed on the surface. Nanocracks were found to originate from the cracking of interlayer AlN, which further propagate with the growth of AlInGaN. Since the gallium was incorporated in AlInGaN unintentionally, actual composition was measured by using XPS and AES and compared with RBS. AES showed reluctance in capturing Auger signal of indium due to its low sensitivity and high noise signal. On the other hand, alloy composition determined from XPS came very close to RBS and around 40% of Ga was unintentionally incorporated in AlInGaN. Interestingly, Hall measurement data showed high mobility and high electron concentration of 2DEG in these heterostructures, indicating AlInGaN as a potential possibility to be used in HEMT structures replacing AlGaIn and AlInN. From local conductivity and nano-scale I-V measurements, we deduced that V-defects and nano-cracks were associated with high conductivity, and were the main cause of Schottky gate leakage observed. By means of AFM phase-contrast imaging, we further showed that these defects were associated with inhomogeneity and were assessed mainly as segregation of metallic atoms such as In or Ga near the V-defects and/or dislocation core, in order to form a current path between the surface and 2DEG region. This was further verified by STS measurements where a reduction in band gap locally and presence of metallic nature near the V-defects were consistently observed. However, no additional states related to dislocation core can be concluded from this data as the dislocation cores in V-defects were situated around 5 to 10 nm below the surface. In contrary to n-GaN, mobility in these 2DEG structures were found not to be limited by the dislocations but by interface/surface roughness scattering. Autocorrelation length calculated from the topography obtained by STM and AFM varied significantly, 2 nm and 120 nm, respectively. The Hall mobility data

for all the samples showed an excellent agreement with the theoretical model of remote roughness scattering by Jena et al. In the calculations, autocorrelation length as 2 nm was used. This indicates that micro scale modulation or grain-size features as observed very often by AFM do not determine the mobility in structures with 2DEG. This also shows the importance of nano scale investigation. Furthermore, nano scale I-V measurements were performed on defect free areas in all the samples, which couldn't be explained by the conventional models on thermionic emission, thermionic field emission and Frenkel-Poole effects. So, we modeled thermionic emission from the 2DEG region considering the lowering of the confinement due to the image charge of the 2DEG. The measured I-V is in agreement with our model. This indicates that when Schottky gate reduces to nanoscale (few 100 nm^2), phenomenon such as image charge plays a very important role in determining the conduction mechanism. The photoluminescence of these heterostructures are dominated by emission from GaN (related to D_0X , FX_A , FX_B and LO-phonons) with a significant reduction in their linewidths. This is due to the presence of high concentration of carriers (2DEG) near the interface. Further, the transitions related to 2DEG region was identified as the recombination between photoexcited electrons in second subband of the triangular well and the holes in the valence band away from the interface where the 2DEG region diminishes significantly.

7.3 InGaN/GaN

From a set of MOCVD grown InGaN samples with varying indium content, we studied electronic properties of threading dislocations and misfit dislocations identified with non-basal slip plane. Though threading dislocations were present in all samples, misfit dislocations were only found in samples with In_i18%. The surface potential map of InGaN with indium up to 17% showed that there was an increment in the surface potential (by 10 to 15 meV) at 62% of the V-defects (i.e. threading dislocations with an edge component), while other (pure screw threading dislocation) showed no variation. The enhanced surface potential was in contrast to the case of GaN, suggesting the V-defects were negatively charged because of their association to acceptor gap states. The local conductivity map in both forward and reverse bias showed quite homogenous current distribution, including at the V-defects, which also conveys that the lowering of barrier height due to indium inclusion at the V-defects is only few meVs. However, as the indium percent was increased (to 19%), the surface potential increment at the V-defects elevated to 50 meV. This is in good agreement with the already know electronic properties of InGaN that with indium content alloy fluctuation (In-accumulation) intensifies and bulk and surface free electron concentration increases.

The local conductivity map in both forward and reverse bias also showed localized high conductivity at V-defects. The variation in the barrier heights at V-defect and defect-free area estimated from current map was between 40 to 60 meV, which is in accordance with the surface potential variation. EBIC micrograph also illustrated that the threading dislocations in also were strong recombination centers.

From the optical characterization on a set of InGaN samples, we observed that photoluminescence is dominated by the presence of localized excitons instead of free or impurity bound excitons causing S-shape temperature dependence of its emission. These localized excitons are due to the presence of local fluctuations in In-N (InN QD) or disordering in InGaN system and occur as band tail states. From the temperature dependence of the PL, local potential fluctuations were underestimated to be around 15 to 20 meV. A strong correlation was also found between the alloy disordering and indium incorporation in InGaN system. This was done by extracting the parameter σ related to Gaussian DOS distribution of band tail states (Eliseev's model), where it monotonically increased with indium percent. Activation energies of the localized excitons were further calculated to lie in the range of 10.6 meV to 40 meV. High activation energies reaching 40 meV were understood in terms of higher disorder and presence of structural defects. Only few of the samples exhibited new-stimulated bands related to many-body effects in the lower energy side of exciton emission on excitation with ArF laser (high density optical pumping). Based on AFM, XRD and SPV results, this behavior was only observed in samples with high structural quality. This stimulated band was identified to electron hole plasma recombination and showed characteristics of superlinear growth of their intensity and band gap renormalization with input excitation power density. While other samples showed a blue-shift with excitation power density that is related to band filling effects and is often seen in literature. Many body effects associated with optical gain. Presence of this effect suggests that we have high quality InGaN layer and this could be highly potential to boost LEDs/LDs performance.

By summarizing all these results, we found that V-defects in ternary and quaternary alloys of nitrides were inherently conductive. However, the significance of their conductivity was found to be strongly dependent on the type of surface termination and presence of, metal (indium) segregation that are completely dependent on the growth conditions. Interestingly, we also observed that threading dislocations in InGaN do not significantly affect the optical properties of InGaN and in theory, high optical gain could be realized as we observed many body effects (related to EHP recombination) for 50 nm thick InGaN samples with indium percent varying from 13% to 19%. This was found to be true as long as there were no additional extended defects such as misfit dislocations.

List of publications

Published

1. A. Minj, D. Cavalcoli, A. Cavallini, Structural and local electrical properties of AlInN/AlN/GaN heterostructures, *Physica B*, 407 (2012) 2838-2840 (2012)
2. S. Pandey, D. Cavalcoli, A. Minj, B. Fraboni, A. Cavallini, D. Skuridina, P. Vogt, M. Kneissl, Mobility-limiting mechanisms in polar semiconductor heterostructures, *Acta Materialia* 60, 3176 (2012)
3. A. Minj, D. Cavalcoli, A. Cavallini, Thermionic emission from the 2DEG assisted by image-charge-induced barrier lowering in AlInN/AlN/GaN heterostructures, *Nanotechnology* 23, 115701 (2012)
4. A. Minj, D. Cavalcoli, S. Pandey, B. Fraboni, A. Cavallini, T. Brazzini, F. Calle, Nanocrack-induced leakage current in AlInN/AlN/GaN, Nanocrack induced, *Scripta Materialia* 66, 327 (2012)
5. S. Pandey, B. Fraboni, D. Cavalcoli, A. Minj, A. Cavallini, Current-Voltage analysis of $Al_{0.86}In_{0.14}N/AlN/GaN$ heterostructures, *phys. stat. solidi (c)* 9, 3-4, 986-88 (2012)
6. A. Minj, D. Cavalcoli, A. Cavallini, Investigation of properties of In-related alloys by AFM, *phys. stat. solidi (c)* 9, 3-4, 982-985 (2012)
7. A. Minj, D. Cavalcoli, A. Cavallini, Defect investigation in $Al_{0.87}In_{0.13}N/AlN/GaN$ heterostructures by scanning force microscopy methods, *J. Phy.: Conference Series* 326 012011 (2011)
8. S. Pandey, D. Cavalcoli, A. Minj, A. Cavallini, Two-dimensional electron gas properties by current-voltage analyses of $Al_{0.86}In_{0.14}N/AlN/GaN$ heterostructures, *App. Phys. Lett.* 99, 012111 (2011)
9. A. Minj, D. Cavalcoli, A. Cavallini, Indium segregation in AlInN/AlN/GaN heterostructures, *App. Phys. Lett.* 97, 132114 (2010)

Under review

1. A. Minj, D. Cavalcoli, A. Cavallini, P. Gamarra, M-A. di Forte Poisson, Strain distribution and defects analyses in III-Nitrides by dynamical AFM analyses, *Nanotechnology* (2013)